
LAB IN TUBE 2019

FINAL REPORT

TEAM ZENITH

Authors:

Brooke Zampell (SV)

Damien Coulon (GM)

Stanislas Furrer (MT)

Pierre Louis Gaudillière (EL)

Mentor:

Dr. Yves Leterrier

8 JUNE 2019



Contents

1	Introduction	6
2	State of the Art	7
2.1	Variable Property Temperature Sensor Technologies	7
2.1.1	Variable Resistance Temperature Sensors	7
2.1.2	Thermocouples	8
2.1.3	Thermoelectronic Sensors	9
2.1.4	Frequency Analog Transducers	9
2.2	Thermal Flow Sensor Technologies	9
2.2.1	Hot Film, Hot Wire	10
2.2.2	Time of Flight	10
2.2.3	Calorimetric	11
2.2.4	Recent Applications of Micro-Thermal Flow Sensors	12
2.3	Material	12
2.3.1	Substrate and Encapsulation	12
2.3.2	Metal	12
2.4	Mechanical Considerations	13
2.5	Extracting Sensor Readings	13
2.6	Selected Technologies and Materials	15
3	Theory of Our Device	16
3.1	Mechanical Calculation and Simulation	16
3.1.1	Constraints Calculations	16
3.1.2	Constraints Simulations	18
3.2	Thermal Calculation and Simulation	20
3.3	Material	21
3.3.1	Substrate	22
3.3.2	Encapsulation	22
3.3.3	Metal	22
3.4	Resistance and Sensitivity Calculations	22
4	Design of Our Device	23
4.1	Constraints	23
4.2	Thermoresistance	24
4.3	Wires	24
4.4	Connection Pads	24
4.5	References	24
4.6	Theoretical Value of the Resistance	25
4.6.1	Spiral Resistance	26
5	Clean Room Process	27
5.1	Lamination	27
5.1.1	Description and Result	27
5.1.2	Learning and Improvements	28
5.2	Exposure	28
5.2.1	Description and Result	28
5.2.2	Learning and Improvements	29
5.3	Development	29
5.3.1	Description and Result	29
5.3.2	Learning and Improvements	30
5.4	Tepla Stripper	30
5.4.1	Description and Result	30
5.4.2	Learning and Improvements	31
5.5	EVA 760	31
5.5.1	Description and Result	31

5.5.2	Learning and Improvements	32
5.6	Lift-Off	33
5.6.1	Description and Result	33
5.6.2	Learning and Improvements	34
5.7	Tape	34
5.7.1	Description and Result	34
5.7.2	Learning and Improvements	35
5.8	Encapsulation	35
5.8.1	Description and Result	35
5.9	Final Result and Discussion	35
6	Sensor to Circuit Connection and Tube Insertion	37
6.1	Connection PCB	37
6.1.1	Design	37
6.2	Wire Bonding	37
6.3	Sensor Insertion	39
7	Conditioning Circuit	41
7.1	Microcontroller and Sensors Specification	41
7.2	Circuit Blocks	41
7.2.1	Signal Generation	41
7.2.2	Amplification	42
7.2.3	Filtering	42
7.2.4	Heat Generation for Calorimetric Principle	43
7.3	PCB Design	44
7.4	Noise Analysis	45
8	Microcontroller and Interface	47
8.1	Data Transmission Method	47
8.1.1	Microcontroller Specifications	47
8.1.2	Comparison to the myDAQ	47
8.1.3	Bluetooth Transmission	48
8.2	LabVIEW Interface	48
8.2.1	Receiving the Data	48
9	Setup and Calibration	49
9.1	Temperature Calibration	49
9.1.1	Platinum Calibration Sensor	49
9.1.2	Noise Elimination	49
9.1.3	Calibration with LabVIEW vs Oscilloscope	50
9.1.4	Calibration During Increasing and Decreasing Temperature	51
9.2	Flow Rate Calibration	51
9.2.1	Closed Loop Flow with Torricelli Principle	51
9.2.2	Flow Calibration Sensor	53
10	Results	55
10.1	Relative Differences of Sensors' Resistances	55
10.2	Evolution of Resistance with Mechanical Constraints	55
10.3	Comparison Between Theoretical and Empirical Results for Flat Sensors' Temperature Calibration	56
10.4	Heater Testing	57
10.5	Temperature Calibration Under Water Flow	59
11	Discussion	61
11.1	Potential Sources of Error	61
11.2	Suggestions for Future Improvements	62
12	Conclusion	63

13 Appendix	67
13.1 Budget and Team Management	67
13.2 Small PCB Layout	68
13.3 LabVIEW Block Diagrams	69
13.4 Testing Setup	70
13.5 Electronic Setup and Oscilloscope Readings	71
13.6 Detailed Formulas For Upstream and Downstream Sensors	73
13.7 Toricelli's Principle	74
13.8 Matlab Code for the Resistance	75
13.9 Acknowledgements	75

Abstract

The goal of this project was to design, manufacture, and characterize a thin film sensor for temperature and flow rate measurements of water in a tube. The project began by conducting a thorough literature review to source inspiration, followed by performing various simulations and calculations on potential designs. Several designs of a calorimetric flow sensor with RTD temperature sensors were then chosen to be manufactured and tested, throughout the process of which the cleanroom steps were optimized to avoid repeats of failures such as excessive lift-off or accidental removal of entire layers. The final product had a polyimide substrate, gold resistances, and a parylene encapsulation, with either spiral-shaped or serpentine resistances. Once these successful sensors were produced, they were connected to an extensive filtering and excitation circuit, which was eventually translated into a battery-powered PCB. Voltage data was transmitted via Bluetooth to a LabVIEW interface where it was processed into temperature and flow readings. Despite the numerous challenges faced in the production of such a device, this short-term development of a product proves that such devices have the potential to revolutionize the biomedical research industry, which has a growing need for small, flexible sensors.

1 Introduction

Temperature and fluid flow sensors are widely used technologies that have many applications in industry and research. These applications serve as motivation for our project, the goal of which is to design, manufacture, and characterize a thin film temperature and flow sensor for water that could one day be translated into use for biomedical sensing.

A variety of implementation methods exist for both temperature and flow rate measurement. Each method works best for certain applications but functions poorly in other situations, hence the wide assortment.

Temperature can be quantified by measuring a material property that varies with temperature; a diverse array of properties can be used. Typical examples of these properties include volume of a liquid such as in thermometers, resistance of a metal such as in thermistors, and amount of emitted thermal radiation such as in pyrometers. Each of these methods requires a different type of interface with the fluid it is measuring (such as pyrometers projecting a laser from a distance) and a different way to read the result (such as reading the mercury level of a thermometer by eye).

Fluid flow measurement methods can be categorized into either macro-scale or micro-scale sensing. Mechanical sensing methods are often employed to measure industrial-sized flow rates; these methods involve restricting the flow in a specific way such as in Venturi tubes or orifice plates, using the flow to rotate turbines, or placing an obstacle in the flow to measure either the resulting vortexes or the forces exerted on fluid [13]. These methods, however, are not suitable for the micro-scale flows found in biomedical applications, due to their moving parts, manufacturing difficulties, and interference with the fluid flow [3].

Another approach to flow sensing, which avoids disturbing the fluid, involves using ultrasonic waves to measure the transfer of energy. While ultrasound finds great application in imaging, it is less useful for flow sensing since any small perturbations from the most ideal of measuring conditions causes large errors in the readings, and emitting and receiving ultrasound in liquids often encounters difficulties [3] [48].

Micromachined thermal flow sensing technologies circumvent all of these challenges, and thus have gained momentum in the biomedical sector. While thermal methods do depend on the physical properties of the fluid and therefore have to be calibrated to the specific application they are used for, they bring a wealth of other advantages to the table. The fabrication of these thermal flow sensors has greatly improved in recent years, due in particular to increasingly efficient miniaturization equipment [1]. These sensors are small and lightweight, consume less power, have high sensitivity, and can be easily integrated with other modules such as wireless telemetry [2]. Such advantages lead to thermal sensors being used for purposes such as measuring cerebrospinal fluid flow in hydrocephalus shunts [4], monitoring blood flow within arteries [5], and ensuring precise dosing of drugs from smart inhalers [6].

This project aims to measure liquid flows on the order of milliliters per minute. At this small scale, thermal sensors are clearly the best design choice for measuring flow. As for temperature sensors, only certain methods work in the context of this project; to ensure compatibility with the flow sensor, the temperature sensor must have direct contact with the fluid and must be able to be interpreted via connection with a read-out circuit, thus narrowing the field of possibilities.

Within a 16 week time period, our team attempted to create a sensor which met the desired specifications of measuring temperature in the range of $35\text{--}45^\circ\text{C} \pm 0.1^\circ\text{C}$ and flow rates in the range of 10-100 ml/min. All iterations and components of the device were made or acquired for a total budget of less than 2000 CHF, demonstrating how relatively economical the development of this device was. Such a feat is significant because this design could be ultimately translated into biomedical research applications, where temperature and flow sensors are gradually becoming more and more in demand. With such cheap, rapid development using standard materials, the project serves as a proof of concept that these types of sensors have the potential to break into the market.

Developing such a sensor did not come without challenges. For instance, the thickness of each layer of the microfabricated device had to be optimized, to ensure the resistance material is protected while not being entirely insulated from the liquid it is trying to detect. The materials of the layers also had to be carefully selected to ensure that they not only fulfilled flexibility and thermal requirements but were also compatible with each other to prevent issues such as delamination. The read-out circuitry had to properly excite the resistances of the sensor without burning them out, and then correctly filter the large amounts of noise. These problems and many more were navigated over the course of the semester.

This report details our project, and proceeds in approximately the order in which the project was tackled. It first begins with an extensive literature review on existing temperature and flow sensor technologies, from which we sourced inspiration for our design. The sections following the state of the art discuss the theoretical design of our sensor including mechanical and thermal considerations, the clean room process flow for manufacturing, and the read-out circuitry for processing and displaying the data. Finally, we discuss the characterization of our device and comment on how well our design worked.

2 State of the Art

Although this project calls for sensors that function under specific conditions and meet certain requirements, leading to the narrowing of the possibilities to thermal-based flow sensors and thermal-compatible temperature sensors, there are still several potential types of measurement systems. With this in mind, the first step is to thoroughly review existing technologies for these sensors.

2.1 Variable Property Temperature Sensor Technologies

Given that the flow sensor will be focused on thermal technologies here, there are several options for a compatible and easily integrable micromachined temperature sensor, all of which have some material property that varies with temperature. The options for these sensors are: resistance temperature detectors (RTDs), thermistors, thermocouples, thermoelectric sensors, and frequency analog sensors.

2.1.1 Variable Resistance Temperature Sensors

RTDs and thermistors both operate on the principle of thermoresistivity, meaning their resistance changes with temperature. These two sensors differ in that RTDs are based on metal while thermistors use the variable resistance of either a polymer or a ceramic.

Thermoresistive sensors use the principle of heat transfer away from a resistive element. When fluid flows over the sensor, convective heat loss occurs, causing a drop in the temperature of the sensor. The change in temperature causes a substantial decrease in resistance, which leads to a change in voltage or current. These are by far the most popular types of micromachined flow sensor due to their easy fabrication, operability, high sensitivity, and good signal-to-noise ratio (SNR) [45][16]. Depending on the materials preferred, the relationship between resistance and temperature can be linear or non-linear. Thermistors, which are based on semi-conductor resistance and thus have a negative temperature coefficient (NTC), are non-linear and have negative variation. Metal thermoresistive resistance temperature detectors (RTD) are linear (Figure 1). The direct, linear relationship between the nominal resistance of an RTD and the temperature is:

$$R(T) = R(T_0)[1 + \alpha(T - T_0)] \quad (1)$$

where $R(T)$ is the resistance of the wire at temperature T , $R(T_0)$ is the nominal resistance, and α is the temperature coefficient of resistance (TCR), a material property [55].

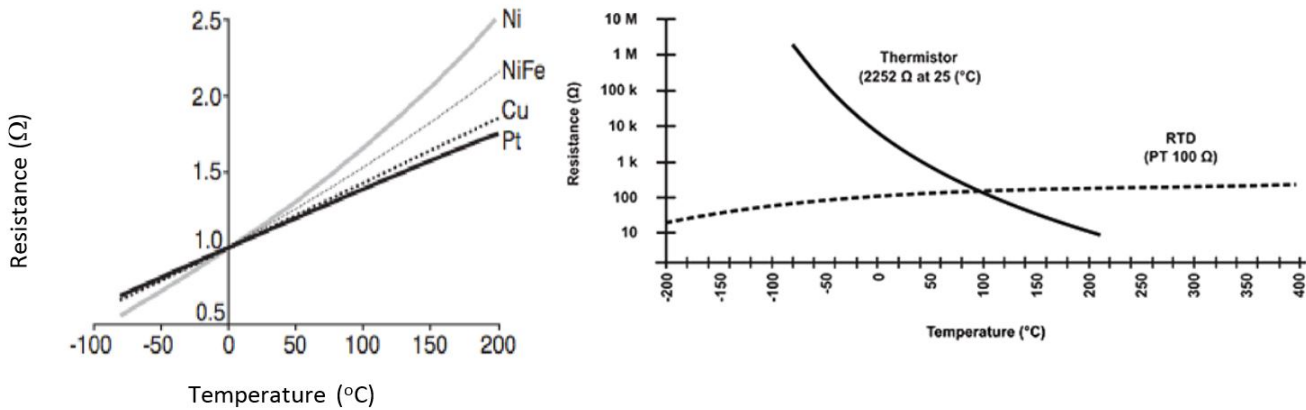


Figure 1: Relationship between resistance and temperature for sensors with variable resistance. **Left:** metal thermistance (RTD) [59]. **Right:** MgO ceramic thermistor (NTC) [55]

The stability of an RTD sensor is characterized by its ability to maintain the same resistance versus temperature relationship for the same conditions over time; any changes in this relationship are referred to as drift. The drift of an RTD sensor is generally a product of the choice of the material. The most common material by far is platinum. Platinum is used for several reasons, including its ability to process at high temperatures, strong stability, good oxidation resistance, high TCR, and simple micromachining processes [45][18][32][33]. For example, a microfluidic

focal delivery device with flow rate monitoring designed by Jonathan et al used platinum for the array of thermal flow sensors, to take advantage of platinum's high corrosion and oxidation resistance [34]. Other materials used to make RTDs include nickel, copper and chromium. Nickel is suitable for good sensitivity and low cost applications at temperatures ranging from -100°C to 200°C[46]. Kaanta et al used Cr/Ni resistors over a suspended silicon nitrite membrane to create an array of flow sensors for micro-gas chromatography systems [35].

2.1.2 Thermocouples

Thermoelectric sensing involves reading the potential drop between two conductors or semiconductors, which are joined at one end (the "hot junction") and left as an open circuit at the other end where the voltage can be read (the "cold junction"). This configuration is called a thermocouple [16] (Figure 2).

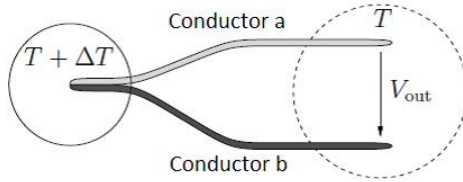


Figure 2: Representation of a thermocouple [16]

Due to the Seebeck effect, a temperature change in the medium will induce a potential in the thermocouples of a thermoelectric sensor [17]:

$$V_{ab} = (\alpha_a - \alpha_b)(T_{hot} - T_{cold}) \quad (2)$$

where α is the Seebeck coefficient of each conductor. Notice that this equation is only dependent on temperature and material properties; the thermocouple is unlike most other temperature measurement systems in that it requires no excitation current to operate. One issue with thermocouples that must be navigated, however, is the small voltage across the open circuit (on the order of microvolts per kelvin), which may make the read-out difficult. It can be increased by connecting several thermocouples in series, an ensemble called a thermopile [1]. The increased number of thermocouples, however, causes an increase in the Johnson noise (random movements of the atoms that are transmitted to conducting electrons) [3]. Increasing the sensitivity requires high thermal isolation between the cold and the hot junctions in order to maximize temperature difference [1]. The accuracy of the thermocouple is limited by the purity of the conductors and the quality of the junction: the two conductors have to be in good physical contact and well isolated. Its physical limit is based on the melting point of the conductors [17].

The voltage at the cold junction is proportional to the temperature difference through the Seebeck coefficient of the two conductors [1]. Table 1 shows the Seebeck coefficients for a variety of materials.

Material	$\alpha[uV/K]$ at 273K	$\alpha[uV/K]$ at 300K
Au	1.79	1.94
Cu	1.7	1.83
Ni	-15	-18
Al	3.5	-1.7
Si		435
P-type	Polysilicon	170
N-type	Polysilicon	-120

Table 1: Seebeck coefficients of common materials at 273 K and at room temperature [16]

Silicon at room temperature has the highest Seebeck coefficient, which makes it a very good candidate for thermocouples. The same applies for its extrinsic form when it is N or P doped. One example use in literature is the thermopiles for the temperature sensor of A. Abarca, made from N-type and P-type polysilicon. Moreover, he utilized P-type polysilicon to design the heaters due to its good linearity to temperature variation and low thermal conductivity [16]. Furthermore, silicon is compatible with integrated circuit technologies as it is the main material utilized to fabricate p-n junctions in transistors or complementary metal-oxide-semiconductors (CMOS).

The Seebeck effect of thermocouples enables high sensitivity, along with an unbiased voltage with no drift nor offset [18]; but the manufacturing of these sensors is complicated since less conventional materials are utilized [1].

2.1.3 Thermoelectronic Sensors

In thermoelectronic sensors, transistors and diodes are used as active sensing elements. It utilizes the I-V relationship of a p-n junction [19]. If the current across the diode is held constant, the diode's voltage changes with temperature. Empirical data reveals that for silicon and germanium at room temperature, $\frac{dV}{dt} = -2.5mV/K$ [1]. The change with increasing temperature is negative because the bandgap energy of silicon decreases with increasing temperature. Thermoelectronic sensors are compatible with CMOS fabrication and thus can be used in integrated circuits for sensing, but also signal processing and amplification without separate packaging [21]. The use of diodes combined with CMOS technology enables the monitoring of proportional to absolute temperature (PTAT) voltages [19]. The different components are a start-up circuit that biases the CMOS so that they supply the required current. Then, a PMOS current mirror imposes the same currents in all the branches, which implies that the voltages at the source of the NMOS should be equal. At this point we can derive the relationship between the resistance and the current and finally express the reference voltage, which turns out to be linearly proportional to the absolute temperature [19] (Figure 3).

$$V = \frac{n k_B \cdot L \cdot \ln(K)}{q} \cdot T \quad (3)$$

The accuracy of this type of circuit is driven by the diode ideality factor and the accuracy of the ratio between the current of the branches. As these parameters are dependent on the process, on-chip dynamic element matching is used [20]. As a result, improving the accuracy in temperature measurement is more power hungry. Sensing temperature via the thermoelectronic principle is promising. The output voltage is scaled to values of interest, on the order of several mV/K. However, it operates on a smaller temperature range than RTDs. It is utilized to sense temperature between -55°C and 150°C [21]. Finally, because of manufacturing tolerance, it will usually not reach the accuracy of an RTD, though it is extremely cost effective for large volume applications [17]. G. Ghoshdury and A. Hassibi designed a silicon on insulator CMOS p-n diode to monitor temperature that has a 3σ inaccuracy of 1.95°C across a 5°C to 100°C temperature range [23].

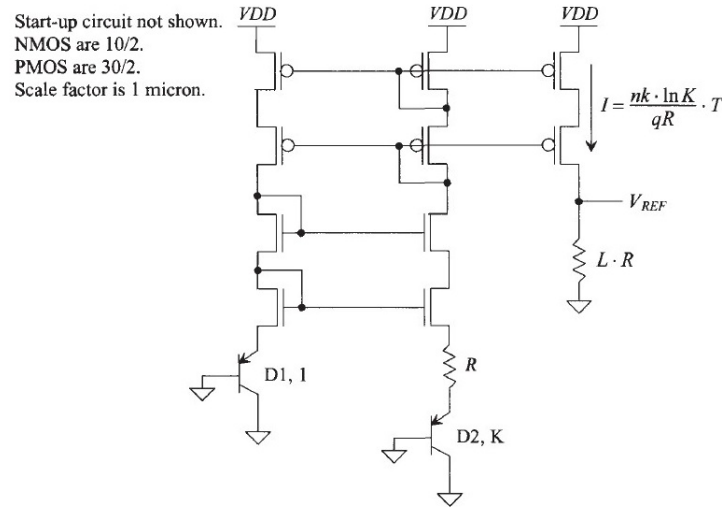


Figure 3: PTAT voltage reference self-biased circuit [19]

2.1.4 Frequency Analog Transducers

Another alternative for measuring the temperature of a fluid is by applying the frequency analog transduction principle. When the temperature of a submerged mechanical element such as a cantilever or diaphragm changes, the stress within the element also changes, thus altering the element's resonant frequency. The change in oscillation can be transduced into a temperature reading [2] [3]. Frequency analog transduction is limited in that it is not very robust to perturbations, and it is more difficult to build and integrate than previously introduced transducers [12].

2.2 Thermal Flow Sensor Technologies

Several of the temperature sensors just mentioned serve as the basis for thermal flow rate sensors. Now that these temperature sensor technologies have been considered, the flow sensor can be examined. Thermal mass flow sensing

methods rely upon the flowing fluid to carry heat away from a central heating element (Figures 4, 5, 6). These methods can be classified into three categories: hot film or hot wire, time of flight, and calorimetric.

2.2.1 Hot Film, Hot Wire

The most basic approach to thermal mass flow sensing involves using one heating element with no other components. The heating element, which is significantly warmer than the fluid that it will sense, can be either a wire or a film. As seen in Figure 4, the governing principle behind this design is that as the fluid flows, it will carry away with it some of the heat from the heating element; this heat loss can be quantified and converted into an output voltage via a Wheatstone bridge [2].

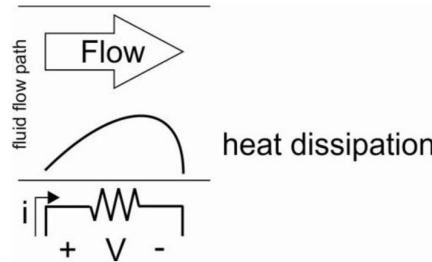


Figure 4: Illustration of thermal hot wire or hot film sensing [2]

There are two modes in which such a sensor can be run, and the choice of mode determines how flow rate is calculated. The first mode involves maintaining the heating element at a constant temperature and measuring the power required to do so. Alternatively, the element can be kept at constant power input, and the flow rate can be calculated by monitoring the change in resistance due to variations in the element's temperature [10]. Although constant temperature mode requires a slightly more complex design due to needing feedback circuitry to maintain the temperature, it is often the preferred mode based on its better frequency response, larger range of measurement, smaller resolution, and higher precision [13] [3]. One application of a constant temperature hot wire sensor can be seen in the work of Melani et al, who designed and fabricated a MEMS sensor to monitor potable water flow [48].

Several characteristics of a hot wire or hot film sensor influence its adeptness at sensing flow. Two of the most important characteristics are the nominal resistance and the TCR; this is because these properties directly affect the sensitivity of the device. For a 4-wire variable resistance sensor (see section 8), the sensitivity is:

$$S_0 = \frac{\Delta V}{\Delta T} = \alpha R_0 I_0 \quad (4)$$

where α is the TCR, R_0 is the nominal resistance, and I_0 is the current through the device. As mentioned in equation 1, the RCR is the factor which directly relates the resistance to the temperature. Based on these relationships, the heating element material should have the highest possible TCR and nominal resistance, while still conforming to other constraints such as mechanical strength and stability, in order to obtain the highest possible sensitivity [3] [2].

Thickness of the encapsulation layer and the ability of the sensor to function underneath this layer is another important point to consider. Most variable resistance materials cannot maintain functionality if exposed directly to the liquid being sensed, and thus a barrier is required. This barrier inhibits transmission of thermal energy between the liquid and the sensor, so the sensor has to be sensitive enough to function regardless.

2.2.2 Time of Flight

In time of flight sensing, a thermal pulse is generated by a hot wire and injected into the fluid. As seen in Figure 5, the downstream thermal sensor detects the heat pulse and the transit time of the thermal pulse will give flow rate information.

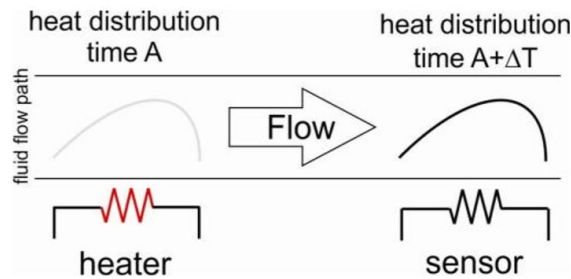


Figure 5: Illustration of thermal time of flight sensing [2]

Ideally, the heater is thermally isolated from the substrate to eliminate interference from thermal conduction effects [2]. The transit time is determined by the thermal conductivity of the fluid, the distance between the heater and the sensor, and the average flow rate [3]. Flow velocity is calculated from the time and the distance between heater and sensor, d_{HS} :

$$v = \frac{d_{HS}}{t} \quad (5)$$

By using multiple thermal sensors instead of one, placed at different distances from the heaters, it is possible to determine not only flow velocities but also fluid properties [7]. However, fluid dependence and nonlinearity are still present for such sensing techniques because of a number of effects related to longitudinal diffusive spreading of the thermal pulse, conduction through boundary layers, and finite detector response time [8][9]. We can, however, cite the work of H Berthet et al. which presents a stochastic time-of-flight measurement operating in a regime in which longitudinal diffusion effects are negligible and with measurements using several sequential detector bridges [11].

2.2.3 Calorimetric

An additional solution to measure temperatures and flow rates with millimetric devices is calorimetric sensing. In this setup (Figure 6) the heater is flanked by two thermal sensors.

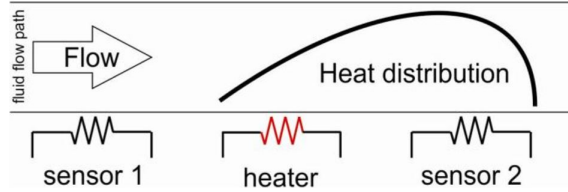


Figure 6: Illustration of thermal calorimetric sensing. [2]

By comparing the two signals from the sensors and knowing the fluid thermal capacity, the fluid velocity can be measured indirectly using the convection principle. After an appropriate calibration of the output signal, the temperature and velocity of the fluid can be calculated [3] [14] [15].

This solution is similar to those explained previously, but it is larger since it requires more elements. The major advantage of this method is that the temperature and flow velocity can both be extracted from the same device, simplifying the overall sensor. The robustness of this method is also good, as explained by M. Elwenspoek in his article [22]. For the heater, a compromise has to be found between mechanical protection and heat transmission to the fluid. The sensors have also to be isolated from the heater to avoid any heat transfer into the substrate and not in the fluid. The thermoresistance must also be designed to be mechanically robust to stretching. A mathematical model corresponding to this solution is visible in article [2]. The measurements will follow this formula:

$$\Delta T = T_h * f(\text{flow, geometry}) \quad (6)$$

with ΔT and T_h measured with the principle of the change of resistance due to temperature, which can be measured relatively to the voltage and current applied to the resistance.

2.2.4 Recent Applications of Micro-Thermal Flow Sensors

We have seen that various approaches exist to measure flow based on temperature. In Table 2 below are listed the methods utilized by some researchers and the range of flow they were able to measure accurately. Certain materials are very common among these sensors. We will see in the next section why these materials are so popular.

Mode	Material	Configuration	Range	References
Th-resistive	Ti/Pt Parylene	Hot-film	0 – 1 $\mu L/min$	Kuo [34]
Th-resistive	W/Ti/Pt Parylene	H-F, Calorim., T-of-F	0 – 400 $\mu L/min$	Meng [37]
Th-resistive	Ti/Au Kapton	Hot-film	0 – 10mL/min	Li [46]
Th-electric	Poly-SI/Ti-W PI	Calorimetric	10 – 100slm	Buchner [18]
Th-electric	Poly-SI/Ti-W	Calorimetric	0 – 2mm/s	Buchner [47]

Table 2: Examples of flow sensor methods and materials.

2.3 Material

With the sensing effects and the transduction principles discussed above, material choice is the next step towards designing a thermal flow sensor. Materials are selected for heating, sensing, and insulating elements.

2.3.1 Substrate and Encapsulation

One of the most important constraints of a flow sensor in biomedical applications is the need for protective biocompatible and impermeable layers. Concerning more specifically the case of a micromachined flow sensor inserted into a tube, the sensor has to be flexible. Potential material choices that meet such requirements for flexibility and biocompatibility include polyimide, parylene, and SU-8. Parylene C is a well-characterized polymer that is used mainly as an encapsulation material, especially for biomedical applications since it is inert, biocompatible, and biostable; it is also an excellent barrier to both liquids and gases [36]. Other properties of interest of parylene C include its flexibility, bendability, conformability, and superior resistance to moisture absorption (0.06 %) [16]. Parylene C could also serve well as a substrate because of its compatibility with a variety of other materials [37][38][39]. Parylene C thin films are produced by chemical vapor deposition (CVD).

Polyimide has many advantageous properties including high Young modulus, good chemical resistance, high hydrolytic stability, adhesive properties, a low dielectric constant, and high thermal stability [40][41]. Polyimide has a much higher tensile modulus (8830 MPa) than Parylene C (20 MPa) and is more robust for sensor development [16]. Besides mechanical and thermal stability, other important factors to consider include manufacturing reproducibility, tolerance to contaminants, and other economical issues [42]. Polyimide thin films are produced by spin coating.

2.3.2 Metal

In order to construct thermoresistive thin film elements, platinum or nickel are most frequently used. Other metals used for micromachined flow sensing are gold, chromium, and copper. Polysilicon has similar properties to metals and can also be used. Table 3 shows electrical, mechanical, and thermal properties of different sensing materials.

Material	Resistivity	TCR, $\alpha(10^{-4}/k)$	Young Modulus E (Gpa)
Aluminum	2.69×10^{-8}	42.0	62
Copper	1.67×10^{-8}	43.0	128
Gold	2.30×10^{-8}	39.0	78
Nickel	6.84×10^{-8}	68.1	207
Platinum	10.6×10^{-8}	39.2	107
Polysilicon	$4 \times 10^{-6} - 1 \times 10^{-1}$	250–10	172

Table 3: Relevant electrical and thermal properties of thermal flow sensor materials [2][49]

The most commonly used material for thermal flow sensors is platinum. While it does not possess the highest TCR among all potential materials, its biocompatibility has made it a popular choice for biomedical flow sensing applications. Platinum is corrosion resistant, compatible with standard micromachining techniques, and used in many implantable devices [12][37][43]. Due to platinum's poor adherence to parylene and polyimide, it is commonly used in combination with titanium [34]. Generally 10 microns of Ti is sufficient [16]. Platinum and titanium both are deposited by an E-beam evaporation process. Nickel, the TCR of which is twice as high as platinum, is a much cheaper alternative to platinum. The tradeoff is that the stable operation temperature of nickel films is much lower than platinum. Similarly to platinum, nickel requires an adhesion layer of Ti, and is deposited by E-beam evaporation process. Doped polysilicon is another popular material for heating elements. The electrical and thermal properties of polysilicon are dopant dependent. The thermal and electrical properties of polysilicon can be tuned by manipulating a combination of grain size distribution, dopant concentration, and doping type [44] [45]. Polysilicon has a high Seebeck coefficient and is thus a good material for thermocouples [16]. One example in literature is the thermopiles of Buchner et al, made of in situ p-doped polysilicon and tungsten/titanium (WTi). This combination of materials creates a high Seebeck coefficient [18].

2.4 Mechanical Considerations

Biomedical applications of these temperature and flow sensors typically call for the device to be flexible, for such purposes as insertion into a catheter or other tube. The various materials also need to be tolerant of a range of temperatures they are subjected to during microfabrication. Bending and thermal stresses therefore need to be calculated and accounted for in the design.

Bending stresses are induced when a material is flexed, causing compressive or tensile stress. This can occur both when the finished device is curled into a bent shape as well as during the manufacturing of the device when it is handled and manipulated [57]. Such stresses, especially when combined with a less-than-perfect adhesion between layers, can lead to delamination, meaning a separation of the device's layers. Bending stress is typically quantified in terms of strain:

$$\epsilon = \pm \frac{x}{R_0} \quad (7)$$

where x is the distance between the neutral plane and the location where the strain is calculated, and R_0 is the bending radius.

Thermal stresses are a serious consideration during manufacturing of the device. When the device has to be exposed to a higher temperature for deposition of certain materials, the layers will expand at different rates due to their mismatched thermal expansion coefficients, leading to residual stresses within the materials [57]. This stress can be quantified as:

$$\sigma_1(T) = \frac{(\alpha_2 - \alpha_1)\Delta TE_1}{1 - \nu_1} \quad (8)$$

where α is the thermal expansion coefficient of each of the two materials, E is the Young's modulus, and ν is Poisson's ratio [56]. If the layers are greatly mismatched in their material properties, then the device can even experience thermal stress just during normal use, if it is exposed to a range of temperatures.

To reduce both of these sources of stress as much as possible, the two most important design considerations are the thickness of each layer and the types of materials. Thicknesses and material properties can be used to calculate the location of the neutral plane and stresses in the device upon bending as well as what range of temperatures the most sensitive part of the device will be exposed to. Most importantly, the most fragile part of the device must be placed as close to the neutral plane as possible.

2.5 Extracting Sensor Readings

After having considered both the temperature and flow sensor technologies, the best type of temperature sensor in terms of integration with a thermal flow sensor is an RTD, which is easy to fabricate, highly sensitive, and made from commonly accessible materials (see section 2.1.1). Extracting information from RTDs boils down to measuring their voltage.

To monitor the voltage at the terminals of the thin film RTDs, we need to inject an excitation current. A simple set-up would be to use a voltage divider, by putting a voltage source and an excitatory resistor in series with the RTD. As the voltage drop across the RTD is proportional to its resistance, when the resistance changes due to a change in temperature, the voltage drop will also change. However, although this configuration is less expensive,

the resistance of the lead wires can add a significant error to the temperature measurement, since they are used to both supply the excitation current and take the measurement [24][27]. Moreover, these resistances may also change with temperature. A common technique to address this issue is to separate the current wires and the measuring connection wires in a 4-wire bridge [26]. Since the voltmeter has a very high input impedance compared to that of the lead wires, the excitation current will not flow into the measuring connection wires and there will be no voltage drop across these wires. Therefore, the voltmeter will only measure the voltage drop at the RTD (Figure 7). Chunyan Li et al have utilized this configuration to measure brain temperature and blood flow and have achieved an accuracy of 0.1°C and a resolution of 0.013°C , which fulfills the requirements of the project [29].

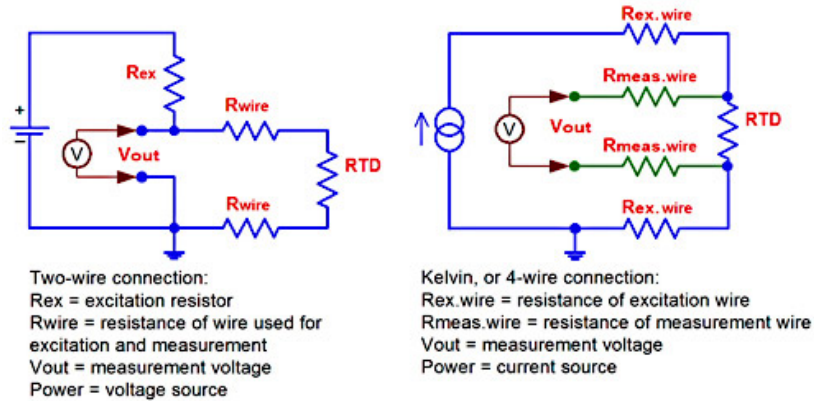


Figure 7: RTD measurements [24]. **Left:** 2-wire bridge. **Right:** 4-wire bridge.

Another alternative to avoid the drop of measurement accuracy due to the lead wires is a four resistor Wheatstone bridge. The excitation current is provided to the bridge by an external voltage source through two lead wires. Ideally, only the RTD changes with temperature whereas the other three resistors have very close to zero temperature coefficient or are well isolated. The output voltage of the bridge will only depend on the resistance imbalance between the two branches. To isolate the three other resistances of the bridge from the RTD, we can separate the RTD from the bridge by a pair of extension wires. These extension wires repeat the same problem stated above. Hence, we can minimize it using the 3-wire bridge configuration, and the effect of the resistance of the lead wires cancels out since they are located in two different branches of the Wheatstone bridge [25] (Figure 8).

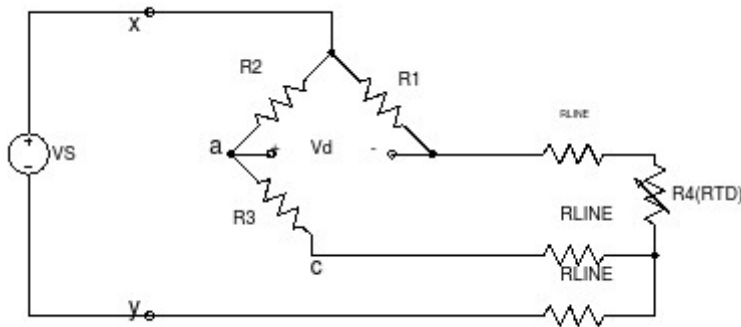


Figure 8: Wheatstone bridge with 3-wire bridge lead wire compensation [50].

When comparing these two configurations, we see that in the case of the 4-wire bridge, the measured output voltage is directly proportional to a change in the RTD resistance, and that it is insensitive to the length of the lead wires utilized for sensing. Moreover we get rid of the three resistances utilized in the Wheatstone bridge and we have instead only one reference resistance. One disadvantage of the 4-wire bridge is that it utilizes one more extension wire than the Wheatstone bridge. Finally, there is a trade-off between the resolution and the response time [24]. Decreasing the RTD resistance will produce a faster response time, but will then require a greater current supply to maintain the resolution; this higher current can lead to self-heating of the resistor, which causes a bias

on the temperature measurement [17]. The temperature error can then be calculated from the self-heating factor of the sensor.

2.6 Selected Technologies and Materials

To summarize our findings from the literature review, RTDs seem to be the technology of choice for temperature sensing due to their high accuracy, easy fabrication and operation, high sensitivity, and good signal-to-noise ratio. Thermistors are similar to RTDs but are susceptible to drift over time and have a lower resistivity. Thermocouples, although highly sensitive and having no need for an excitation current, have limited accuracy and issues with excessive noise. Thermoelectric sensors are cheap to manufacture and can be scaled to a specific voltage range of interest, but require more power and are less accurate than RTDs. Among the flow sensing methods, given the goal of our project to have both a temperature sensor and a flow sensor, the calorimetric principle is the best due to its robust measurements and automatic incorporation of a temperature sensor. Thus, based on this state of the art review, we chose to design a microthermal sensor that uses the calorimetric principle with RTD temperature sensors. The device runs in constant temperature mode and utilizes the principle of thermoresistance for transduction. The constant temperature mode allows for a large range of measurement, small resolution, and high precision (see section 2.2.1). To read the voltage at the flow sensor terminal, we chose a 4-wire configuration, which enables greater measurement accuracy (see section 2.5).

Materials, layer thicknesses, and the process flow design were optimized over three iterations. A polyimide substrate was selected since it fulfills our device's criteria of flexibility and hermetic barrier formation; the thickness of this layer was varied to find the specific optimum for our device. Finite element analysis was used to optimize a mask pattern for the resistances, which included finding the best distance between the heater and temperature sensors to ensure they were isolated from each other while still keeping the device as small as possible (see section 2.2.3). A platinum/titanium mixture was initially selected as the preferred material due to platinum's excellent mechanical and electrical properties (see section 2.3.2); due to encountering problems with the platinum that will be explained later, the final devices had gold/titanium resistances. In both cases, the titanium acts as an adhesive to more effectively bond the metal to the substrate. The metal layer was then encapsulated with a thin layer of parylene (5 microns). This thickness was a compromise between protection from the liquid and heat transmission to the liquid. The preprocessing of the signals from the finished device is performed through a PCB containing several filters. The PCB is connected to a microcontroller with a Bluetooth module, allowing the transmission of the information to a computer interface. Finally, the data is processed and displayed on a computer.

3 Theory of Our Device

3.1 Mechanical Calculation and Simulation

To have a robust sensor, two of the most important factors to consider are layout and dimensions. Since the sensor will be manipulated and inserted in a tube, the mechanical constraints have to be calculated to anticipate and prevent any failure, which can delay the entire project due to the time needed for an iteration, particularly in the clean-room process (see section 5). As mentioned in section 2.3.2, these devices require multiple layers made of different materials, each of which serves a different purpose (e.g. the metal is the actual sensing element while the encapsulation layer protects the metal from the fluid). Mechanical constraints are therefore derived from the thickness and material properties of each layer.

3.1.1 Constraints Calculations

The substrate layer, made of polyimide, was a straightforward decision in that we chose a thickness of $25 \mu\text{m}$, the thinnest available polyimide at CMi. This thickness was motivated by our desire for a flexible device, as well as by the fact that thinner devices have lower strain in flexion.

The encapsulation layer, which protects the metal resistances of the device from the fluid they are sensing, had a wider variety of potential thicknesses available. When selecting the thickness of the encapsulation layer, both thermal and mechanical considerations must be taken into account.

On the thermal side, having the thinnest encapsulation layer possible is ideal. This leads to a maximum amount of heat being transferred to the resistance layer, producing a sensitive device. The mechanical considerations, on the other hand, give motivation for having the thickest encapsulation layer possible. Having a thick encapsulation layer moves the neutral plane closer to the metal layer, providing it protection from mechanical stresses. The metal layer performs the electricity conduction, making it not only the most brittle part of the device but also the most important.

To compromise between these ruling principles while still keeping our metal safe, we looked at how thin we could make the parylene while not exceeding the elastic limit of the gold layer. The gold layer undergoes compression stress. From literature, a compression of less than 1% will induce a stress of around 200MPa for a thin layer (100nm) [54]. From calculations detailed later, we can observe in Figure 9 that a thickness of $4 \mu\text{m}$ matches the maximal strain that the gold layer can withstand in compression. Ultimately, however, we chose a $5 \mu\text{m}$ parylene layer, to provide a security margin as well as to facilitate cleanroom deposition. This is a reasonable choice since this thickness is in a low slope area for the heat flux, so the thermal needs are still relatively satisfied but we avoid the risk of mechanical failure of our device. Thus, the chosen parylene thickness produces a flexible device with protection for the metal while not drastically decreasing the sensor performance by isolating the metal layer from the liquid.

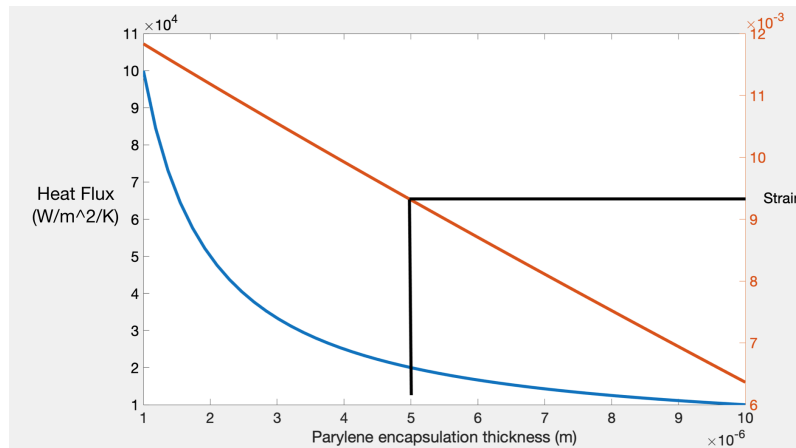


Figure 9: Parylene thickness influence on strain and heat flux

The heat flux in Figure 9 has been estimated with a heat conductivity of the parylene of $0.1 \text{ W}/(\text{m}^*\text{K})$.

The following calculations are demonstrating that the $5 \mu\text{m}$ parylene layer is sufficient to have less than 1% strain in compression for our metal layer.

Here are the characteristics of our chosen layers (Young's modulus and thickness):

- Polyimide :

$$L_1 = 25 \mu m$$

$$E_1 = 2 GPa$$

- Parylene :

$$L_2 = 5 \mu m$$

$$E_2 = 2.7 GPa$$

From those data, we are able to calculate the position of the neutral plane, which is important to be able to evaluate constraints applied to our device (Figure 10). In our calculations for the neutral plane, we will neglect the layer of metal (platinum or gold) due to its negligible thickness and area proportion (less than 2%).

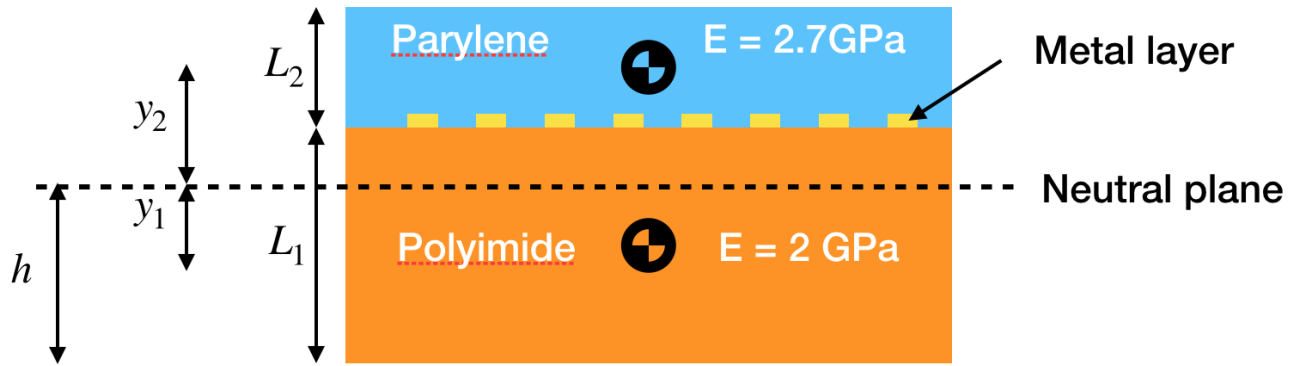


Figure 10: Neutral plane schematic

The neutral plane can then be calculated, with h being the position of the neutral plane in meters:

$$E_1 * y_1 * L_1 + E_2 * y_2 * L_2 = 0 \quad (9)$$

$$\Rightarrow E_1 * \left(\frac{L_1}{2} - h\right) * L_1 + E_2 * \left(L_1 + \frac{L_2}{2} - h\right) * L_2 = 0 \quad (10)$$

$$\Rightarrow h = \frac{2 * 10^9 * 12.5 * 10^{-6} * 25 * 10^{-6} + 2.7 * 10^9 * 25 * 10^{-6} * 2.5 * 10^{-6} * 5 * 10^{-6} + 2.7 * 10^9 * 25 * 10^{-6} * 5 * 10^{-6}}{2 * 10^9 * 15 * 10^{-6} + 2.7 * 10^9 * 5 * 10^{-6}} \quad (11)$$

$$\Rightarrow h = 15.7 * 10^{-6} m \quad (12)$$

Consequently, the distance between the metal layer and the neutral axis is :

$$x = L_1 - h = 25 - 15.7 = 9.3 \mu m \quad (13)$$

Next, we were able to estimate the stress applied on the device while rolled into the tube. As seen in equation 7 (recalled here for convenience), the equation for a bent structure (high deformations), with x being the distance between neutral plane and location where we are calculating the strain, is:

$$\epsilon = \pm \frac{x}{R_0}$$

From the calculation of our device's neutral plane, assuming a tube with the target diameter of 2mm (with a negative sign due to the device being rolled in such a way that induces compression):

$$\epsilon = -\frac{9.3 * 10^{-6}}{1 * 10^{-3}} = -9.3 * 10^{-3} \quad (14)$$

We consequently have under 1% deformation in compression for our metal layer, which is the maximum value we are targeting.

Unlike this unavoidable strain, fatigue will not occur. In fact, once inserted, the stress will remain constant. For larger diameters, stress will be smaller due to the smaller curvature radius of our device.

3.1.2 Constraints Simulations

In addition to the stresses that our device has to withstand while rolled in the tube (see section 3.1.1), we estimated that an additional and probably higher constraint would come from the manipulations and deformations undergone during fabrication, integration in the system, and insertion in the tube. But obviously, the problem of that type of stresses is their random aspect, which depends on too many parameters to be predicted. However, since many designs are available or can be invented, we decided to compare different options. These simulations were performed on devices in tension, since this type of strain is more probable during manipulation and more damaging to our device. We used a finite element analysis to compare different designs, with the same stretching force applied on each simulated device. The finite element analysis tool used was Autocad Inventor. To be able to compare the devices on the same basis, the length, thickness, and width of the wire were the constant parameters, since they are the critical dimensions for the device sensitivity. Additionally, the stress applied was the same for all devices, but is chosen arbitrarily, due to the random aspect of those stresses. The analysis is consequently used to compare the devices on the same basis, even if this stress will potentially not occur in the reality of the sensor.

We compared the four most common designs from literature. These included a classical serpentine resistance (Figure 11a), a classical serpentine but with rounded corners (Figure 11b), a Hilbert curve that is a type of fractal curve (Figure 11c), and a double spiral resistance (Figure 11d) that we considered because of its symmetry and elimination of constrain concentration zone.

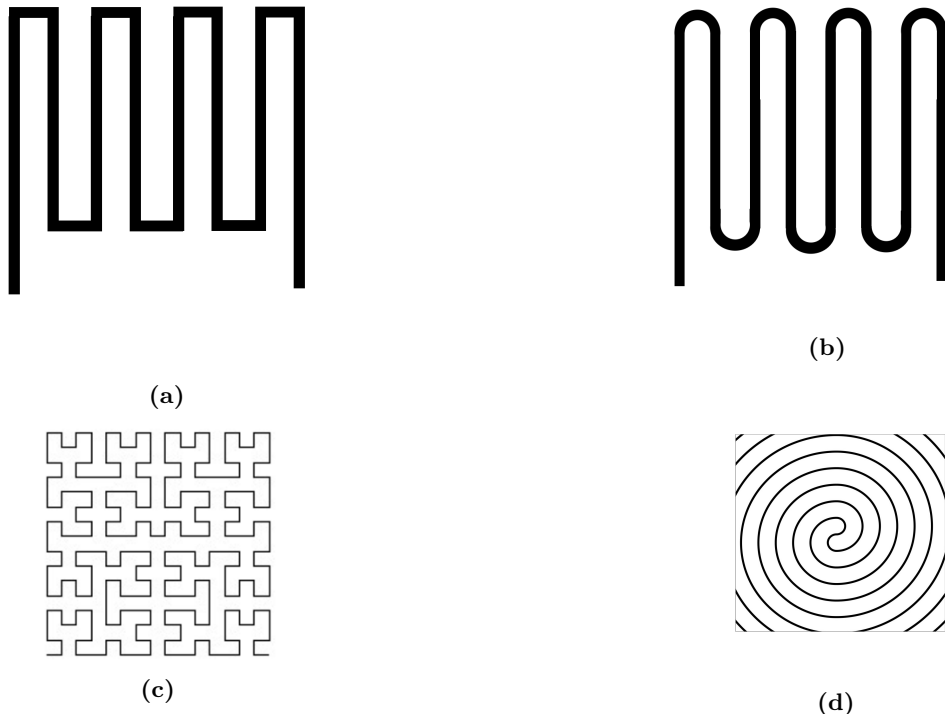


Figure 11: Different sensors design (a) Square serpentine (b) Rounded serpentine (c)Hilbert curve (d) Double spirale

From those designs, we do a comparison with a finite element analysis software. To have meaningful results, we accounted for the length (14.4mm), thickness (100nm), width ($25\mu\text{m}$), covered area, force applied (0.05N), and material (platinum). We apply a lateral stress to the plate on which the resistance is fixed. We then vary the direction of the applied force because of the non symmetry of the devices, with the exception of the double spiral one.

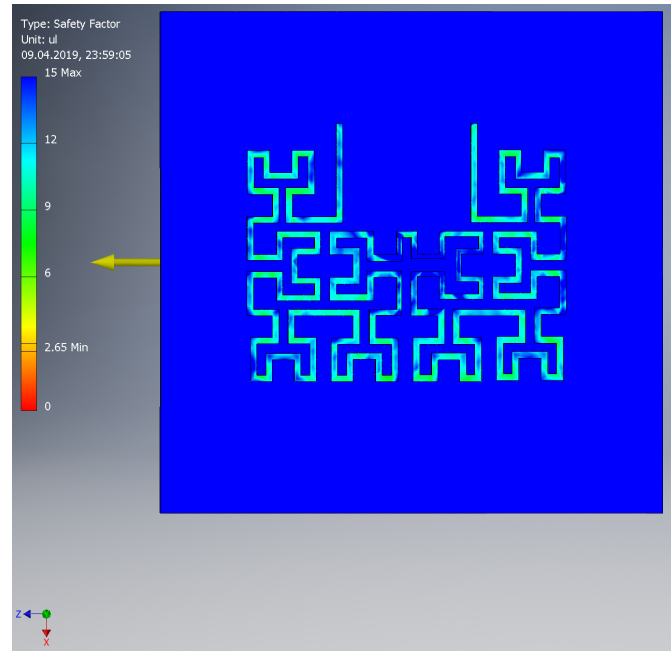
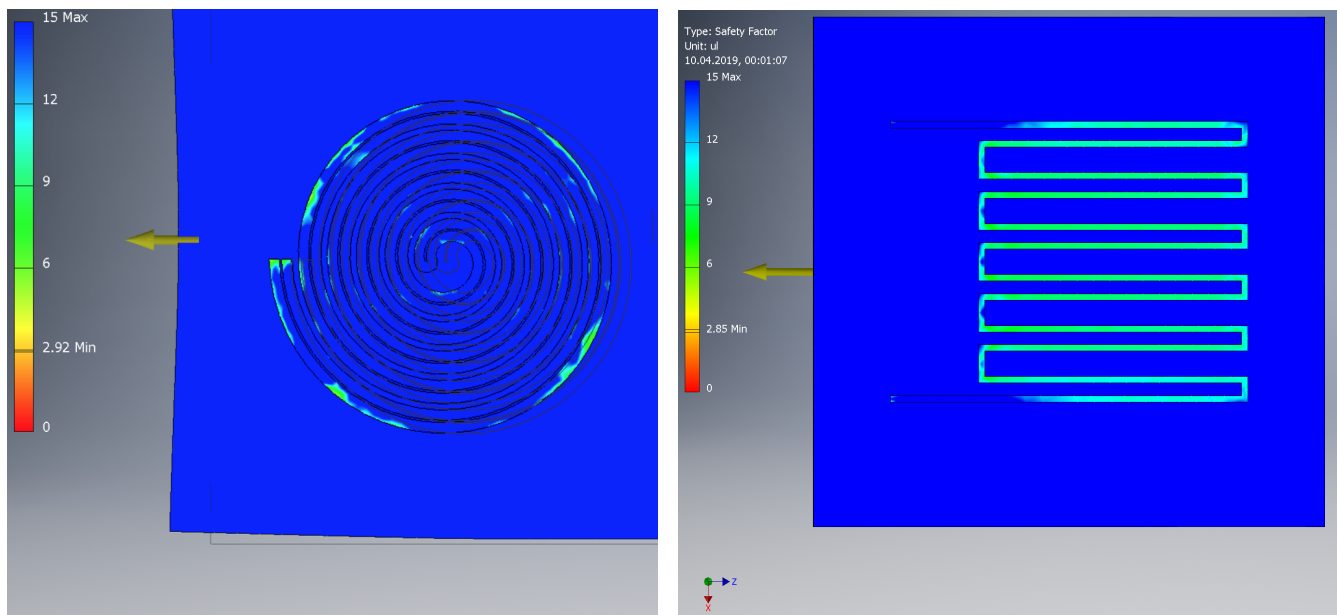


Figure 12: Hilbert design FEA



(a) Classic serpentine design FEA

(b) Spiral design FEA

Figure 13: Serpentine and Spiral FEA results

In Figures 12 and 13, we can see what the FEA interface looks like, with the results for stretching of a "Hilbert curve" design in direction z.

In Table 4, we show the results of the analysis. In the first column there are the different types of design, in the

second one the load direction, and in the third column the minimum security factor, which is defined as:

$$\text{Min Safety Factor} = \frac{\text{Yield Stress}}{\text{Max Working Stress}} \quad (15)$$

Type	Load Type	Min security factor	Max working stress (MPa)
Spiral	Tension	2.9	37.2
Classic	Tension x	2.24	48.2
Classic	Tension z	2.85	37.9
Hilbert	Tension x	1.68	64.3
Hilbert	Tension z	2.65	40.8
Rounded	Tension x	2.36	45.8
Rounded	Tension z	2.31	46.8

Table 4: FEA results

From Table 4, it turns out that the spiral option has the best mechanical properties among the different options, because of its higher security factor compared to the other designs for the same stress. This can be explained by the elimination of all constraint concentration zone, which permits the distribution of stress over the device, reducing the maximum stress.

3.2 Thermal Calculation and Simulation

To determine the distance needed between the heater and the sensors, it is difficult to perform an analytical method, due to the complexity of a model which has to account for both heat transfer through different layers as well as conduction. From literature [7][8][11], we observed that a distance of $100\mu\text{m}$ would be a good solution in our case. To confirm this choice, we first looked at simulation results from articles (Figure 14). Then we did our own, to confirm the found results in our specific case.

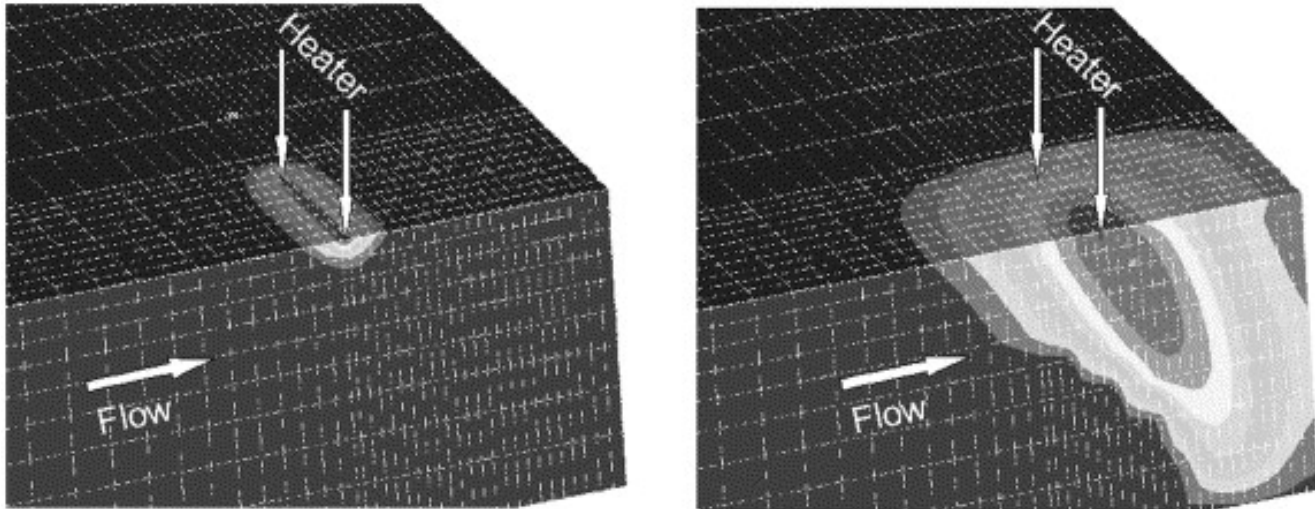


Figure 14: Heat transfer simulation from literature [8]

The model is 2D, due to the problem being axisymmetric. The sensor has been modeled by a rectangle, with its major part inside the tube, and a small part outside, for visualization and simplicity of programming. The tube has been modeled by a rectangle, filled with a liquid that has the density, conductivity, and heat capacity properties of water. The initial condition is 20°C everywhere in the model, as seen in Figure 15.

In Figure 16, we can see that after 4s, which is the heating time, we have a temperature elevation of 0.5°C at $100\mu\text{m}$, which will be easily detected by our sensor. That seems to confirm our choice, even if the simulation is not precise enough to completely base our design upon.

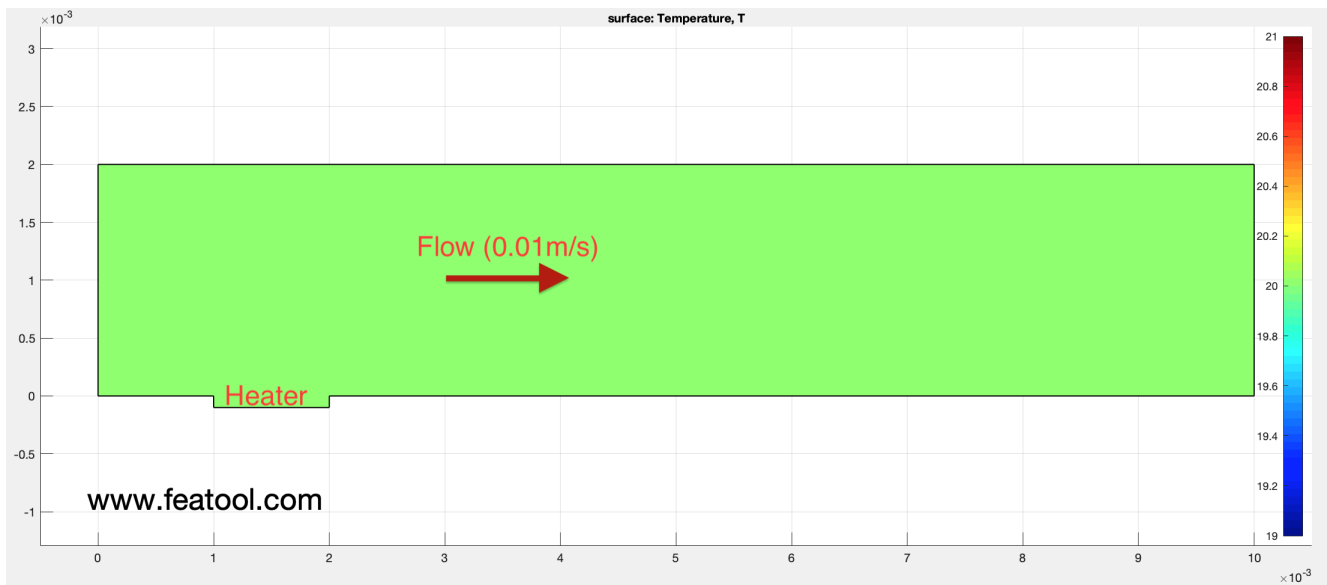


Figure 15: Heat transfer simulation, initial condition. The color bar on the right represents temperature in °C. Units of the x and y axes are mm.

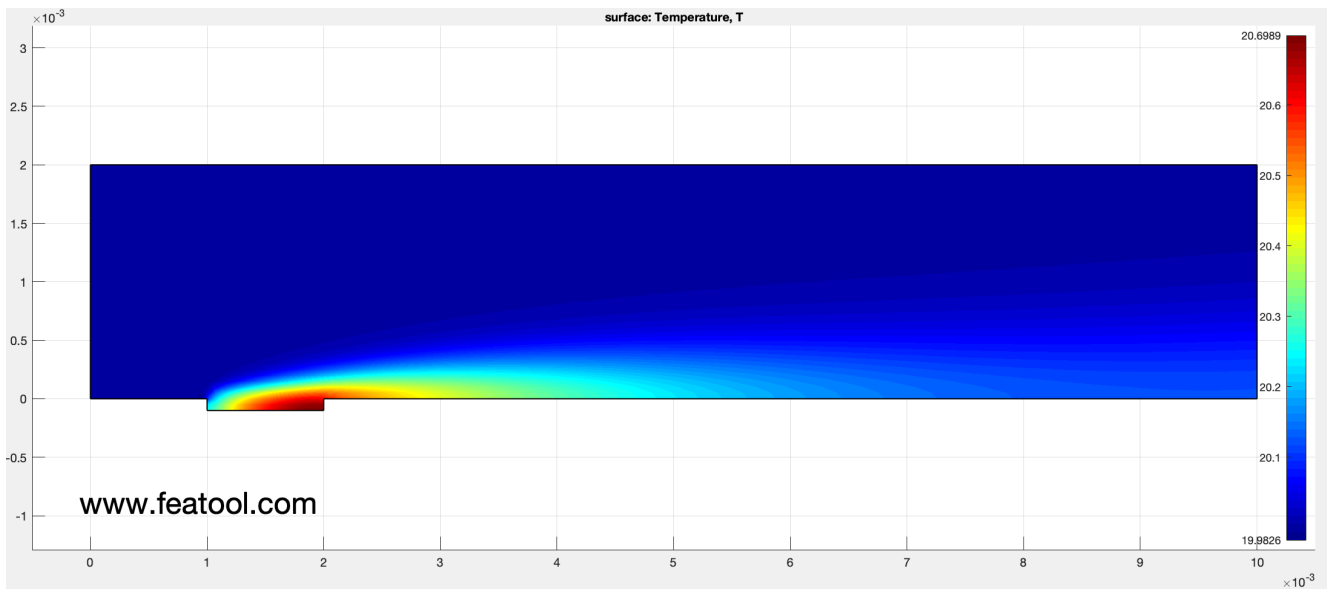


Figure 16: Heat transfer simulation, after 4s. The color bar on the right represents temperature in °C. Units of the x and y axes are mm.

Finally, we chose this $100 \mu\text{m}$ distances between heater and sensor. From literature, it seems to be the optimal distance, because we need to be close enough to the heater to have convection in flow in a short distance for precision, but if the sensor is to close to the heater, conduction problems through the sensor are appearing, decreasing the performance of the sensor. This comes from many articles, in particular articles [7][8][11]. Due to the time and abilities necessary to establish a robust and complete model, we only computed simple heat transfer simulation in a fluid, leading to some elements of confirmation for our choice.

3.3 Material

The realization of our project necessitated 3 generations of sensors. The different iterations enabled the evolution and optimization of the manufacturing processes as well as the choice of materials. Our strategy was to obtain as many operational devices as possible with the highest possible quality (i.e. a small difference between the three

resistances of a device). Our three generations share the same thickness and choice of materials for their substrates and encapsulations. Only the choice of the metal film has evolved between the different iterations. This section aims to review the evolution of the choice of materials during our project.

3.3.1 Substrate

As mentioned in section 2.3.1, only three substrates (polyimide, SU8, and parylene) satisfy our specifications. Due to limitations in the materials available to us as well as the fact that we were not able to use spincoating, however, our only choice was polyimide. EPFL's Center of MicroNanoTechnology (CMi) trained us to laminate 25, 40, or 50 micron thick layers of polyimide substrate film. Initially, we had also contacted the company COMELEC through Mr. Florian Bourgeois to request a spincoated parylene substrate from them; this would have resulted in having a thinner substrate as well as better adhesion between the substrate and the hermetic parylene seal, which we would have liked to compare to the polyimide substrate devices. Unfortunately, this pursuit had to be abandoned due to a lack of time. Since our goal was to minimize the overall thickness of our device, we chose to opt for the thinnest film available: 25 microns of polyimide.

3.3.2 Encapsulation

The EPFL's CMi allows us to choose the parylene encapsulation thickness. Since we desired a thickness that compromised between mechanical protection during bending and heat transmission from the liquid, we chose a thickness of 5 microns, which matched our literature review findings.

3.3.3 Metal

The sensitivity of our product depends on the nominal resistance as well as the alpha coefficient (see equation 1). Over our various iterations, we chose to test a mixture of Au/Ti as well as a mixture of Pt/Ti. Our first generation was in gold (100 [nm])/titanium (10 [nm]). In terms of optimizing the sensitivity of our devices, the platinum/titanium mixture seemed to be the ideal candidate, but it was not available at the time of the first iteration. The gold's poor adhesion to the substrate as well as the fact that its properties are not as well suited to this purpose compared to platinum led us to use platinum/titanium in our second iteration. Problems with cracks in the platinum (as discussed in section 5.5), however, led us to use gold once again in our final iteration, with an additional step to improve its adhesion to the substrate (see section 5.4).

3.4 Resistance and Sensitivity Calculations

As a reminder, the sensitivity of a sensor resistor connected in 4 wire is given by the formula:

$$S_0 = \frac{\Delta V}{\Delta T} = \alpha R_0 I_0$$

The sensitivity increases with the nominal resistance as well as the alpha coefficient. In section 2.3.2, we discussed the different materials to optimize sensitization, namely platinum, gold, and nickel. The geometrical characteristics of the resistor have been adapted to give it high resistance at room temperature and to minimize heating energy consumption by minimizing the surface area of the sensors. To do this, the surface of the resistors is a compromise in order to have a high resistance and to minimize the consumption of energy. In our case this means minimizing the distance between each coil loop or double spiral turns and maximizing the number of loop or spiral turns in a sufficiently small area (see Figures 18a, 18b and 18c).

4 Design of Our Device

From the state of the art section (2) and the theory section (3), we have a more precise idea of what our sensor has to look like to perform as robustly as possible. But drawings have to be made to order the mask for the clean room, with all detailed elements respecting the constraints: thermo-resistance itself, wires, connection pads, and references.

Once the drawings were made, we transmitted them to CMi so that the chromium mask could be produced (Figure 19), with some format compatibility challenges.

The final result can be seen on Figure 17.

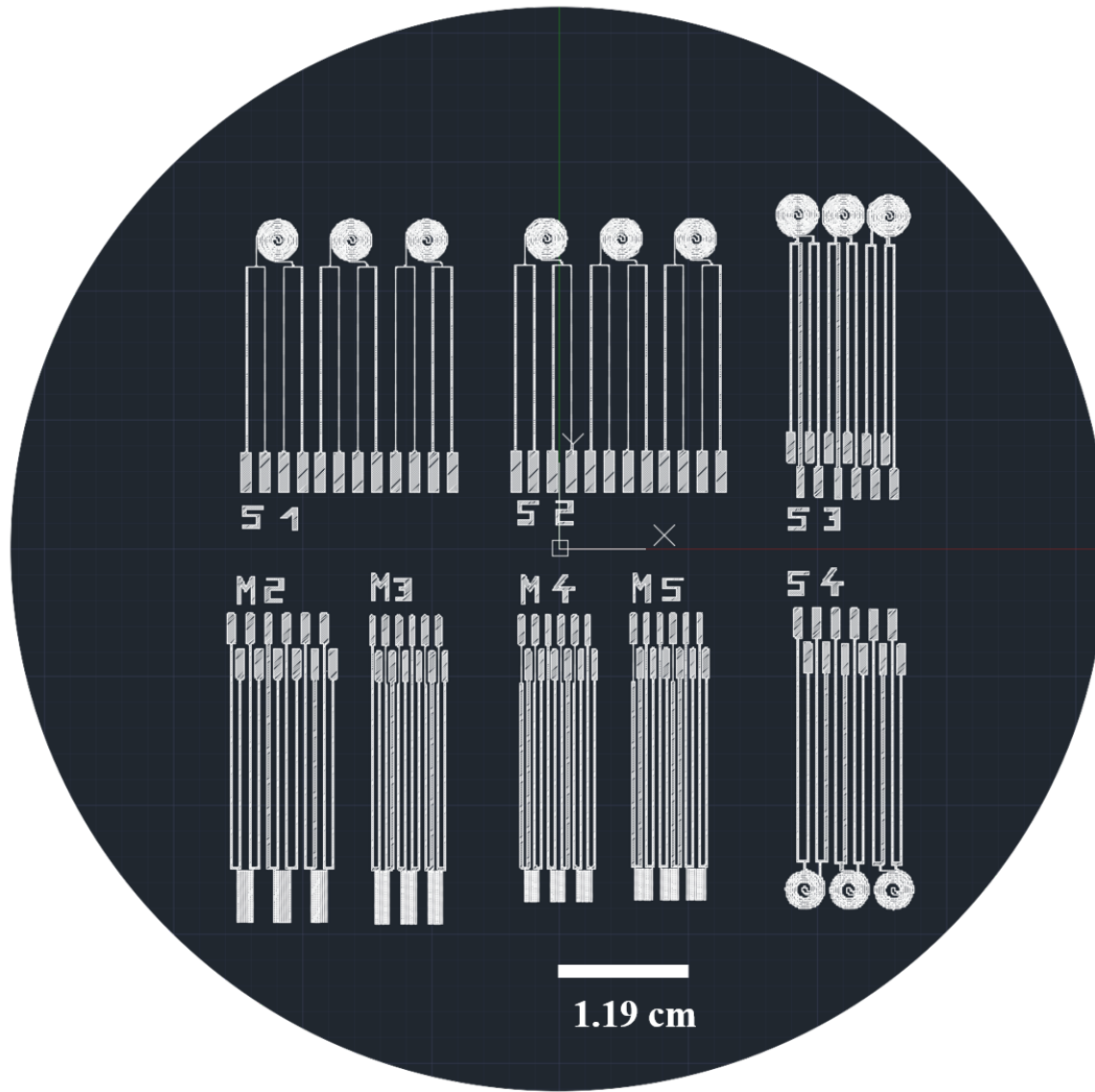


Figure 17: Wafer design

4.1 Constraints

To design the devices on the wafers, we have several constraints:

- The size of the wafer (100mm diameter) limits the number of devices we can produce on it.
- For the evaporation, the wires cannot be thinner than the photo-resist thickness ($20\mu m$). If we design wires under this limit, metal is no longer uniformly deposited.

- We need a distance around $100\mu\text{m}$ between the sensors and heater, from section 3.
- We need four wires that connect each sensor or heater, from section 2.5.
- We need some space between devices to be able to cut between them.

4.2 Thermoresistance

We saw in section 3.1.2 that the spiral device is mechanically more robust compared to the other options. However, we decided to put both spiral and rounded serpentine resistances on our wafer, in order to minimize the risk of failure by diversification. Consequently we put four models of each type, maximizing the available space on the wafer.

We also vary the width among the devices, between 25 and $35\mu\text{m}$. The reason behind this choice is once again to minimize risk and maximize performance. In fact, if we decrease resistance width, the performance will be better as the resistance value will change with more sensitivity. However, if we decrease it too much, the risk of destroying the device during fabrication or insertion is higher. We also variate the length of the serpentine (3,5 mm), the number of serpentine (15,20) and the diameter of the spiral (3.5,4 mm). Figures 18a, 18b and 18c shows example of sensors sizing and Table 5 gives a summary of the different variations we made.

4.3 Wires

Each sensor or heater has been connected with four wires, meaning two input and two output, according to the State of the Art (section 2.5). This is needed to have higher precision measurements. The problem of this technology is that it adds constraints in term of space. The four wires must be wide enough to not interfere with the sensors, and long enough to be able to exit the tube. This leads to a large space being occupied by those wires, which reduces the space available for more devices and limits the minimal distance we can have between sensors and heaters.

4.4 Connection Pads

Since we want our sensors to be wire bonded to a PCB, we have to design pads large enough to permit this wire bonding. From technical data, we designed two types of connectors, with a big margin to be sure to match the requirements of the wire bonder. Figure 18d shows how we made a compromise between pads sufficiently large and limited the occupied space.

Sensor	Thickness Small Wire [μm]	Distance between Resistance [mm]	Length / Diameter [mm]	Number of serpentine
M2	30	1.5	5	15
M3	35	1.15	5	15
M4	35	1.15	3	15
M5	35	0.9	3	20
S1	25	1.8	4	None
S2	35	1.8	4	None
S3	35	0.3	4	None
S4	35	0.3	3.5	None

Table 5: Summary of the variations we made

4.5 References

Finally, we added reference labels on each device, so that each one could be identified even once the sensors were cut apart.

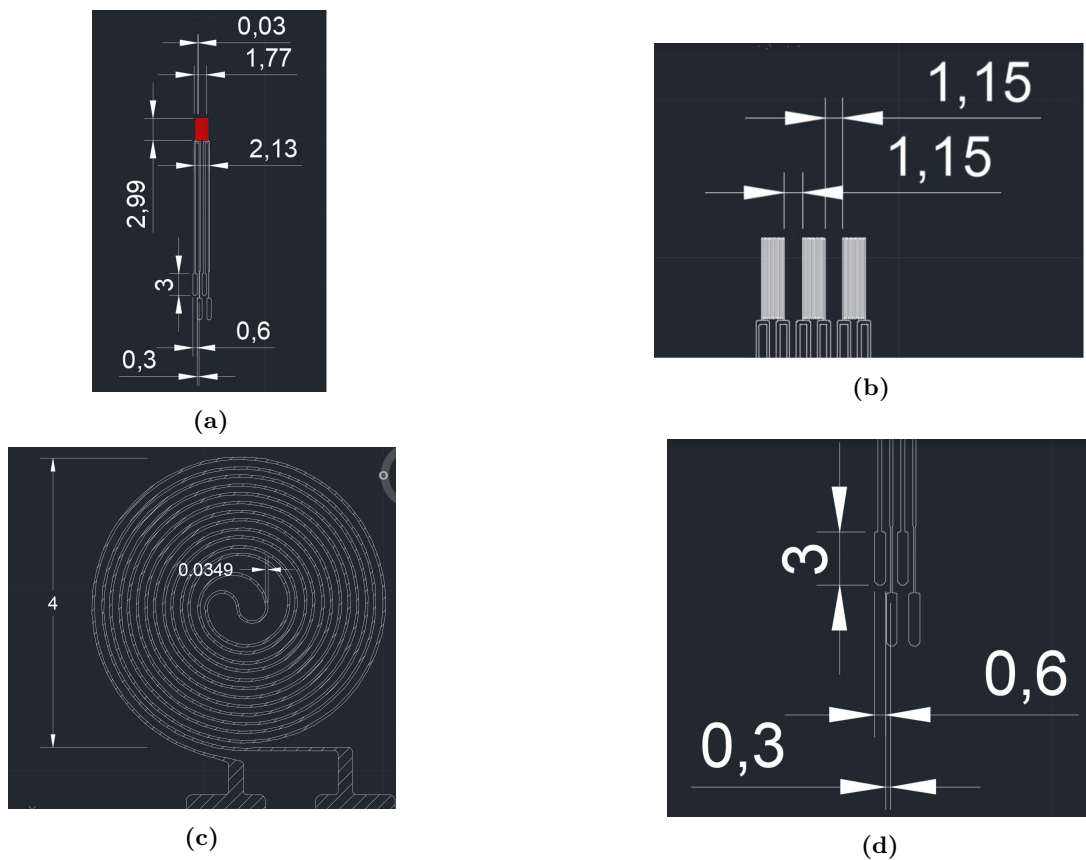


Figure 18: Example of sensors sizing. All distances are in mm. (a) Global view of a serpentine resistance (b) Minimizing the space between two resistances from a same sensor. (c) Width of $35\mu\text{m}$ to minimize risk and maximize performance. (d) Pads design. Compromise between sufficiently large for wire bonding and minimizing the occupied space.

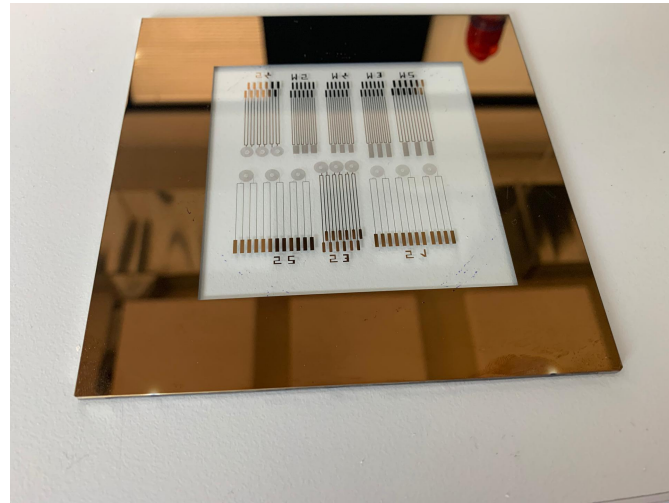


Figure 19: Chromium mask

4.6 Theoretical Value of the Resistance

We have made a graph of the resistance depending on the different size parameters for the serpentine (Figure 20). Table 6 gives the theoretical values of the different resistances according to the sizing of our sensors.

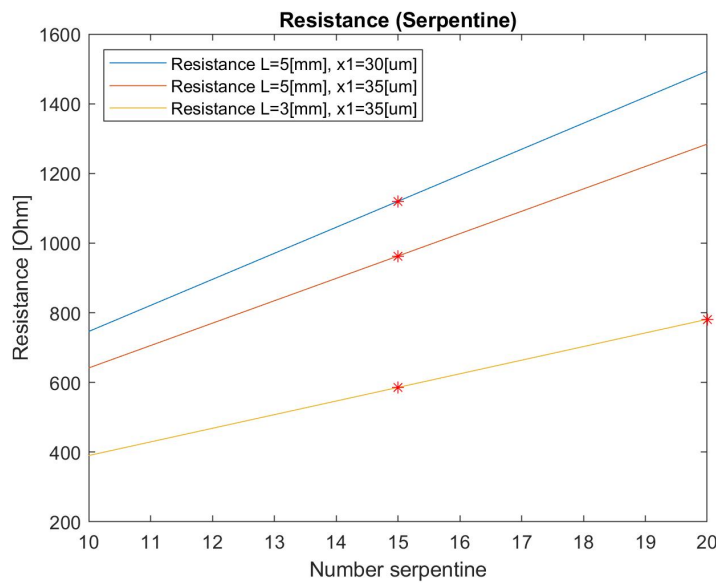


Figure 20: Variation of Resistance depending on the number of serpentine. The red point are our choice of serpentine sizing. The Matlab code to obtain these curves can be found on Figure 90 of the Appendix.

Sensor	S1	S2	S3	S4	M2	M3	M4	M5
Resistance [Ohm]	1793	867	867	718	1120	962	590	781

Table 6: Theoretical resistance of the sensors

4.6.1 Spiral Resistance

To find the theoretical value of the resistance, the first step to do is to find the area covered by the spiral, minus the area between the wires. In order to do that, we calculate the proportion of the area covered by the wires, with subtracting the center of the spiral where just take in account the half turn of the wire. Then by dividing by the thickness of the wires we obtain the length of the spiral. The we use a classical equation to evaluate the resistance :

$$\text{resistance} = \text{resistivity} * \frac{L}{S} \quad (16)$$

5 Clean Room Process

This section will describe in detail the different steps of production of our device as well as the improvements made between the various iterations and the takeaway pieces of knowledge that we learned at every step. Figure 21 below presents the general process flow. Each of these steps took place on a standard glass wafer 100 cm in diameter.

Step	Process description	Cross-section after process		
01	Substrate Preparation Pro : Lamination of polyimide Equ : PHOTOPRO33(Z12) Thi : PI (25 µm) Rem:	PI Wafer		
02	Deposition of the photoresist Pro : Lamination of ordyl (PR) Equ : PHOTOPRO33(Z12) Thi : 20 µm Rem: /	PR PI Wafer		
03	Exposition of the photoresist Pro : Photolithography Equ : Süss MJB4 (Z13) Thi : / Rem: /	Mask PR PI Wafer		
04	Development of the photoresist Pro : Photolithography Equ : Base wetbench (Z13) Thi : / Rem:/	PR PI Wafer		
05	Metal deposition Pro : Evaporation Equ : EVA760 (Z11) Thi : Ti=10nm/Pt=100nm Rem: /	Ti+Pt PR PI Wafer		
06	Lift-off Pro : Resist stripping Equ : SVC14 (Z13) Thi : / Rem: /	Ti+Pt PI Wafer		
07	Encapsulation Pro: Parylene coating Equ: COMELEC C-30-S (Z10) Thi: 5 µm Rem: Done by the CMI staff	Parylene C Ti+Pt PI Wafer		

Figure 21: Step-by-step process outline

5.1 Lamination

5.1.1 Description and Result

The PhotoPro33 (Figure 22a) is a hot-roll laminator designed for applying dry film photo-resist sheets to a wide range of materials such as stainless steel or microfabrication wafers. The first steps consists of washing the metal sheet with isopropanol, followed by lamination of a 25 micron thick polyimide film at room temperature (Figure 22b). Next, we cut a piece of 20 micron thick ordyle to be smaller than the sheet of metal,remove one side of polystyrène and hot laminated it (approximately 100°C) while ensuring that the ordyle was held during lamination (Figure 22c). The ordyle needed to be held just enough to guarantee a smooth lamination, but held no more tightly than that. Once the lamination was finished, we cut the combined layers of polyimide and ordyle in the shape of a wafer and removed this piece from the metal sheet. Finally, we taped our double-layered structure on the polyimide side onto a wafer and hot laminated (Figure 22d).

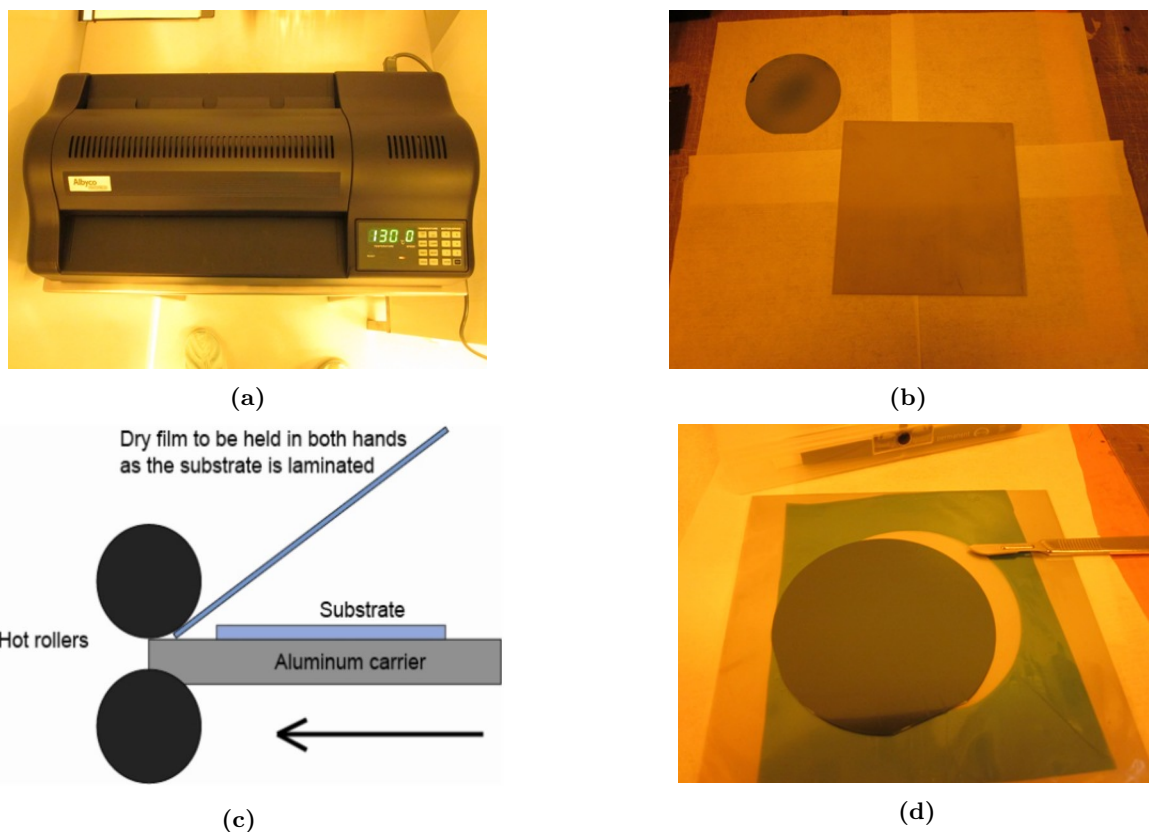


Figure 22: Photos taken from the CMI website.(a) The hot-roll laminator PhotoPro33. (b) Substrate laminated on the aluminum carrier. (c) The method for the hot lamination of the ordyl on the substrate (d) Final result of the lamination process of polyimide and ordyl.

5.1.2 Learning and Improvements

- In order to have a high quality final product, a lamination must be redone if there are small bubbles or folds. Such an imperfection could indeed have serious repercussions on our final product.
- When laminating the ordyl, it is important to not hold it too tightly, since otherwise it may tear or wrinkle.
- One way to avoid any problem of irregularity would have been to spin coat the polyimide and then the ordyl. This process would have also improved the adhesion of the polyimide on the wafer.

5.2 Exposure

5.2.1 Description and Result

The Süss MJB4 mask-aligner is a photolithography machine (Figure 23a). The MJB4 in the CMi has a default illumination setup of: intensity = 20mW/cm², i-line (365nm) illumination. The resolution is limited by light diffraction through the mask opening, and can reach a minimum of about 800 nm with thin photosensitive resists (thickness < 1 μm). In our case, this is not an inconvenience. Calibration steps will not be described here since we simply followed the steps described in the MJB4 user manual. One important thing to mention regarding the UV exposure is that the ordyl's polystyrene protective film must be left on the ordyl in order to prevent sticking to the chromium mask (the mask previously shown in Figure 19). We tested several exposure times (2.5, 2.7, 2.9, and 3.1 seconds) during the first iteration to determine an optimum that is neither under- nor overexposed. After this experimentation, we found that 2.5 seconds of exposure is optimal. After exposure it is necessary to remove the layer of polystyrene before the development step (Figure 23b) .

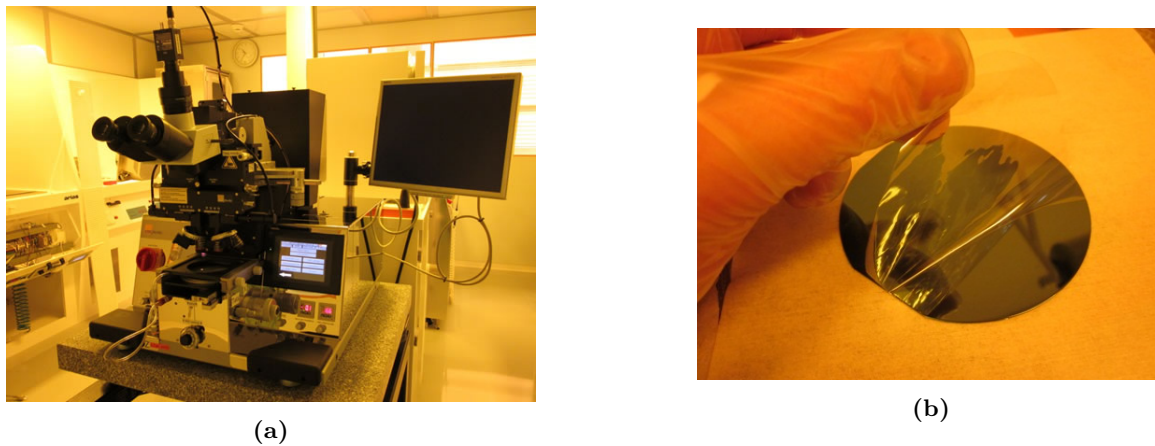


Figure 23: Photos taken from the CMi website. (a) Süss MJB4 mask-aligner. (b) Removal of the second layer of polystyrene from the ordyl before development.

5.2.2 Learning and Improvements

- The first iteration enabled us to find the optimal exposure time of 2.5 seconds. This time was then used for the second and third iterations.

5.3 Development

5.3.1 Description and Result

After exposure, the future resist mask exists as a latent image in the photo-resist: The exposed areas differ chemically from the non-exposed sites. The purpose of the development is to dissolve either the exposed (in the case of positive resists) or the unexposed (in the case of negative resists) resist areas, resulting in the final desired resist structures. In our case, the ordyl is a positive resist and the developer is a solution of 1% of Na_2CO_3 . During the development it is necessary to shake (agitate) slowly the the recipient to improve the development. After a certain time of development, the wafer is placed in the water for one minute and then dried. The first iteration was used to determine the optimal development time under the solution that is neither under- nor overdeveloped. We tested 1min, 1min30, 1min40, and 2 minutes of development. Figures 24a and 24b show the result after 1min15 of development. We clearly see that they are underdeveloped since the ordyl isn't totally removed from the exposed pattern and the serpentine lines are thinner than expected. On the other hand, overdeveloped wafers led to bigger, overlapping serpentine lines. The optimal result was produced when we developed for 1min30 for the first and second iterations and 1min15 for the third. The third iteration had a shorter development time due to a slight change in the mixture of solution.

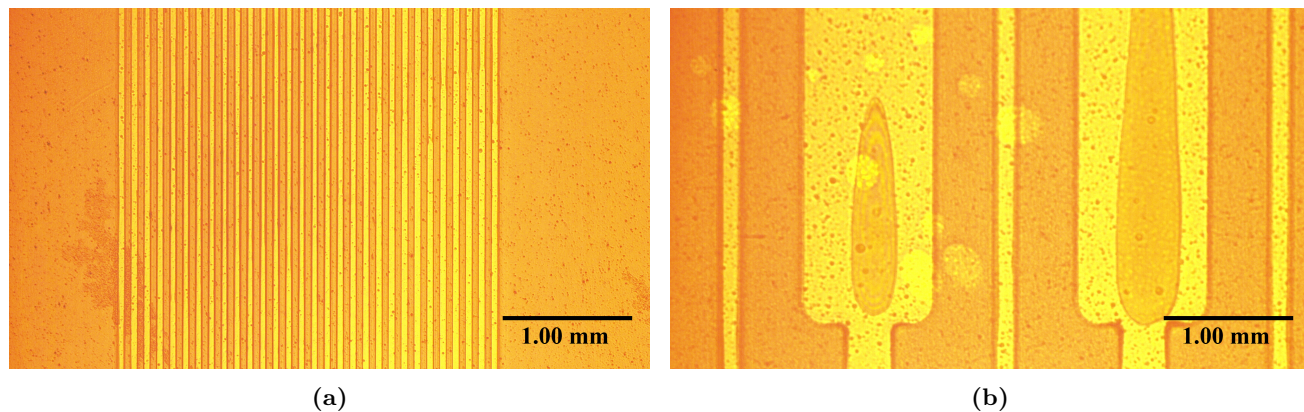


Figure 24: Photos taken by Nikon Optiphot 200 Optical Microscope with a 10x magnification lens. This is the second iteration of sensor after 1min15 of development. (a) We can see that the serpientes are under-developed because they are thinner than expected. (b) The pads are clearly under-developed since there are still filled with small areas of ordyl (the dark orange in the pads)

5.3.2 Learning and Improvements

- The first iteration enabled us to find an optimal development time of 1 minute 30 seconds. This optimal time was also used during the second iteration.
- The third iteration used a shorter development time of 1 minute 15 seconds due to a small change in the development solution.
- During the first iteration, we learned how to effectively dry using pressurized air and a paper towel. This drying prevents moisture from interfering with the rest of the process flow.
- Drying could have been even further improved by using a hot plate machine; this was not pursued, however, since only a few wafers can be dried at a time and this takes a lot of time.

5.4 Tepla Stripper

5.4.1 Description and Result

The Tepla 300 (Figure 25a) is a machine that makes a high frequency plasma to clean the wafer before subsequent processes such as the evaporation of metal. It removes air bubbles and dirt from the wafer. In the case of the first iteration, we omitted the use of this machine, which led to a poor adhesion of the metal film to the substrate after evaporation. When we applied tape on the pads and then removed the tape, it removed the entire metal film, even when we used UV tape. For the second and third iterations, this problem was solved by using the Tepla stripper. Before using the Tepla stripper, it is important to use tape in the corners of the wafer to be sure that the polyimide is correctly fixed to the wafer. Without this tape, the polyimide film would be removed (or at the very least lose most of its adhesion to the wafer) during the O_2 cleaning. The taped wafers are placed on a quartz carrier to create space between each wafer, since more space between them leads to cleaner wafers (Figure 25b).



Figure 25: Photos taken from the CMi website. (a) The Tepla 300. (b) The wafers on the quartz carrier, with enough space between them to optimize the cleaning effect of the O_2 plasma.

When we performed the Tepla stripper process on the third iteration, it produced strange results (Figure 26). It looked as if the polyimide had been exposed to a lot of heat, even though we had only programmed the process for 30 seconds at a power of 500 Watts, which is normally quite low. The reason for these bad results is still unknown even after asking the machine's manager. One thing that may have gone wrong is that the wafer was not sufficiently dried after the development process, which was done the same day as the Tepla stripper for this iteration. Moisture between the polyimide and the wafer could have produced overheating since the water evaporates instantly. In the end, this strange effect had no implications, as our sensors still worked perfectly well.

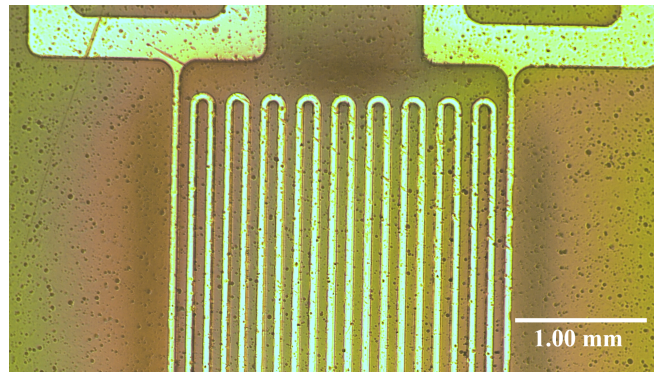


Figure 26: Photo taken by Nikon Optiphot 200 Optical Microscope with a 10x magnification lens of the third iteration after a good lift-off. It can be seen that the contours of the serpentine are lightly burnt. The reason could be that after development there was moisture between the polyimide and the wafer, causing overheating due to evaporation of this moisture.

5.4.2 Learning and Improvements

- The omission of the Tepla stripper from the first iteration led to an extremely poor adhesion of the metal film on the polyimide; when the tape was removed after encapsulation, it removed the entire metal film. This problem, which rendered our first iteration unusable, was solved for the second and third iterations.
 - The Tepla stripper cleaning could be even further improved by using it individually on every wafer rather than multiple wafers at a time. We did not use this method due to budget limitations.

5.5 EVA 760

5.5.1 Description and Result

The EVA 760 is an e-beam evaporator which uses a wide range of complex configurations (Figure 27). To use it, we had to choose the metal mixture of our choice and place a planetary dome with 8 wafers ready to evaporate. During

the first iteration we chose the mixture titanium (10nm)/gold(100nm) with a surface treatment of O_2 plasma. We initially choose this gold mixture instead of platinum because platinum was not available at the time.



Figure 27: Photo taken from the CMi website. Alliance-Concept EVA 760, evaporator, e-gun

The first attempt was a failure because the polyimide film was not fixed on the wafer; after EVA pumping, the entire polyimide film came off the wafer. To address this issue, just like we would learn in the second iteration with the Tepla stripper, we had to use tape all around the wafer to fix the polyimide on the wafer. The second attempt of the first iteration was then a success. For the second iteration, we asked Clerc Guy-François, the master of this machine, to program the setup for titanium(10nm)/platinum(100nm) with a surface treatment of O_2 plasma. Strangely, after the evaporation process of this setup, the entire wafer was full of cracks, rendering the sensors unusable since no current can pass through (Figure 28). Unfortunately, we did not notice these cracks until we attempted to measure the resistance at the end of the entire process flow. The entire first iteration was thus wasted due to this inexplicable situation. For the third iteration, we returned to the first recipe ([O_2 Plasma] titanium(10nm)/ platinum(100nm)). This led to great results.

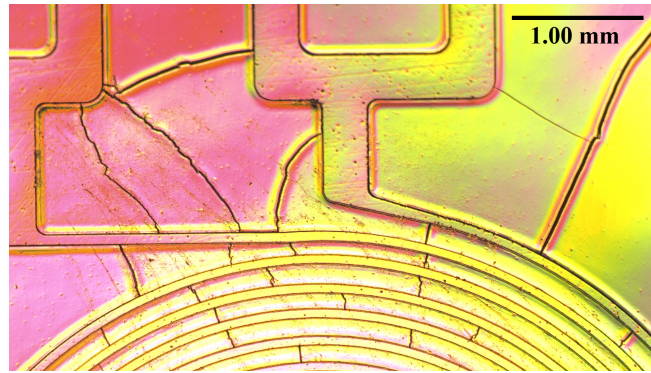


Figure 28: Photo taken by Nikon Optiphot 200 Optical Microscope with a 10x magnification lens. This is the second generation of resistance after the Ti / Pt evaporation step. Cracks are observed along the wires, preventing the current from passing through and thus rendering the resistance unmeasurable.

5.5.2 Learning and Improvements

- The first iteration taught us that it is very important to add tape to the edges of the wafer in order to prevent the removal of the polyimide during the Eva pumping step.
- The titanium/platinum mixture created cracks after evaporation, preventing the use of the sensor. This was the main reason why the second iteration failed. We can be fairly certain the failure was due to a factor out

of our control, since the other Lab in Tube group also had the same problem with this mixture.

- The third iteration was a success and thus had optimal parameters.

5.6 Lift-Off

5.6.1 Description and Result

Lift-off is a method for creating a pattern of a target material on the surface of a substrate (e.g. polyimide) using a sacrificial material (e.g. ordyl photoresist). The common stripper used is SVC-14 (DMSO). The basic procedure is to put the wafer in a container with SVC-14 and put the container in a basin of tempered water where we send an ultrasound with a certain power to lift off correctly. The three variable parameters are the time of lift off, the temperature of the water, and the power of the ultra-sound. The lift off process is the most difficult process to optimize out of all the manufacturing steps since there are three parameters that could be modified and it varies widely among the different mixtures of metal deposited. Figure 29a and Figure 29b show a sample of the first iteration without enough lift off. We can see large amounts of residual ordyl that cannot be removed by hand with a cotton swab. These residual deposits will result in problems during the encapsulation step, leading to unusable sensors. Figure 29c and Figure 29d show a sample of the third iteration with too much lift off. It produced holes in the pattern, destroying the sensors.

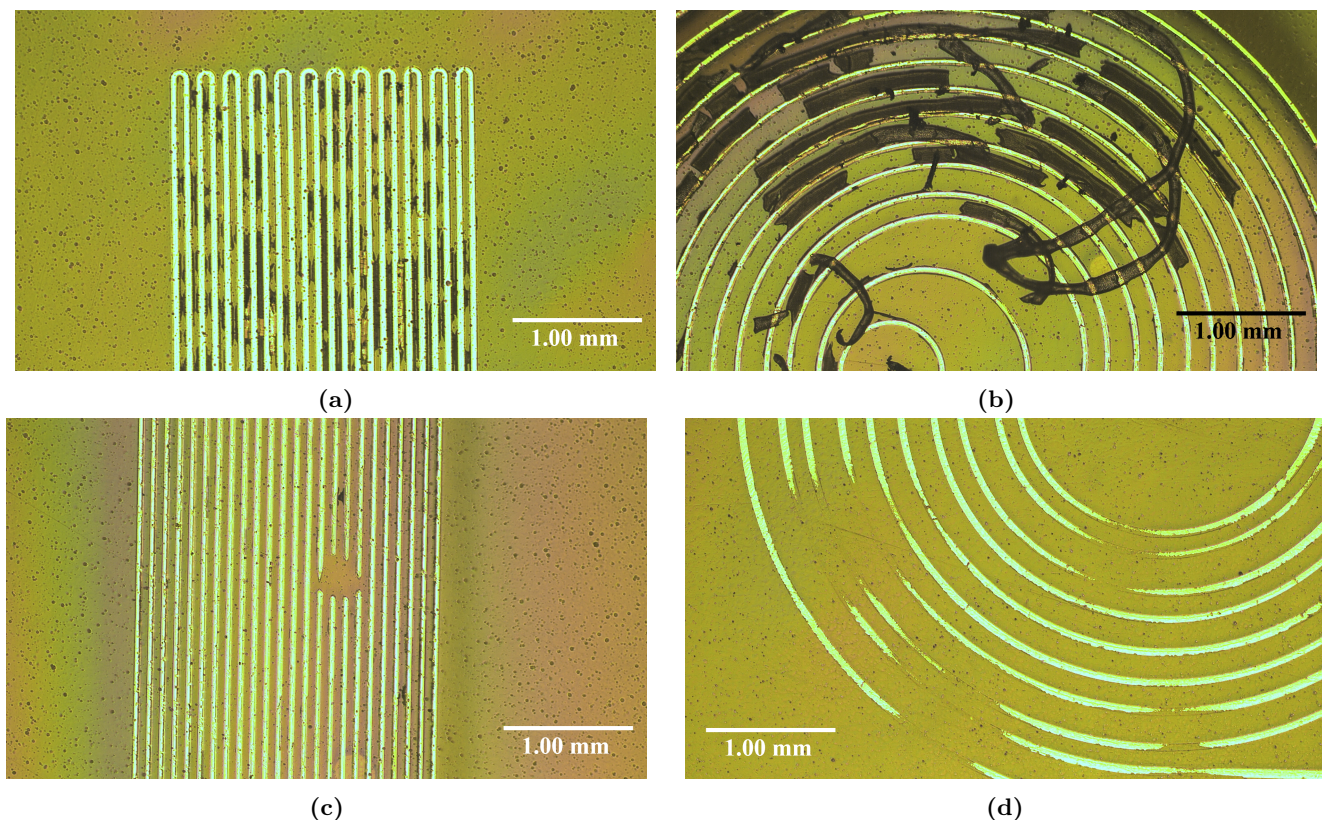


Figure 29: Photo taken by Nikon Optiphot 200 Optical Microscope with a 10x magnification lens. (a & b) First iteration on a wafer without enough lift off. Between the serpentine and the double spiral we can see ordyl residues. (c & d) Third iteration on a wafer with too much lift off, creating holes in the metal film pattern.

During the first iteration we used water at 75°C, and regardless of the power level or time of lift-off, this warm water produced many holes in the pattern of our device. This was due to the fact that gold becomes soft at very low temperature. When we reduced the temperature to 55°C, the hole problem mostly disappeared. For the rest of the time we used this temperature as a fixed variable of the lift off. We made many variations of the time and the power level. At the end we saw that a power level of 3 (which is the medium power) gives the best result and the time of the lift off varied for each wafer. When the lift off was visually acceptable, we removed the wafer from the SVC stripper and cleaned it. Generally the lift-off took between five and seven minutes for the gold and between

two and three minute for the platinum. The lift off of the platinum took less time because the many cracks of the iteration made lift-off easier. We can see in Table 7 the results of the third iteration after lift off. After measuring the three resistances of each device, we obtained 10 usable devices. Figures 30a and 30b shows two resistances that are usable after lift off.

Wafer No	S1	S2	S3	S4	M2	M3	M4	M4
3_1		2/3 Ok						
3_2			2/3 Ok		Perfect			
3_3		2/3 Ok			2/3 Ok	Perfect	Perfect	2/3 Ok
3_4		2/3 Ok	2/3 Ok		Perfect	Perfect	1/3 Ok	1/3 Ok
3_5		Perfect	Perfect	Perfect	2/3 Ok	1/3 Ok		
3_6		Perfect	1/3 Ok	Perfect	1/3 Ok	1/3 Ok		
3_7			1/3 Ok	1/3 Ok	2/3 Ok			
3_8		1/3 Ok			1/3 Ok	1/3 Ok	1/3 Ok	

Table 7: Success rates of all sensors from all eight wafers of the third iteration. For all the wafers of this iteration, we used a temperature of 55°C and a power level of 3 for the lift off. The time varied between 5 and 7 minutes for the wafer. The black box means that all the sensors of the device are broken. Green means the sensors are fully usable. The white boxes give the number of working resistances in a partially functioning sensor.

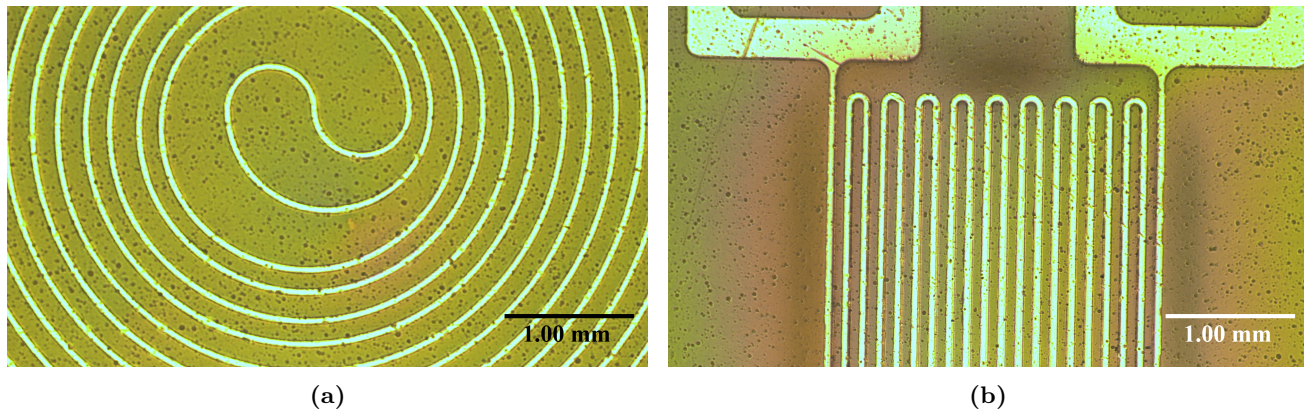


Figure 30: Photo taken by Nikon Optiphot 200 Optical Microscope with a 10x magnification lens. (a & b) Two good resistances after the lift off process. The resistance values are measurable.

5.6.2 Learning and Improvements

- The temperature should not be too high because the gold becomes too soft and holes appear easily.
- Because of the cracks in the second iteration, the lift off only took between 1 and 2 minutes.
- If there are a few small residual spots of ordyl, it is possible to remove them by hand with a cotton swab, salvaging the device. Bigger spots cannot be removed.

5.7 Tape

5.7.1 Description and Result

Before the encapsulation of parylene, it was necessary to put some tape on the pads of all our sensors. This tape enabled us to removed the parylene barrier from the pads, making them accessible for readings. Initially we used normal tape on our pads, but we quickly saw that all of the metal was removed with the tape (Figure 31). We then decided to instead use UV tape, which worked perfectly with the second and third iterations. The first iteration was a good opportunity to learn of this problem anyway, since the adhesion of the metal was too poor even for the UV tape. The UV tape has a better adhesion when it is not exposed to the UV light; after two minutes of exposure, it no longer adheres.



Figure 31: Removal of the standard tape on the first iteration pads after encapsulation. The entire metal film came off with the tape.

5.7.2 Learning and Improvements

- The UV tape is the solution to protect the pads from the encapsulation layer and avoid the removal of the metal film from the substrate.
- Another option to remove the encapsulation from the pads would be to dry etch the parylene through a mask in the zone of the pads. We did not use this method because we were not trained how to do the etching, as well as the fact that the tape process is free.

5.8 Encapsulation

5.8.1 Description and Result

As mentioned in section 3.3, the last step of the process is to add a protective layer of 5 micron parylene. This step was done by the CMi staff. The machine used was the Comelec C-30-S Parylene deposition system (Figure 32).



Figure 32: Comelec C-30-S Parylene deposition system

5.9 Final Result and Discussion

At the end of the entire clean room process, the third iteration produced 10 devices ready to be wire bonded and used. The values of all of these devices' resistances and how they respond to bending are described in detail in section 10.2. Figure 33 shows 5 operational devices. Table 8 gives a summary of all the variations in the setup that we have made, as well as the number of functional devices and the main problem of each iteration.

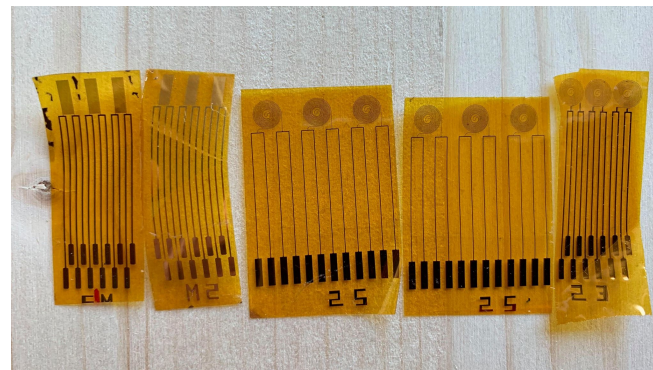


Figure 33: Five operational examples of different devices from the third generation. All resistances are measurable with a small difference between each resistance of the same sensor (about 30Ω). The sensors range from 2.62cm to 2.86cm in length depending on their design.

Process Flow	First Iteration	Second Iteration	Third Iteration
Lamination thickness Polyimide / Ordyl [μm]	25 / 20	25 / 20	25 / 20
Exposure Time [s]	2.5, 2.7, 2.9, 3.1	2.5	2.5
Development Time [s]	60, 75, 90, 105	75	75
Tepla Yes/no	No	Yes	Yes
EVA [nm]	[02] Ti/Au 10/100	[02] Ti/Pt 10/100	[02] Ti/Au 10/100
Lift Off Time [min] Power [$^{\circ}\text{C}$]	[5-12] P1,P2,P3,P4,P5 45,55,65,75	[1-3] P3 55	[5-7] P3 55
Tape Standard/UV	Standard, UV	UV	UV
Encapsulation Parylene [μm]	5	5	5
Number Device Working	2	none	10
Problem	Very bad adhesion of the metal film to the substrat because the tepla wasn't used.	After evaporation of the platinium all the wafer was full of crackles.	None

Table 8: Summary of the different parameters used for each iteration.

6 Sensor to Circuit Connection and Tube Insertion

6.1 Connection PCB

To make the interface between the sensor and the big PCB, which performs signal processing and transmission, we decided to design a small PCB to have an easily manipulable device. This permits rapid switching from one design to another with a classical connector, and also enables each sensor to be permanently soldered to its own small PCB.

6.1.1 Design

The design of the small PCB can be seen in the appendix in Figure 79. A picture of a produced one is visible in Figure 34a. The circuit was made following the large PCB requirements, and a sufficient amount of space has been left free to allow the sensor to be glued onto the small PCB to facilitate the bonding and to improve the robustness of the system.

Once the sensor was glued and bonded to the small PCB, the cable connector to the large PCB was soldered, and is visible on Figure 34b. The female part is soldered with the small PCB, and the male part of the cable can be disconnected and connected to another device if needed.

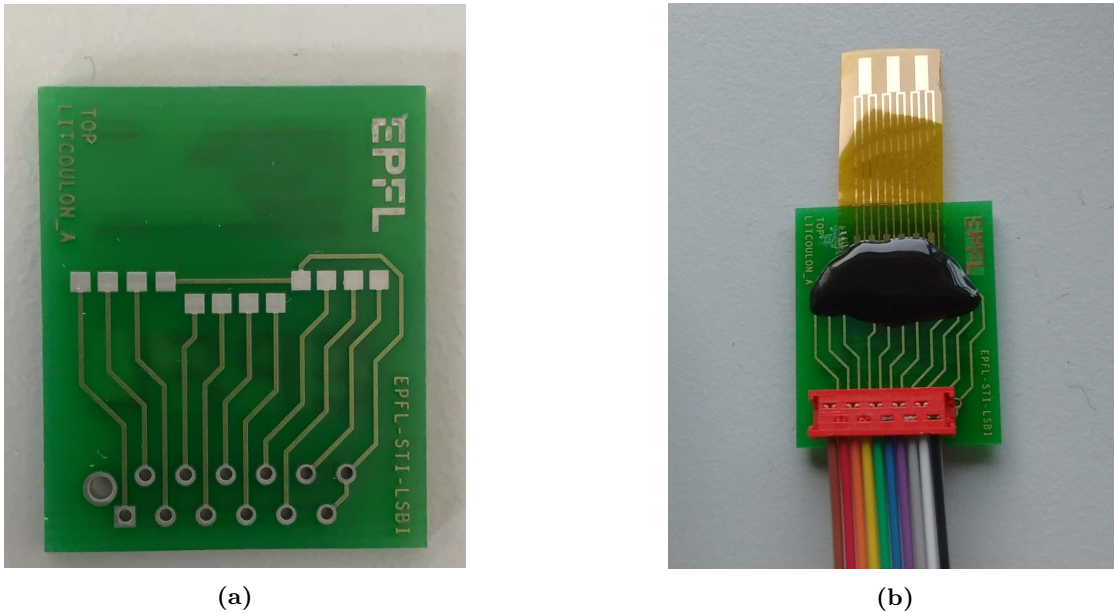


Figure 34: Connection system between the sensor and the circuitry. (a) Small PCB, which has one wire for each pad on the sensor. This PCB is 2.4cm by 2.9 cm. (b) The red plastic part is the cable connector, which is standardized among all small PCBs and is thus interchangeable.

An error was made during ordering, leading to the deposition of a tin layer which is undesirable for wire bonding. We then had to have it removed to be able to bond on the copper layer under the tin one.

6.2 Wire Bonding

Wire bonding is a technique used to make electrical connections between a PCB and a semiconductor. In our case the wire bonding allowed us to make an electrical connection between the pads of our small read-out PCB and the gold pads of our device. The wiring made by a wire (or bridge) soldered between the two connection pads provided for this purpose on each of the elements. The main advantage of this technique is that the welding is performed ultrasonically at room temperature. There is no risk of melting the substrate. The wires are made of gold or aluminum and are 25 microns thick. The wire bonder used is the TPT HB10 Wedge and Ball Bonder (Figure 35).

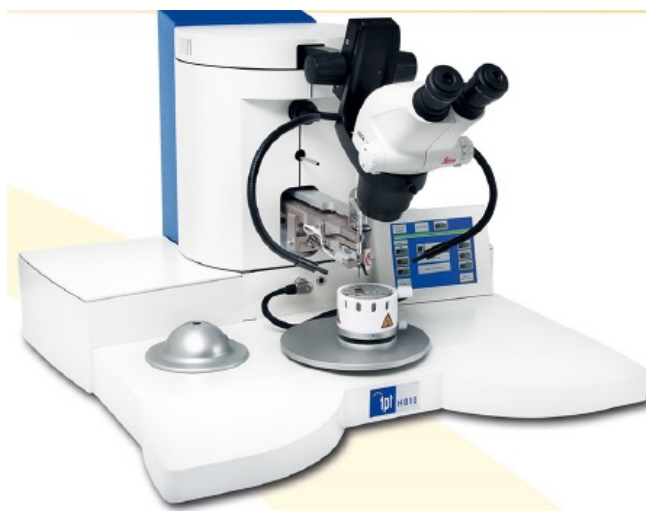


Figure 35: TPT HB10 Wedge and Ball Bonder

There are three main classes of wire bonding: ball bonding, wedge bonding, and compliant bonding. Each of them has advantages and drawbacks. In our case, the first two techniques were available at EPFL, and both were attempted on all three iterations of our device. Unfortunately, all of these wire bondings failed due to low adhesion of the metallic film on the substrate. When bonding, the metallic layer pulled off part of the pads of our device, as illustrated in Figure 36.



Figure 36: Photo taken by Nikon Optiphot 200 Optical Microscope with a 5x magnification lens. These are the pads of the second generation resistor after wire-bonding attempt. The wire bonding pads pulled off parts of the metallic film.

To solve this problem, it was necessary to add conductive Epoxy (H20E) on the PCB pads as well as those of our device to fix the wire bonding wire in place. Figure 37 shows the result of such an operation with gold wire. Once the wire was secured by the conductive glue, it was necessary to add an insulating encapsulation (Epoxy Glob-Top H70E-2) to protect the wire bonding step from the environment. This is a water resistant protective barrier. The final result, shown in Figure 37b, used wedge bonding and was successful for all of our devices. Wire bonding withstands a current of less than 500 milliamps.

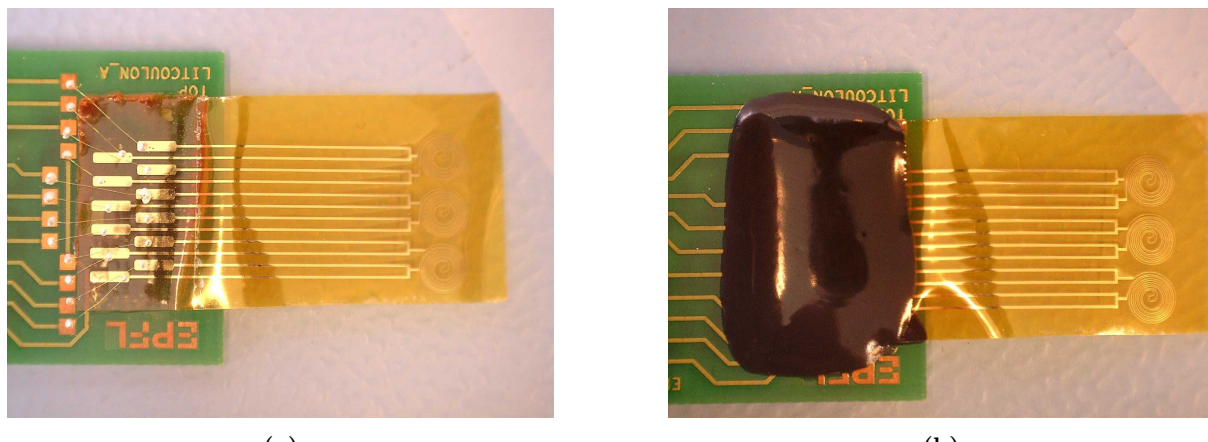


Figure 37: Photo taken without magnification. Illustration of the wire-bonding of our devices on the small PCB. (a) Wire-bonding of gold wires with conductive glue to fixed the wire. (b) Our final device after encapsulation of the wire-bonding process.

6.3 Sensor Insertion

To insert the sensor into a tube, several steps should be followed. These steps have been improved throughout the different iterations, most notably the glue used to close and seal the tube after the sensor insertion.

First, the tube needs to be cut lengthwise, forming a sliced opening as visible in Figure 38a.

Then the device is pre-rolled outside the tube (Figure 38b), and placed in that form into the tube. Once released inside the tube, the memory effect of the substrate makes the sensor still retain a rolled shape and thus adhere to the sides of the tube (Figures 38c & 38d).

Finally we apply glue with a glue gun (Figure 38e), securing the device in place and resealing the tube. The final result is shown in Figure 38f. Several glues were tried, but only the thermo-hardening one has been robust in sealing the tube. This may due to the fact that most of the other glues have to be applied between two flat surfaces in contact, whereas in our case we are closer to a situation with two perpendicular planes.

The difficulties of these manipulations is to insert without applying too much stress to the sensors. However, we did not break any of them during insertion, thanks to the procedure we followed and to the layer thicknesses we chose.

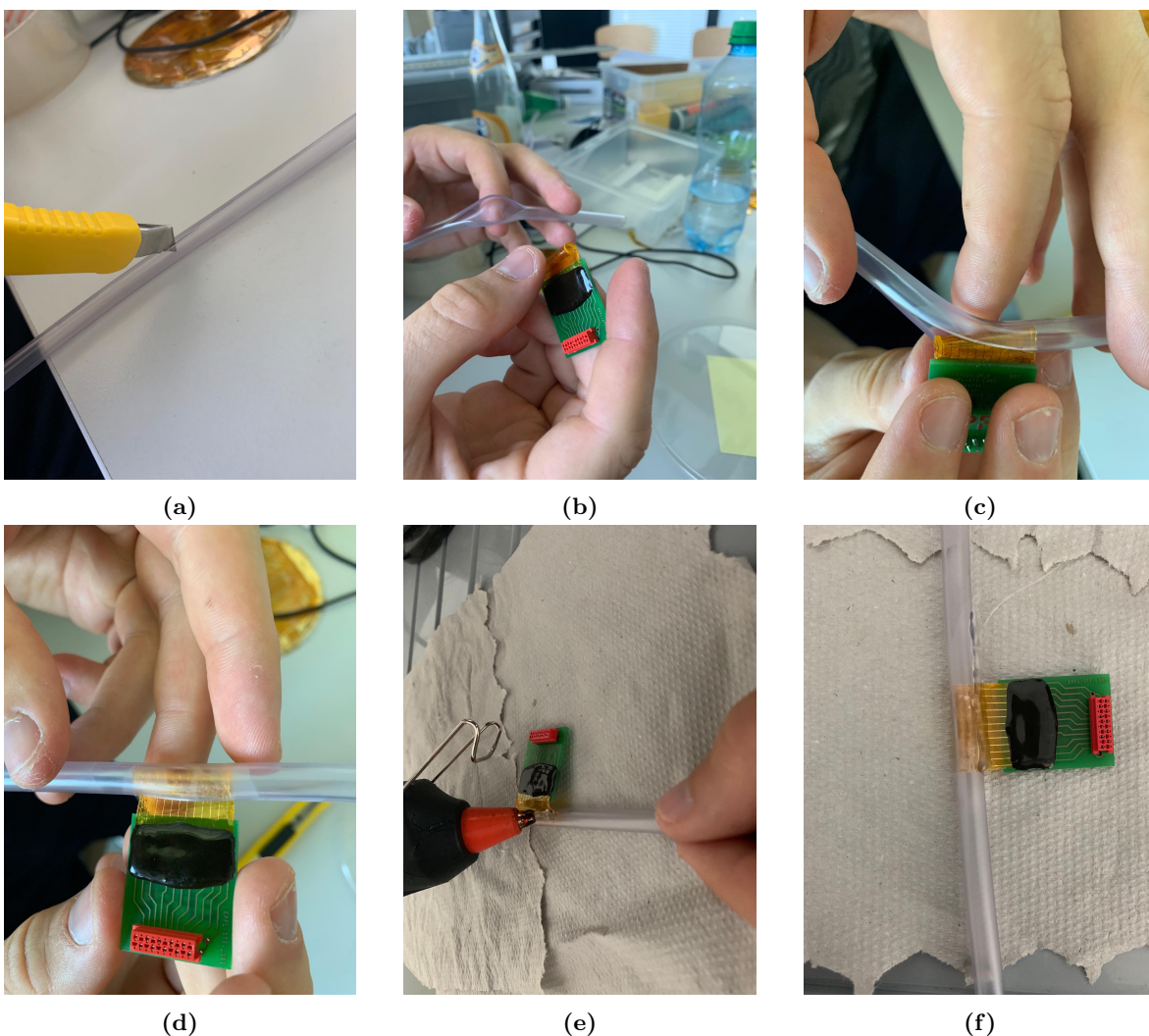


Figure 38: The steps of the insertion of our device into the tube. This method is used for the three diameters of tube (10, 5 and 2 mm). (a) Cut the tube (b) The device is pre-rolled outside the tube (c & d) then placed into the tube. (e) Finally we apply glue with a glue gun. (f) Final result.

7 Conditioning Circuit

7.1 Microcontroller and Sensors Specification

The microcontroller we are working with can acquire positive voltages up to 3.6V (see section 8). Above this point, it saturates. Therefore, in the required temperature range [35-45°C], and an accuracy of 0.1°C, the smallest detectable change of temperature would correspond to a sensitivity of $\frac{3.6}{100} = 36 \text{ mV}/0.1^\circ\text{C}$. Our final sensors are made of gold deposited on titanium. The resistivity of gold at room temperature is $2.44e-8 \Omega/m$ [52]. We have played with the number of turns and the thickness in order to obtain functional devices with a resistance of about $1\text{k}\Omega$ for serpentine sensors and 600Ω for spiral sensors at room temperature. Finally, the theoretical temperature coefficient of gold is equal to $34e-4 \Omega/\text{ }^\circ\text{C}$ [51], so at first order, the change of the resistance is $\Delta R(T) = \alpha_{gold}R_0\Delta T$ which varies between $\Delta R_{min}(\Delta T = 0.1^\circ\text{C}) = 0.34\Omega$ (serpentine), 0.204Ω (spiral); and $\Delta R_{max}(\Delta T = 10^\circ\text{C}) = 34\Omega$ (serpentine), 20.4Ω (spiral).

7.2 Circuit Blocks

7.2.1 Signal Generation

To start with, we are generating a 5V square wave of 5Hz with equal cycle duties in order to excite the sensors half of the time. It allows us to reduce the heat caused by the Joule effect ($R I^2$). Figure 39 shows the timer generating the square wave (left) and the voltage to current converter. The final current output is equal to the input square wave voltage divided by the output resistance: $I_{out} = \frac{V_{in}}{80k\Omega} = 62.5\mu\text{A}$. Again, the amplitude of the excitation current is low in order to reduce the heat effect. Unfortunately, an oversight on this circuit was made and only realized too late in the project: the current source is not independent of the load applied. For the current source to be ideal, it would require a current mirror so that the current source and the load are on different branches, and that the current generated by the current source is copied to the other branch in order to supply the load. Figure 40 is a representation of such a current mirror. Another way would be to design a current source similar to that of the heater, shown in Figure 43.

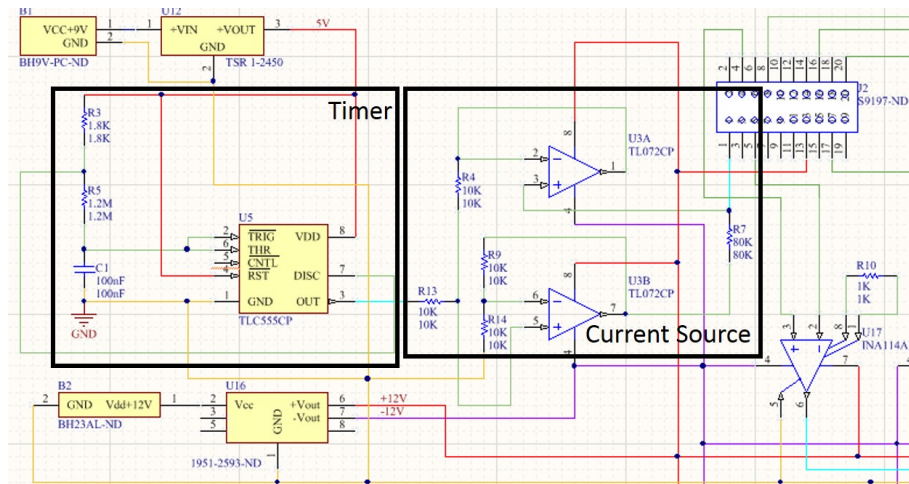


Figure 39: Illustration of Timer (left) and Current Source (right)

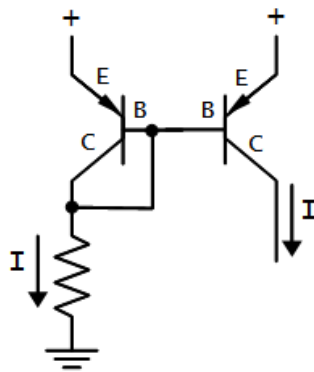


Figure 40: Current Mirror Circuit: The current on the right copies the current on the left

7.2.2 Amplification

The voltage drop at the sensors is measured via the 4-wire principle presented in section 2. The voltage drop at the sensors and at the reference resistance is amplified through a first set of differential amplifiers of gain $G_1=51$. Then the voltage difference between each RTD sensor and the reference sensor is also amplified by a second set of differential amplifiers of gain $G_2=6$. The use of differential amplifiers allows us to get rid of the common mode voltage noise as they have a high common mode rejection ratio (CMRR). The reference sensor consists of a $2\text{k}\Omega$ large turn potentiometer, to be as close as possible to the resistance of the sensors once they have been inserted into the tube and put into contact with 35°C water. As there may be a small difference in the resistance between the two sensors, the reference resistor is selected to be no higher than the smaller of the two resistances. This constraint is imposed by the microcontroller, which can only read positive voltages, and thus the amplified voltage difference must be positive. Moreover, the use of a reference resistor is well suited to get rid of the noise generated by the drift of the current since the same current is circulating through the sensors and the reference resistor. Figure 41 shows a representation of the two amplification stages.

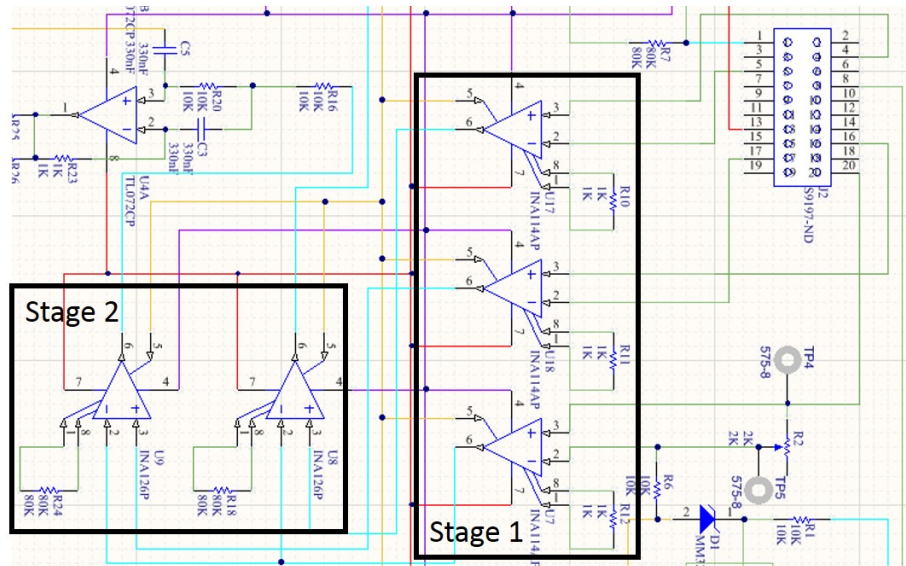


Figure 41: Illustration of the two amplification stages

7.2.3 Filtering

Finally, to get rid of the 50Hz background noise coming from the power line and the ground, we apply a third-order low pass Butterworth filter of cut-off frequency $f_c = \frac{1}{2\pi RC} = 26\text{Hz}$. At low frequency, the gain of the filter is $G_f=2$,

whereas after the cut-off frequency, it will be attenuated according to:

$$H(jw) = \frac{1}{\sqrt{1 + \epsilon^2 (\frac{w}{w_p})^{2n}}} \quad (17)$$

with $n=3$, the order of the filter, and w_p the cut-off frequency.

Therefore at 50Hz, the amplitude will decrease by a factor of 2.7, or -8.56 dB. The filter is necessary when we power the circuit with the generator and do the measurements with an oscilloscope, but also when we are using the water pumps. Indeed, the water flowing through the sensor and the pumps can be represented as a body and so a capacitor is induced between the water pumps and the water. Therefore, the 50Hz noise is transmitted to the circuit through the running water, and it causes some oscillations of the voltage at the plateau which makes the reading of the amplitude complicated. Another alternative to solve this problem would be to coat the tubes with aluminum for example and connect it to the common ground.

The gains were chosen in order to respond to the specifications. The relationship between a change in voltage and a change in temperature is:

$$\Delta V = G_1 G_2 G_f \times I_0 \Delta R \quad (18)$$

Using this relationship, the minimum voltage change corresponding to a change of 0.1°C is $\Delta V_{min} = 10.4\text{mV}$, and the maximum voltage change corresponding to a change of 10°C is $\Delta V_{max} = 1.04\text{V}$, both of which lie within the analog input voltage range of the microcontroller. It is possible to triple the value of the current in order to thoroughly exploit the range of the microcontroller, which would lead to a $33\text{k}\Omega$ resistance instead for the current source. However, because of the fabrication process, the differences in initial resistances might already reach $30\ \Omega$ or more, hence the value of the current has to be limited to lower values. Our final choice is then a $80\text{k}\Omega$ resistance. Figure 42 below shows the filter stage, situating at the output of the second amplifier stage.

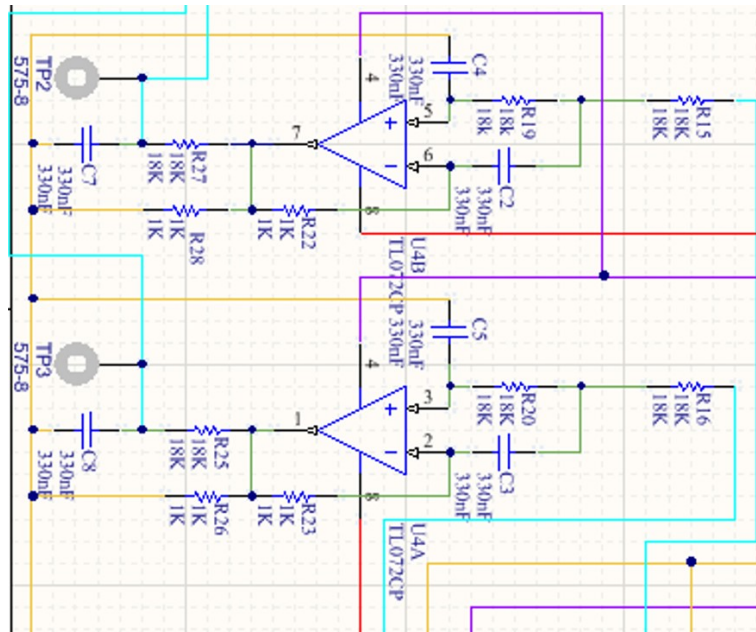


Figure 42: Illustration of the 3rd order Butterworth filter stage

7.2.4 Heat Generation for Calorimetric Principle

We are now going to look at the circuit block responsible for the generation of heat. First, as we don't want to generate heat continuously, we also generate a square wave but with a frequency of an order of magnitude lower than the square wave that excites the sensors, $f_{heater} = 0.1\text{Hz}$. Indeed, the goal is to be able to perform several measurements of the variation of the voltage amplitude at the sensors for each duty cycle of the heater. These duty cycle have unequal period, the heating period is equal to 4s while the resting period is set to 6s, as we want more time for the water and the sensors to cool down once they have been heated, through convection mainly. Finally, the square wave is converted into a current of amplitude 3 mA. The generated current feeds the heater placed at the

middle of the two sensors. However, it turns out that with this current amplitude, we can heat up the surrounding area and see the increase in amplitude of the two sensors, but once it is inserted into water, the amplitudes remain unchanged. This is due to the fact that water has a higher heat capacity than air, so water absorbs the heat faster and more effectively than air, leaving no nearby heat for the temperature sensors to read. Therefore, we need to increase the current amplitude to 6mA or more as other literature sources have done [53]. Figure 43 below depicts the timer (bottom) along with the current source (top). We are going to record how the amplitude of one sensor is varying with respect to the other sensor, in order to extract information on the direction of the flow and its velocity.

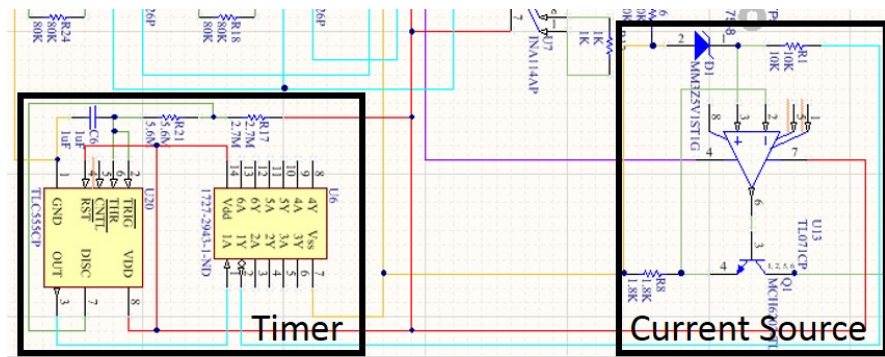


Figure 43: Illustration of the 0.1Hz timer (bottom) alongside with the 3mA current source (top)

7.3 PCB Design

Our final goal was to have a portable device which is independent from the power line. Therefore, we decided to mount our circuit on a PCB. There are two battery holders, one for a 9V battery and the other one for a 12V battery. They are then connected to DC-DC converters in order to provide the necessary power to our circuit. We have a 5V output utilized for the generation of the square wave that will excite the sensors; then we have a $\pm 12V$ output to supply the amplifiers and to generate the square wave for the heater. Finally, we add decoupling capacitors to prevent the circuit from oscillating at very high frequency, for example during the transition from the low to high value of the square wave, which is on the order of a few MHz. Figure 44 below shows the final schematic of the circuit for the PCB. Once the schematic of the PCB was completed, we contacted the ACI laboratory at EPFL to manufacture the PCB. The components to be soldered to the PCB were ordered on Digikey Electronics and Mouser Electronics. The outline of the PCB and the PCB with the soldered components are shown on Figures 85 and 86 of the Appendix.

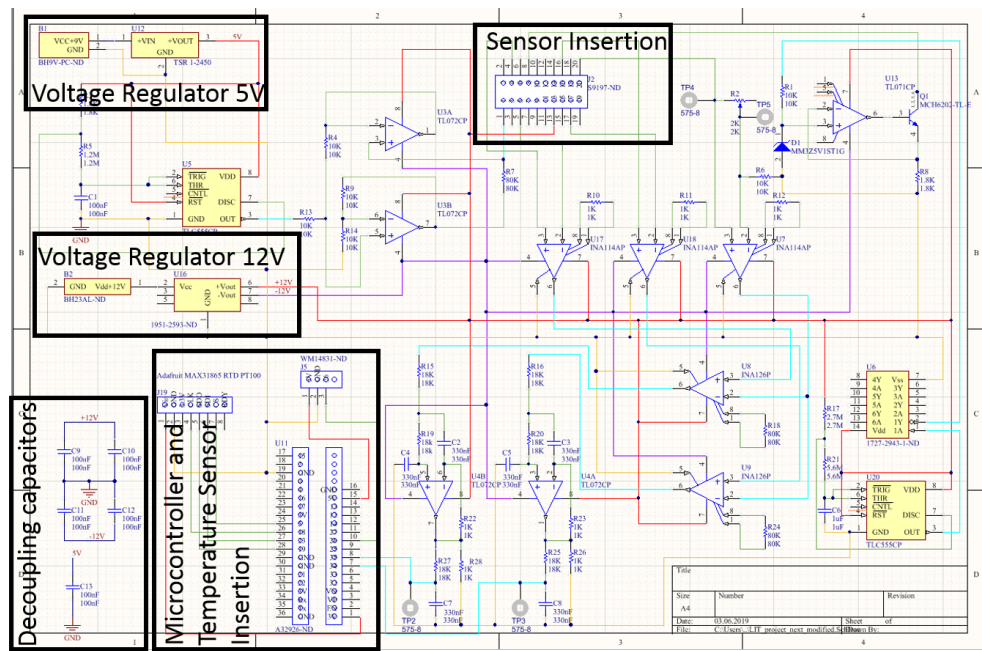


Figure 44: Illustration of the schematic of the circuit for the PCB

7.4 Noise Analysis

Thanks to the differential amplifiers and the filter stages, we have greatly reduced the 50Hz noise as it can be observed in Figure 45, where the yellow curve represents the surrounding noise when we hold the wire in our hand, whereas the blue curve is plugged into the output of the filter stage. During experimentation, some random noises appeared in the signal, and this noise is increased when self-powered devices like computers are placed in proximity of the circuit, or when we plugged electronic devices other than the oscilloscope or the power supply into the power strip. In Figures 46 and 47 is a representation of the random noise added to the signal with more or less disturbing electronic devices around the circuit. Moreover, this random noise can also be due to movements of the wires connecting the sensors to the circuit. The random noise might lead to instability of the measurements if it occurs too frequently, but it can be greatly reduced by averaging or sampling, as its frequency is much higher than the baud rate of the microcontroller. We have tried to limit the number of wires on the board as much as possible in order to minimize this noise. Finally, we have twisted the wires from the oscilloscope and the power generator in order to reduce the influence of the magnetic field.

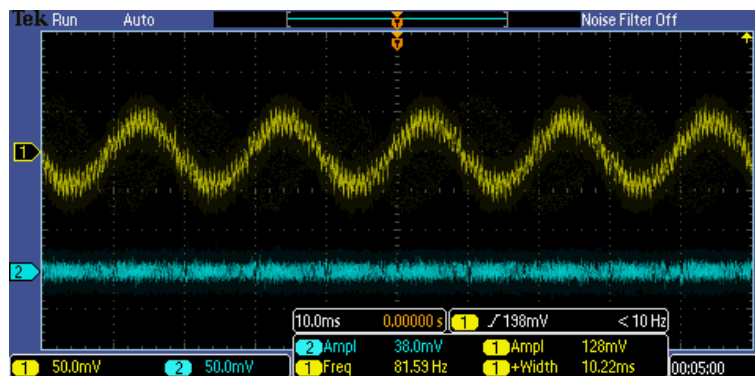


Figure 45: Comparison between the display of a wire placed in the surrounding (yellow), with a display of a wire inserted after the filter stage (blue)

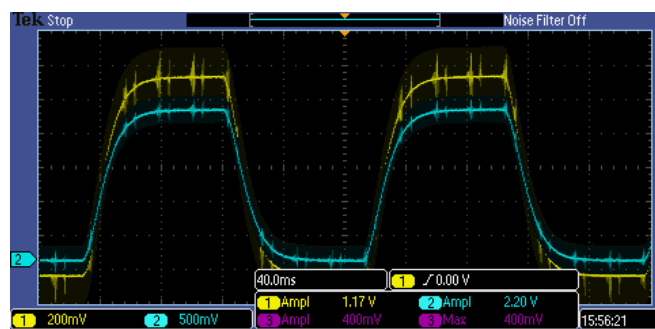


Figure 46: 5Hz signal waves when the circuit is surrounded by several electronic devices like a computer or a kettle, leading to random noise addition

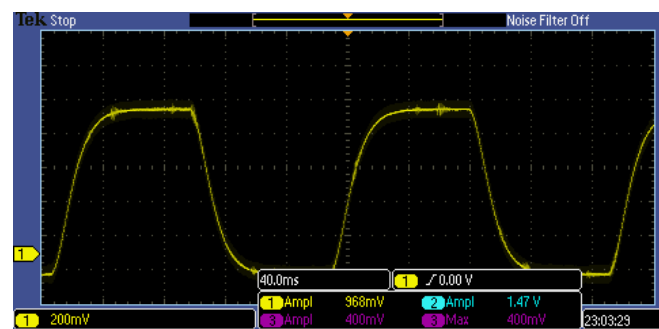


Figure 47: 5Hz signal waves when the circuit is not surrounded by electronic devices like a computer or a kettle. Therefore, the random noise is reduced

8 Microcontroller and Interface

The sensor data is now at a stage where it is ready to be sampled, interpreted, and displayed on a graphical interface. The main questions faced were how to transfer the data from the read-out circuit to the computer and how to display the data on the computer.

8.1 Data Transmission Method

There were two main choices for transmitting the data between the read-out circuit and the computer: the myDAQ, a student-oriented plug-and-play data acquisition device from National Instruments, or any type of microcontroller. The microcontroller was selected initially, reconsidered mid-way through the project, but then kept for the final device.

8.1.1 Microcontroller Specifications

We explored the options for easily obtainable microcontrollers that satisfied the project's needs, and there was one clear winner. The ESP32, a recently-released board from Espressif Systems, goes far beyond the requirements of our system and is also extremely cheap. Specifically, we acquired the WEMOS LOLIN32 board, which has an ESP-Wroom-32 chip. This microcontroller initially caught our attention due to its on-board WiFi and Bluetooth capabilities, opening up the possibility of wirelessly transmitting our data to the computer. This functionality in addition to the small size of the board (58mm x 25.4 mm) makes our design cleaner and more portable, an attractive setup. The board also has numerous input pins with a 12 bit successive approximation register analog to digital converter (SAR ADC), providing lower power consumption, higher resolution, and a more linear relationship between the voltage input and the ADC output than the average microcontroller. Large amounts of memory on the board and its quick internal clock sealed the deal on selecting the ESP32.

8.1.2 Comparison to the myDAQ

Now that the specific microcontroller had been selected, a direct comparison of the ESP32 to the myDAQ was possible. This comparison became necessary when issues with the microcontroller arose.

The myDAQ had the upper hand on two key features: its ease of integration with the LabVIEW interface and its range of readable voltage inputs. Since the myDAQ is designed for students, many online tutorials explain how to easily extract the data from it and display it in LabVIEW. The method for how to process and display the data was not readily apparent, but the importation of the data was quickly attainable. In contrast, microcontrollers are not as commonly used as data inputs for LabVIEW, so the integration was less straightforward. Besides simplifying the LabVIEW integration, the microcontroller posed a larger challenge to use in general, since the ESP32 is still an up-and-coming board and is used more by developers at this point, thus leading to a smaller online resource base for help compared to the highly popular Arduino line of microcontrollers. This was a necessary tradeoff in order to gain the wireless functionality.

The myDAQ was also greatly advantageous in that it can read voltages in the range of -10V to 10V, enabling the opportunity for a much higher resolution of our data than the ESP32's 0-3.6V range. This issue was eventually circumvented by designing the read-out circuit such that all voltages fell within the microcontroller's working range, and the smaller voltage range was accepted in light of the high-resolution ADC that the ESP32 offers.

The fork in the road came when the microcontroller started exhibiting noise problems. Specifically, the instant the microcontroller was connected to the read-out circuit, the readings on the oscilloscope became much noisier, to the point of being intolerable. The microcontroller was nearly abandoned at this point, until a consultation with a professor led us to realize that the noise was simply due to the microcontroller being powered over USB by a computer. By using the ESP32's integrated lithium polymer battery interface, we switched to powering the board by battery instead, which ultimately eliminated most of the added noise.

Besides its small size and wireless functionality, the microcontroller offers two additional advantages over the myDAQ. Firstly, the data values transmitted are not confined to any preset National Instruments settings, expanding the range of possibilities for how we process and send our data. Secondly, using a microcontroller enabled easy integration of external flow and temperature sensors, the specifics of which will be discussed in Section 9. These sensors were key to calibrating our device and constantly monitoring its performance.

8.1.3 Bluetooth Transmission

To take advantage of the ESP32's wireless capability, the data can be sent using either WiFi or Bluetooth. WiFi was the initial choice since it provides the opportunity to access the data from several devices at once, setting the stage for potential neat applications like monitoring the sensor's data from a phone. This quest was abandoned when we realized that the WiFi network on the EPFL campus requires special user input, preventing the microcontroller from accessing the network. Thus, Bluetooth was pursued. This method works cleanly, sending the data as comma-delimited strings to the computer where LabVIEW then parses them into individual values. Although wireless transmission is slightly slower than a wired connection, it was chosen in favor of its portability.

8.2 LabVIEW Interface

LabVIEW, a data acquisition and display software from National Instruments, was chosen as our display interface due to its breadth of data processing functionality which serves our purposes well. With this in mind, we designed an interface to effectively process and show our device's readings (Figure 48). Block diagrams of this interface are available in Section 13.

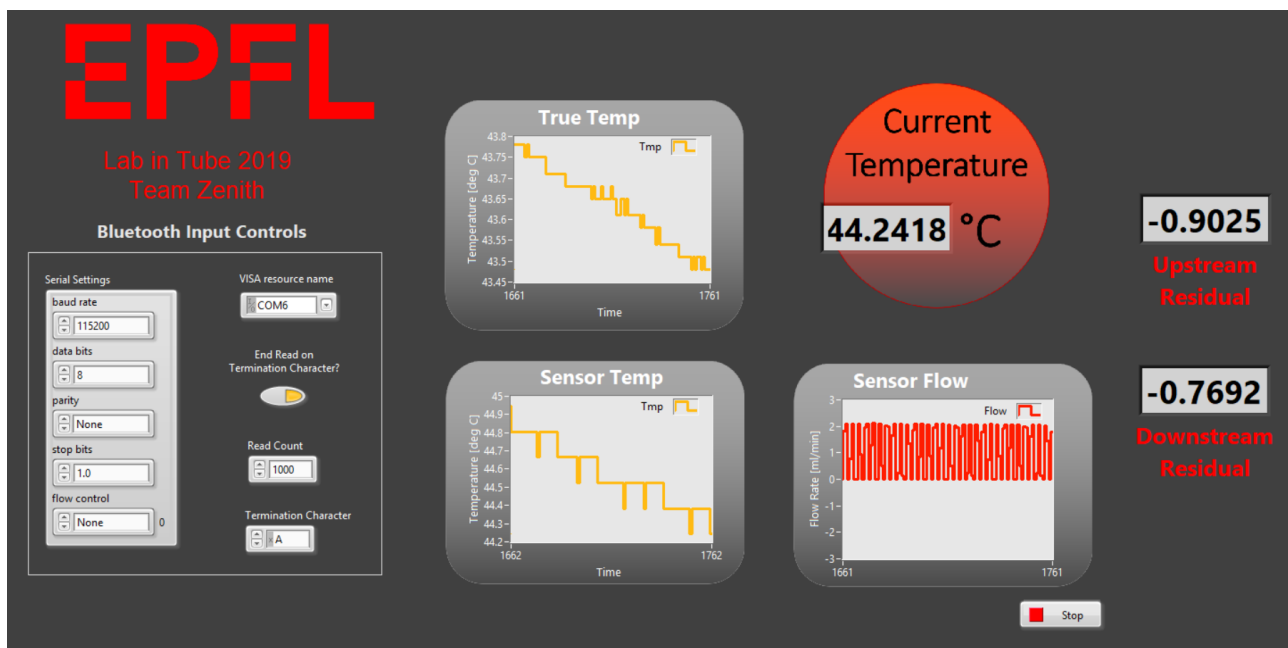


Figure 48: Screenshot of the LabVIEW demonstration interface while sensors and calibration methods were still being optimized. The residuals are calculated as the difference between the true temperature and the temperature from the calibrated sensors.

8.2.1 Receiving the Data

As mentioned previously, the LabVIEW interface receives the data as comma-delimited strings over Bluetooth. In each string sent, there is a true temperature from the external temperature sensor (see Section 9) and a voltage for each of the device's two temperature sensors. This real-time data is only imperceptibly delayed by the microcontroller code which reads and processes the values, and by the time taken to send the values over Bluetooth.

The incoming voltages are in the form of square waves, where approximately eight time points correspond to one wave. The true data lies in the amplitude of the square waves. To extract this amplitude from the real-time data, one wave's worth of points is stored in an array for each of the three metrics, and this array is continuously updated as each new square wave comes in. These voltage amplitudes are then used in the next step: calibration.

9 Setup and Calibration

The completed device was integrated into a setup with water to test its capabilities. The two temperature sensors (upstream and downstream of the heater) were calibrated first, followed by calibration of the flow sensing. Figures 83a, 83b and 83c in the appendix show our testing setup.

9.1 Temperature Calibration

Since the temperature sensors are the simpler aspect of our device, they are able to function in a wider variety of environments and thus can be tested in multiple setups. To gradually explore the functionality of our sensors, then, we increased the complexity of testing in steps. The temperature sensors were first tested by leaving the sensor flat in a petri dish of water on a hot plate. We then inserted them into a tube and analyzed them with stagnant water, where temperature was altered by pouring in water from a boiler. Finally, we flowed water at various temperatures through the tube.

9.1.1 Platinum Calibration Sensor

Considering that the only output from our microfabricated sensor is a series of voltages, we needed a way to correlate these readings with temperature values. Taking advantage of the fact that we already had a microcontroller integrated with our system, the selected temperature sensor was a platinum RTD from Adafruit Industries, made for use with microcontrollers. This sensor, which reads a larger temperature range and has a better resolution than required for our sensor, has a nominal resistance variability of $3.85 \Omega/\text{ }^{\circ}\text{C}$, where the resistance is 1000Ω at $0\text{ }^{\circ}\text{C}$. This small difference in resistance is fed into an amplifier. The amplifier is also used to handle the 3-wire setup, a similar configuration to our device in that it compensates for the resistance of the connecting wires.

A platinum RTD was clearly the best choice among temperature sensing technology since the measurements are repeatable, stable, and more accurate than thermocouples, an alternative technology. It also enables the use of the 3-wire setup. The amplifier uses serial peripheral interface (SPI) to communicate with the microcontroller, which synchronizes the serial communication between the two devices.

9.1.2 Noise Elimination

During the initial test setup where the sensor was flat in a petri dish on a hot plate, some oscillations appeared at the plateau of the square waves, making it difficult to read the voltage amplitude. Even with the filter and the differential amplifiers, the oscillations were still of the order of 50mV which would lead to errors when trying to acquire temperature. We therefore decided to add a copper plate, inserted into the water dish and simultaneously connected to the same ground as the generators (Figure 51a). This eliminated all of the 50 Hz noise. Figure 49 and Figure 50 below illustrate the two situations, with and without the copper plate. To translate this approach into the tube environment once the sensors are inserted in a tube, we jabbed two nails into the tube, one upstream and one downstream of the sensor (Figure 51b).

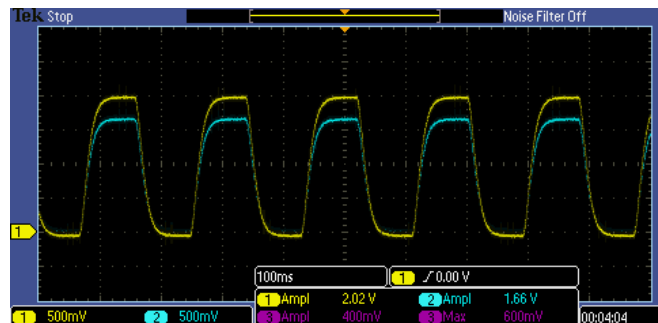


Figure 49: Voltage waves with copper plate when heating the water with the hotplate

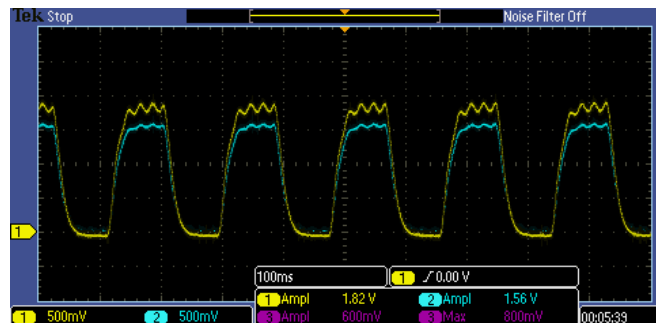


Figure 50: Voltage waves without copper plate when heating the water with the hotplate

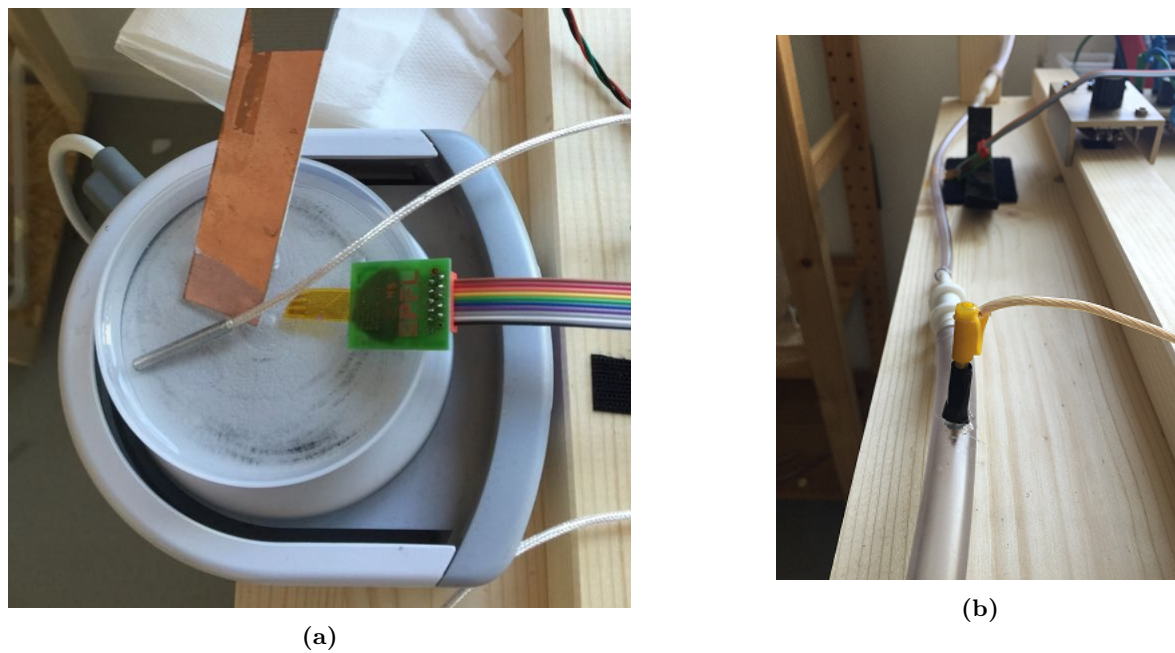


Figure 51: Method for reducing noise in the circuit. The main idea is to connect a piece of metal to the circuit's ground, then put that metal in contact with the water. (a) Copper plate used as the grounding metal in initial flat testing. (b) Nails used as the grounding metal for testing in the tube.

9.1.3 Calibration with LabVIEW vs Oscilloscope

Since temperature calibration takes time, we searched for a way to automate the process using LabVIEW. LabVIEW provides a handy method for automatic calibration through its linear fit function; this method could not easily be integrated with how the final results are displayed, so two similar but separate LabVIEW interfaces were created. The calibration interface feeds the true temperature and each of the voltage amplitudes into the linear fitting module, which gradually adjusts a linear model for each temperature sensor as more and more real-time data comes in, ultimately creating a function that maps voltage to temperature. After a satisfactory number of data points have been collected and fit with a linear trendline, the slopes and intercepts of these models are manually inserted into the demonstration interface where they are used to convert the voltage amplitudes into temperature readings.

To give an idea for how well the data is calibrated, a residual between the calibration trendline and the true temperature is calculated for each point in the demonstration interface. The mean squared error is also provided by the calibration interface, to give an idea of how linear the data is.

We compared the performance of this automated calibration to manual readings from the oscilloscopes. As we can see in Table 9, the values are similar, especially the slopes. Therefore, we can assume that the LabVIEW calibration works properly. Moreover, it may be more accurate than the oscilloscope since it acquires many more amplitude values and there is less delay for acquisition than for a person, looking at the oscilloscope display and then typing the values into Excel. Figures 52 and 53 show the two graphs obtained via the values displayed by the oscilloscope. As we can observe, there are a few points and repetitive values, which means a lack of accuracy.

Flat Sensor Calibration	Labview Calibration	Oscilloscope Calibration	Relative Error [%]
Top Slope [Celsius/V]	14.07	14.1	0.21
Top Intercept [Celsius]	19.76	18.33	7.24
Bottom Slope [Celsius/V]	13.56	13.66	0.74
Bottom Intercept [Celsius]	16.18	14.12	12.73

Table 9: Slopes and y-intercepts of calibration curves computed by the LabVIEW interface and by the oscilloscope values. The "Top" sensor is the upstream temperature sensor and the "Bottom" sensor is the downstream temperature sensor, relative to the direction of water flow.

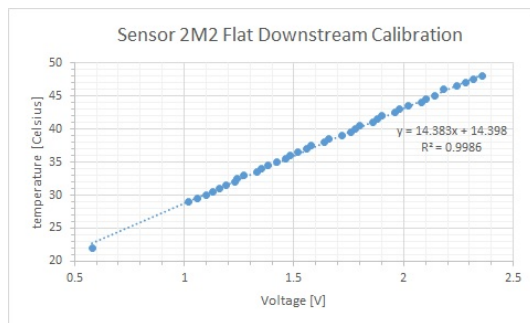


Figure 52: Linear Fitting for the bottom (downstream of heater element) sensor.

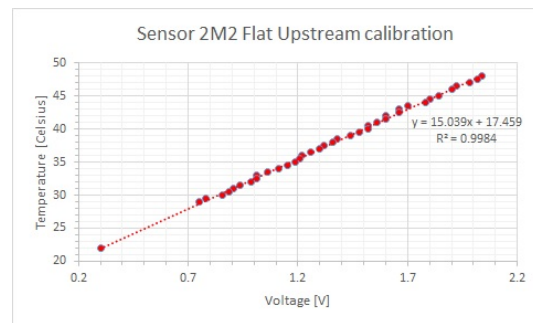


Figure 53: Linear Fitting for the top (upstream of heater element) sensor.

9.1.4 Calibration During Increasing and Decreasing Temperature

At first, we started the calibration when the water was cooling down, after having heated it up to 50 degrees. However, it seems that the behavior of the sensor is different when it heats up (Figure 54) than when it cools down (Figure 55) because we were getting diverging results from the reading of the temperature sensor when doing the simulation. Therefore, we decided to calibrate the sensors both when heating and cooling, so that the calibration is more reliable and more representative of the situations the sensor will be used in. This is applied in practice by obtaining a heating calibration curve and a cooling calibration curve, then applying in the demonstration interface whichever curve is appropriate based on whether the current temperature reading increased or decreased from the previous one. This alteration in the calibration method led to approximately a 50% reduction in the residual error when comparing the true values to the calibration curve values.

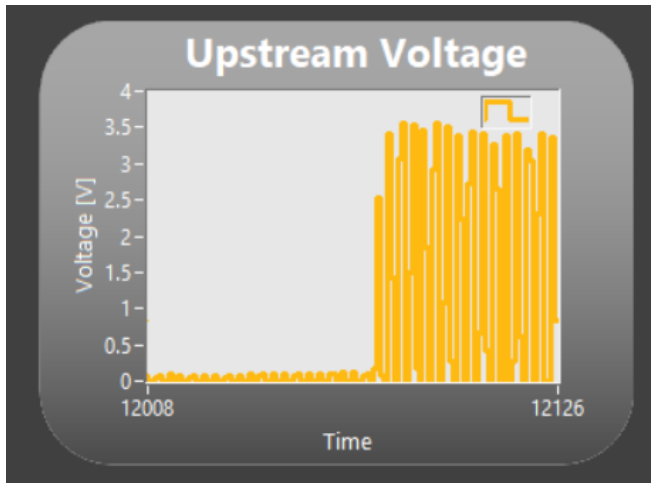


Figure 54: LabVIEW graph of the voltage readings from one of the device's temperature sensors, where the sensor started in room temperature air and then was inserted into 45°C water. Response from the sensor is nearly instantaneous.

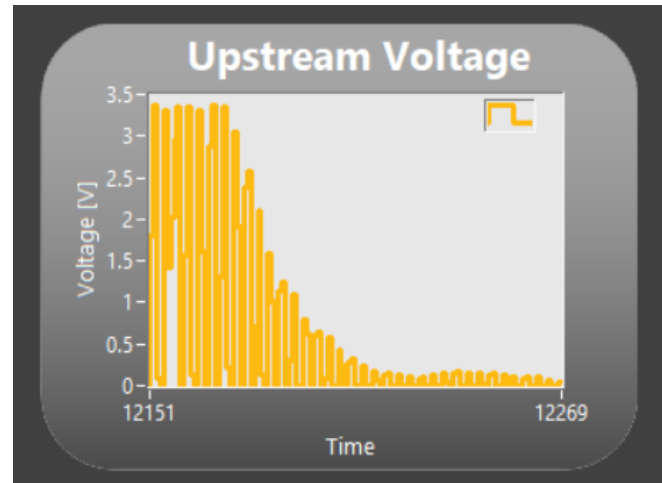


Figure 55: LabVIEW graph of the voltage readings from one of the device's temperature sensors, when the sensor started in 45°C water and then was removed from the water. The response to removal from water is slower than the response to insertion.

9.2 Flow Rate Calibration

We next turned our attention toward calibrating the flow sensor.

9.2.1 Closed Loop Flow with Torricelli Principle

To ensure our sensor has the most stable environment possible, we designed a closed loop flow system with continuous flow. The flow is driven by Torricelli's principle, which states that liquid flowing out from a hole in a tank will flow faster with a greater height of liquid above the hole. A tank was therefore mounted at various heights above

the location of the sensor to alter the flow rate. After reaching the floor, the water is collected into a basin where it is returned to the top source tank via peristaltic pumps (Figure 56). Thanks to the upper tank, we are able to eliminate the non-linearity of the pumps.



Figure 56: Torricelli tower setup. The 3 pumps on the middle shelf return the water from the collecting basin at the bottom to the source tank at the top.

In addition to altering flow by adjusting the height of the source tank, the flow rate could also be changed by opening the valve of the main tank to various degrees, which is equivalent to changing the size of the diameters of the tube, from 2 to 10mm. The flow is limited by the smallest tube in the circuit, analogous to an electronic circuit with resistances placed in series where the current is limited by the highest resistance.

We used the Torricelli principle to calculate the heights at which we should place the tank in order to obtain a given flow, with a given tube diameter. The curves of the evolution of the height of the tank with respect to the flow, with a given tube diameters are shown on Figure 57. Finally, the Matlab code to obtain these curves can be found in Figure 89 of the Appendix. We can observe that with the given flow range, and with a 2mm tube, we cannot technically go above a 30mL/s flow, otherwise it would require that the tank is placed above a 3m height.

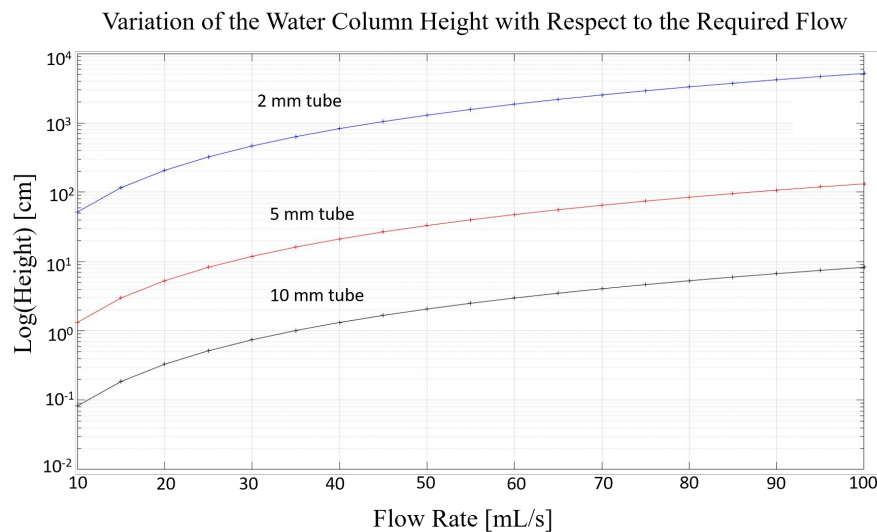


Figure 57: Computed heights of the tank, based on the Torricelli's principle, with respect to the flow, for a given tube diameter.

We then tried to compare the theory to experimental results, using a 5mm diameter tube as it is the one we would like to use to monitor flow. We used the pumps to keep the level of the water constant so that the flow is constant, and then we started a timer for one minute and measured the volume of water that had fallen. However, it turns out that for a given height, the flow is much lower than that which was calculated. The differences between theory and experimentation is shown in Figure 13b below. We think these differences are due to friction in the tube and also to the plastic connectors between the tubes which may further inhibit flow.

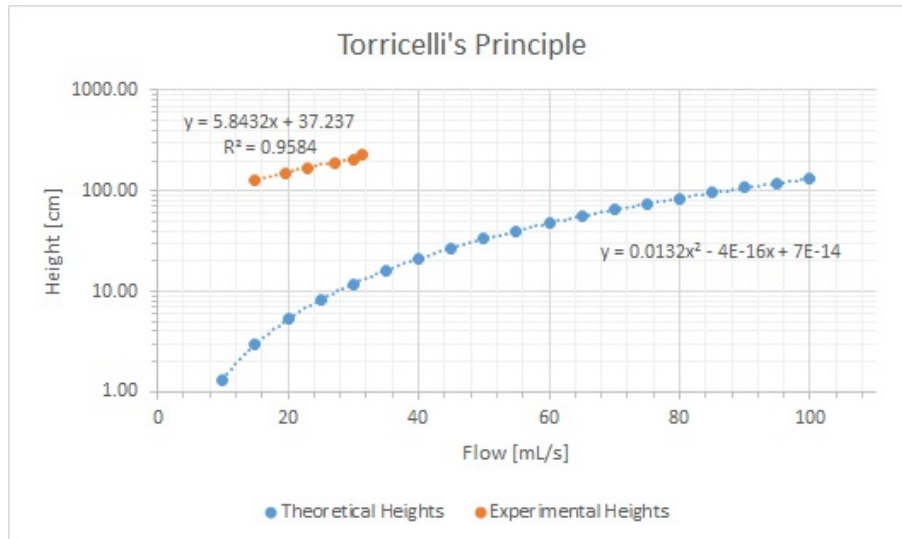


Figure 58: Computed heights of the tank, based on the Torricelli's principle, with respect to the flow, for a 5mm diameter tube along with the experimental results.

9.2.2 Flow Calibration Sensor

Working with the provided range of 10-100 ml/s for flow rates to measure, we chose the Gravity Digital Water Flow Sensor from DFRobot to calibrate our flow rate readings. This sensor uses a magnetic rotor and a Hall sensor to keep track of the number of rotations of the blades, calling an interrupt function on the microcontroller every time a rotation is detected. This rotation count can then be translated into a flow rate. The measurement range is 0.5 ml/s to 100 ml/s.

There was an administrative mix-up at the end of the project which made us think we should have looked at flows in the range of 10-100 ml/min rather than per second. Due to this confusion, the external flow sensor has not yet been integrated with the rest of the project. We attempted to instead calibrate flow by the crude method of fitting a linear model in Excel to manually measured flow rates and the differences in voltage amplitude between the two device's temperature sensors. Using the slope and intercept of this model, the device's measurement of the flow rate can be displayed on the demonstration LabVIEW interface.

10 Results

Testing and characterization of the sensor was performed gradually. The sensor was first tested while flat, then tested inside a tube without flow, and finally in the flowing tube setup. Note that the heater of the sensor could not be tested while flat, since in the petri dish of water used for flat testing, the volume of the water was too large, quickly dissipating the heat and thus giving no reading to the flanking temperature sensors. Thus only the temperature sensors were tested while flat.

10.1 Relative Differences of Sensors' Resistances

Table 10 below lists the resistance values of the upstream and downstream sensors for different generations of spiral and serpentine devices. As it can be observed, the relative difference between the two sensors' resistances is more pronounced for spiral sensors than for serpentine sensors. Indeed the relative change varies between 3 and 10% for spiral sensors, whereas it stays below 2% for serpentine sensors. This can be explained by the fact that the process flow is newer and more difficult for the spiral sensors than for the serpentine sensors. We have also compared the measured resistances with the theoretical ones computed with matlab. Sometimes, the difference increases up to 30%, and that might be due to imperfections of the process flow.

	Resistance Upstream Sensor [Ohm]	Resistance Downstream Sensor [Ohm]	Relative Difference %	Theoretical [Ohm]	Relative Change Upstream %	Relative Change Downstream %
Sensor S3	853.00	822.00	3.70	867	1.61	5.19
Sensor S4	627	584	7.10	718	12.67	18.66
Sensor 2S4	612	578	5.71	718	14.76	19.50
Sensor 3S5	873	920	5.24	867	0.69	6.11
Sensor 3S51	918	882	4.00	867	5.88	1.73
Sensor M3	1207	1202	0.42	1120	7.77	7.32
Sensor M4	777	766	1.43	590	31.69	29.83
Sensor 2M3	1196	1179	1.43	1120	6.79	5.27
Sensor 2M2	755	763	1.05	962	21.52	20.69
Sensor 3M2	761	746	1.99	962	20.89	22.45

Table 10: Data representing the relative variation of resistance between the upstream and downstream sensors within the same device. The reference for the percent difference was taken as being the mean between the upstream and downstream resistance values.

10.2 Evolution of Resistance with Mechanical Constraints

We have measured the resistances before they are inserted into a tube and after. The tubes used had three different diameters: 2mm, 5mm and 10mm. In Table 11 are recorded the resistances values before and after insertion. As expected according to simulations, the resistance of the sensors is decreasing because of being under compression. Moreover, as the deformation is more pronounced in smaller diameter tubes, we get the highest change in resistance in 2mm diameter tubes. Finally, the spiral sensors (labelled S) generally show less variation of their resistance than serpentine sensors (labelled M): it is twice as low. Ideally, we would like the calibration when the sensor is flat to still be valid when the sensor is bent; however, the change in the resistance is significant and cannot be neglected. Therefore, we need to redo calibration after insertion.

	Flat [Ohm]	Rolled 2mm [Ohm]	Rolled 10mm [Ohm]	Rolled 5mm [Ohm]	Relative Resistance Change [%]
Sensor S3 Top	875	853			-2.51
Sensor S3 Bottom	840	822			-2.14
Sensor S4 Top	627	614			-2.07
Sensor S4 Bottom	584	582			-0.34
Sensor M4 Top	777	743			-4.38
Sensor M4 Bottom	766	732			-4.44
Sensor M3 Top	1207		1194		-1.08
Sensor M3 Bottom	1202		1189		-1.08
Sensor 2M3 Bottom	1179	1160			-1.61
Sensor 2M3 Top	1196	1173			-1.92
Sensor 2M2 Bottom	763			743	-2.62
Sensor 2M2 Top	755			753	-0.26
Sensor 2S4 Bottom	578			572	-1.04
Sensor 2S4 Top	612			609	-0.49

Table 11: Data showing the variation of the sensors' resistance values after being inserted into tubes of different diameters compared to before insertion.

After insertion of one sensor into a 5mm tube, we have tried to fold the tube into different directions to see if the mechanical constraints were felt by the sensors placed inside. Indeed, we observe that the amplitude of the waves changed by 10 to 30 mV, which can lead to errors of ± 0.1 to 0.3°C in temperature measurements.

10.3 Comparison Between Theoretical and Empirical Results for Flat Sensors' Temperature Calibration

Once we have extracted the slopes from calibration, we compared them with the theoretical slopes, computed thanks to equation (19), with α_0 and R_0 being the gold temperature coefficient and the initial resistance at room temperature. Our equation is based on the fact that within the given temperature range, the alpha coefficient is constant with temperature, and that the higher order coefficients are negligible in this temperature range [52].

$$\text{Theoretical Slope} = \frac{1}{G_1 G_2 G_f \times I_0 \times \alpha_0 R_0} \quad (19)$$

In Table 12 below, we have listed the theoretical slopes along with the slopes we have obtained from experimentation. We have also listed the temperature coefficients of our gold sensors the same way. We have assumed that the gain of the amplifier stages are close to the theoretical ones (we have checked their gain doing some tests with known resistances), so that the difference in the slopes is mainly due to differences in the supplied current and the temperature coefficient of our sensors. The difference in the temperature coefficient of our sensors from the theoretical value can be explained by the purity of the gold utilized to fabricate our sensor but also by the fabrication process that is not perfect: some impurities may have been deposited on the sensors while they were fabricated. Finally, in order to compute the theoretical slopes and the temperature coefficients of our sensors, we chose as R_0 the resistance of the sensors measured at room temperature ($RT=22^\circ\text{C}$)

	Sensor 2M2 Flat Bottom	Sensor 2M2 Flat Top	Sensor 2M3 Flat Bottom	Sensor 2M3 Flat Top	Sensor 2S4 Flat Bottom	Sensor 2S4 Flat Top
Theoretical Slope [Celsius/V]	10.67	10.79	6.91	6.81	14.09	13.31
Experimental Slope [Celsius/V]	13.56	14.07	8.05	7.15	15.27	12.6
Relative Error [%]	27.03	30.43	16.53	5.00	8.37	5.32
Theoretical Temp.Coeff.Gold 290K	3.21E-03	3.21E-03	3.21E-03	3.21E-03	3.21E-03	3.21E-03
Experimental Temp.Coeff.Gold 290K	2.71E-03	2.84E-03	2.89E-03	2.95E-03	2.78E-03	2.81E-03
Relative Error [%]	15.58	11.53	9.97	8.10	13.40	12.46
Theoretical Current [uA]	62.50	62.50	62.50	62.50	62.50	62.50
Experimental Current [uA]	58.28	54.16	59.57	64.77	50.45	60.48
Relative Error [%]	6.76	13.34	4.69	3.64	19.28	3.22

Table 12: The relative error between the slopes and currents. M stands for serpentine and S for spiral.

On the table above, we can observe that 2M3 (second generation serpentine sensor) has the lowest relative errors regarding the temperature coefficient, at less than 10%. Moreover it has also low relative errors for the current flowing into the sensors. Therefore, when testing, this sensor has the best performance, followed by 2S4 (second generation spiral sensor) and 2M4. However, we don't have the accuracy of 0.1°C required. The error lies in between $\pm 3^\circ\text{C}$. The calibration curves were done in a temperature range going from 29°C to 51°C , or sometimes only up to 48°C otherwise the microcontroller was saturating. Therefore the next step is to reduce the temperature range, from 34°C to 46°C , while increasing the current by about 2.5, replacing the $80\text{k}\Omega$ resistance by a $33\text{k}\Omega$ resistance at the current source. Therefore, the difference in voltage amplitude when the temperature is changing should increase, so the residual error between our sensors and the reference sensor should decrease. Figures 59 through 64 below show the graphs obtained for all six of our sensors from oscilloscope calibrations (in blue), along with the curves obtained using the slope and intercept computed on LabVIEW (in orange). We could not store on LabVIEW the amplitude values and reference temperature values used for calibration, so the orange curve was obtained by interpolating points using the slope and intercept of the LabVIEW calibrations. The differences between the oscilloscope and LabVIEW curves can be explained by the change in the reference resistance from one calibration to the other. Moreover, some sensors have a negative offset that cannot be read by the microcontroller so the amplitude provided to LabVIEW is lower than the real one. The detailed equations for the upstream (20) and downstream (21) sensors to compute the intercept and the slope can be found in the Appendix. It is surprising that 2M2 has the most similarity between the oscilloscope calibration and the LabVIEW one; however, it has poorer performance during testing.

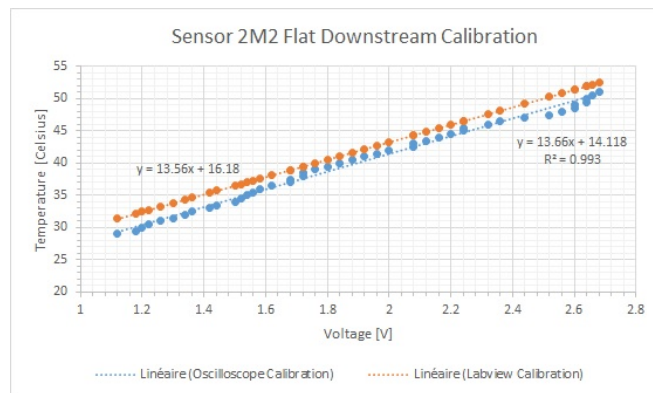


Figure 59: Calibration Curves of the 2M2 Downstream Sensor, when it is flat and put into a dish filled with water

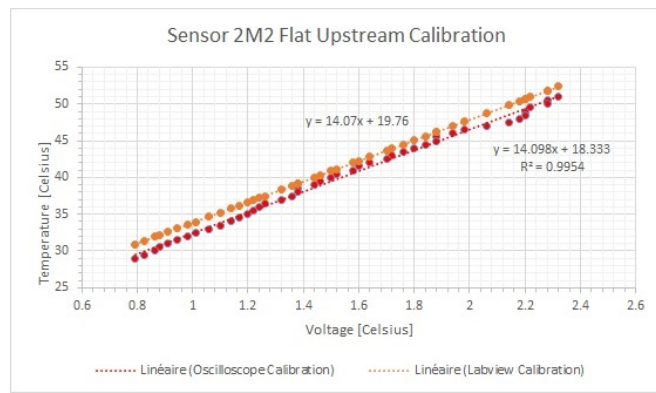


Figure 60: Calibration Curves of the 2M2 Upstream Sensor, when it is flat and put into a dish filled with water

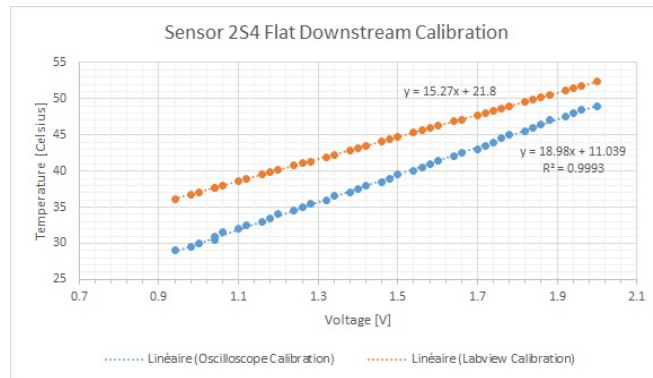


Figure 61: Calibration Curves of the 2S4 Downstream Sensor, when it is flat and put into a dish filled with water

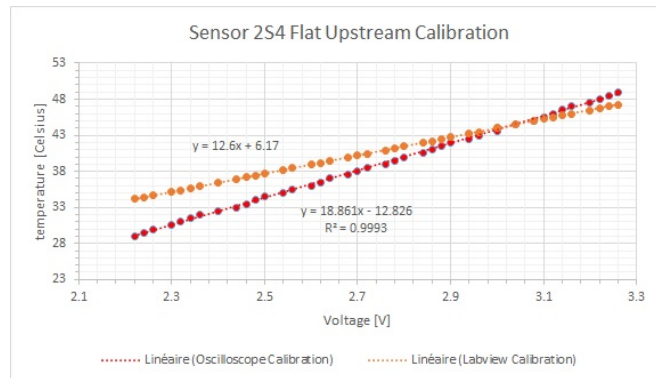


Figure 62: Calibration Curves of the 2S4 Upstream Sensor, when it is flat and put into a dish filled with water

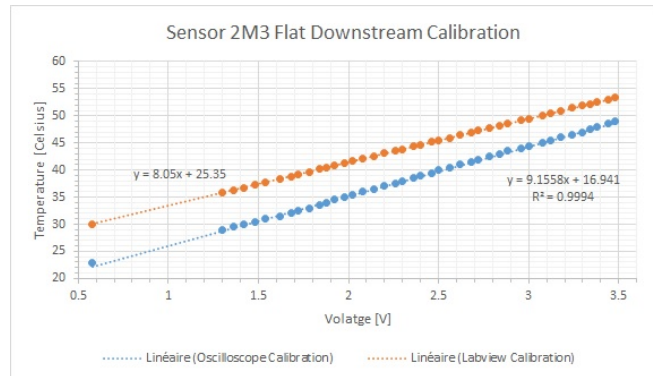


Figure 63: Calibration Curves of the 2M3 Downstream Sensor, when it is flat and put into a dish filled with water

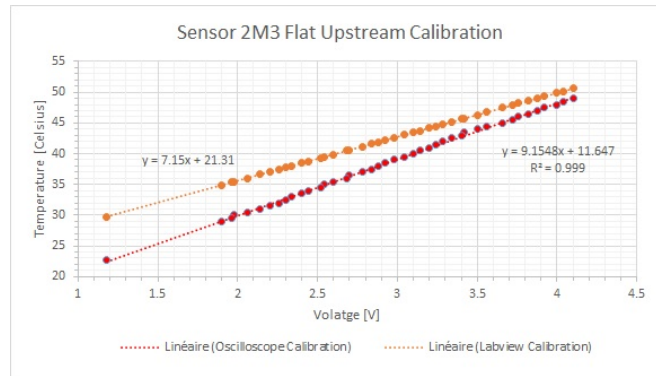


Figure 64: Calibration Curves of the 2M3 Upstream Sensor, when it is flat and put into a dish filled with water

10.4 Heater Testing

It is now time to test the flow rate functionality of the device by characterizing the heater element. As explained in the conditioning circuit section and as it can be observed in Figures 71 and 72 below, if we keep a 5mA current in order to heat the surrounding area and have the sensors measuring the temperature change due to heating, it works perfectly in air but not in water. The amplitude variation of the sensor is about 200mV, and it can be increased

while having higher current flowing into the heater. Moreover, the amplitude variation depends also on the distance between the two sensors and the heater, and it is obviously higher when the two sensors are closer to the heater. However we need to maintain enough gap between them so that conductivity is negligible.

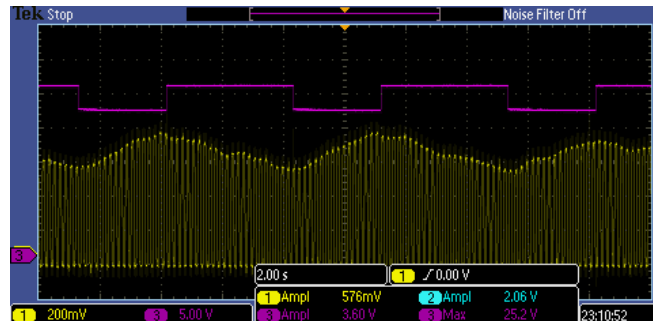


Figure 65: Variation in air of the amplitude of the sensor (yellow wave) when the heater is heating (low level of the purple wave) and when it is not (high level of the purple wave), with a 5mA current. The sensor is flat

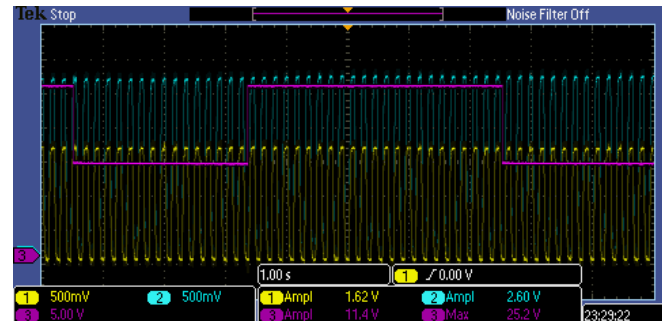


Figure 66: Variation in water of the amplitude of the sensor (yellow wave) when the heater is heating (low level of the purple wave) and when it is not (high level of the purple wave), with a 5mA current. The sensor is flat

Figures 67 and 68 below show the variation of the amplitude of the two sensors after the device has been inserted into a 2mm tube. In Figure 67, the amplitudes are increasing linearly with time whereas the the difference between the two amplitudes is the same. It means that there is no flow of air inside the tube and so the heater is heating the surrounding stagnant air. In Figure 68, while the heater is on, we have blown some air into the tube. The air is flowing from the downstream sensor (yellow curve) to the upstream sensor (blue curve). Hence the amplitude of the downstream sensor is decreasing since we are removing heat (the air we are blowing into the tube is colder than that of the air inside, heated by the heater), whereas the heated air is pushed towards the upstream sensor so its amplitude is increasing.

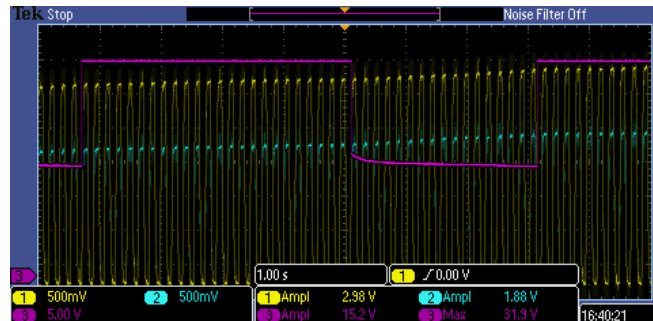


Figure 67: Variation in air, with no air flow, of the amplitude of the downstream sensor (yellow wave) and upstream sensor (blue wave) when the heater is heating (low level of the purple wave) and when it is not (high level of the purple wave), with a 21mA current. The sensor has been inserted into a 2mm diameter tube

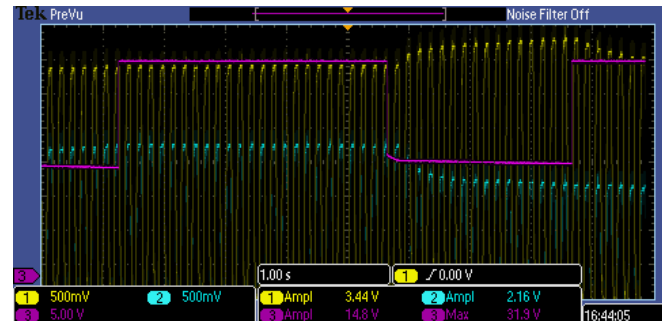


Figure 68: Variation in air, with air flow, of the amplitude of the downstream sensor (yellow wave) and upstream sensor (blue wave) when the heater is heating (low level of the purple wave) and when it is not (high level of the purple wave), with a 21mA injected current. The sensor has been inserted into a 2mm diameter tube

We can observe on Figure 69, from the high to the low level of the step, that the amplitude continues to decrease which means that because of the injecting current, the heater is heating but also heated, therefore its resistance increases. Moreover, because there is no flow, the amplitude of the two sensors is increasing and decreasing at the same rate. Finally, on Figure 70, when there is air flow from the downstream to the upstream sensor, we observe a similar behavior than on Figure 68, but with an increased amplitude difference between the two sensors. Regarding the low plateau of the heater, as before it decreases and then it increases again. Indeed, the flow of air is also refreshing the heater.

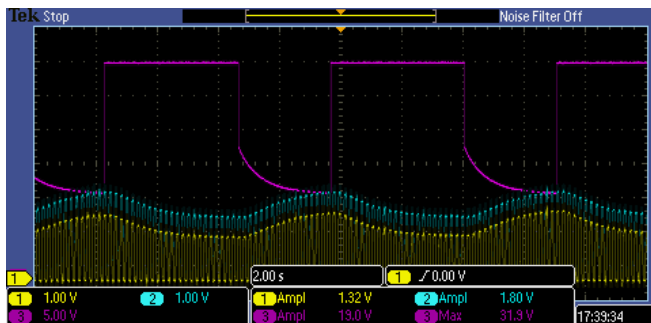


Figure 69: Variation in air, with no air flow, of the amplitude of the downstream sensor (yellow wave) and upstream sensor (blue wave) when the heater is heating (low level of the purple wave) and when it is not (high level of the purple wave), with a 25mA injected current. The sensor has been inserted into a 2mm tube

On the next two figures, we can see the effect of the heater when the sensor is inserted into a 2mm tube and water is flowing. We can observe that the amplitude of the downstream sensor is increasing whereas that of the upstream sensor is stationary, which tells us in which direction the flow is going. Therefore, thanks to the amplitude of the upstream sensor, we get the information on the temperature of the incoming water, whereas from the evolving amplitude difference between the upstream and downstream sensor, we can extract the flow. To get an effect of the heater on the sensors, we had to insert a current of 30 mA into the heater, which corresponds to a power of $P = RI^2 = 1k \times (30mA)^2 = 0.9W$. We unfortunately found out that this current is too high and it damages the heater after running for a time. As soon as we knew, we reduced the current to 20 mA.

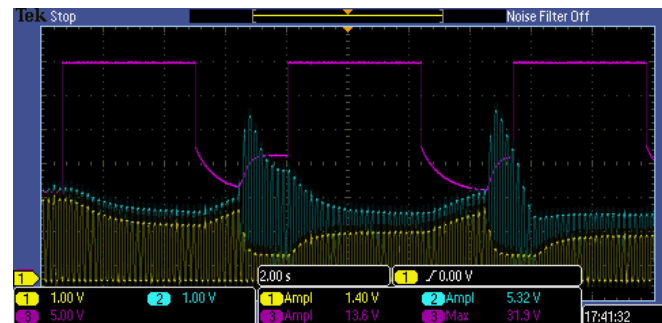


Figure 70: Variation in air, with air flow, of the amplitude of the downstream sensor (yellow wave) and upstream sensor (blue wave) when the heater is heating (low level of the purple wave) and when it is not (high level of the purple wave), with a 25mA injected current. The sensor has been inserted into a 2mm tube

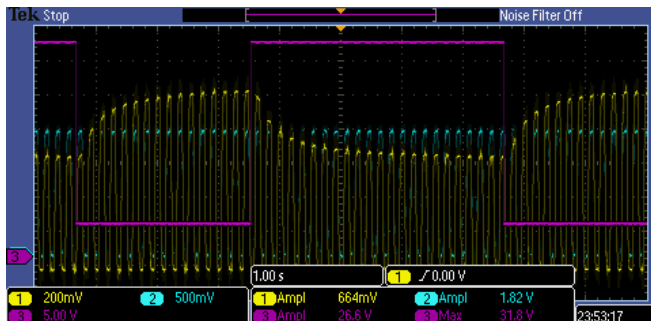


Figure 71: Variation in water, with flow, of the amplitude of the downstream sensor (yellow wave) and upstream sensor (blue wave) when the heater is heating (low level of the purple wave) and when it is not (high level of the purple wave), with a 30mA current. The sensor has been inserted into a 2mm tube

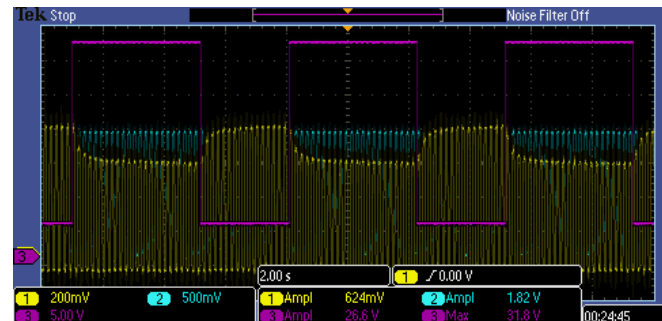


Figure 72: Variation in water, with flow, of the amplitude of the downstream sensor (yellow wave) and upstream sensor (blue wave) when the heater is heating (low level of the purple wave) and when it is not (high level of the purple wave), with a 30mA current, with more waves to show the periodicity of the behavior under constant flow. The sensor has been inserted into a 2mm tube

10.5 Temperature Calibration Under Water Flow

At this point in time, we unfortunately have not managed to calibrate the temperature sensors of the device once it is inserted into a tube and is exposed to flow. Indeed, one of the sensors (or both) always breaks. Its resistance increases to the $M\Omega$ range. It does not happen immediately but a while after the water has been flowing. We first observe instability of the square waves, and then the signal saturates.

On Figure 73 below is represented a sensor that has undergone flow and started showing some instability. It is inserted into a tube and the whole apparatus is placed into a container of water. We can fully observe the amplitude of the two sensors on the oscilloscope (Figure 75). Moreover, when we are dropping hot water into the plate, the amplitude of the two sensors increases without any offset. However, when we now connect the ground (we put inside the container the copper sheet, Figure 74), the sensors again started showing instability (Figure 76). Our

guess was that the sensors were not as well isolated that they should have been, and so the ground is propagating through the water to the sensors, which leads to saturation.

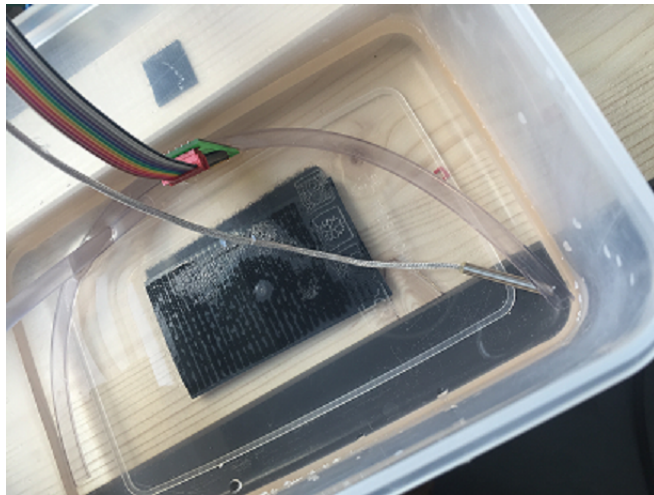


Figure 73: Submersion into stagnant water of the two sensors that had previously undergone flow and started showing instability. We made the temperature of the water increase by pouring in hot water from a kettle



Figure 74: Submersion into stagnant water of the two sensors that had previously undergone flow and started showing instability. We made the temperature of the water increase by pouring in hot water from a kettle. However, the water is connected to the external ground

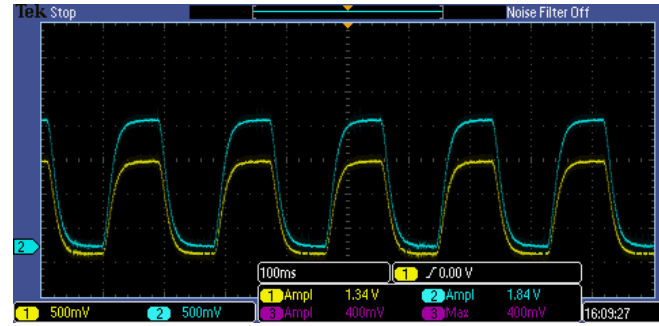


Figure 75: Measured amplitudes of the two sensors in stagnant water, without adding an external ground. The amplitude waves are smooth and stable; and the amplitude is increasing with water temperature

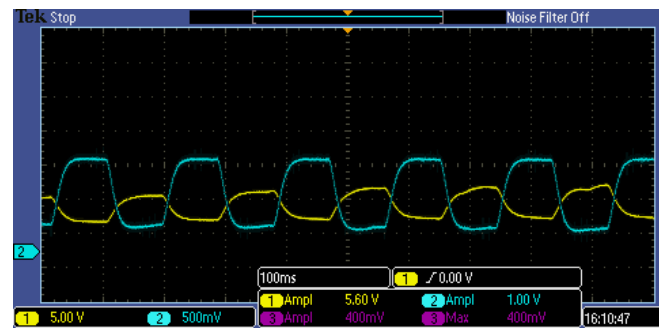


Figure 76: Measured amplitudes of the two sensors in stagnant water, with adding an external ground. The amplitude waves become unstable and we have obtained an offset

11 Discussion

While our testing led to very promising results, at this point in time, the device is unfinished. Various problems of excessive current and strange behaviors when trying to measure water flow keep appearing. It is useful to discuss what has gone wrong and why our device might have misbehaved as it did.

11.1 Potential Sources of Error

The data from the read-out circuit frequently displayed various amounts of noise as well as other small issues. These sources of error potentially lowered the accuracy of our device.

One problem we encountered when testing with the breadboard circuitry was that we had random and unpredictable noise which sometimes occurred. This noise would come and go without us changing anything on the circuit, so it was impossible to solve.

There was also a slight difference between the voltage amplitudes read by the oscilloscope and by the microcontroller. Sometimes the oscilloscope showed a slight negative voltage offset (the microcontroller can only read positive voltages). But other times, even when there was a positive voltage offset, the values from the two sources did not match. Which source was higher was never consistent. We calibrated based on the microcontroller's amplitudes, but these differences were still unpredictable and may have increased our device's error.

One other potential problem we noticed was that our parylene seal was not complete (Figure 77). Water entering our resistance layer would greatly affect the quality of the device. This leakage was seen on all sensors. Such an issue might have been due to the fact that the polyimide substrate and the parylene seal were not the same material, leading to a lower adhesion between the layers than if they had been the same material. As discussed in section 3.3.1, we ran out of time to pursue having a parylene substrate, but perhaps that would have prevented this problem.

This parylene leakage may have led to our lack of ability to calibrate the temperature sensors with flowing water. Alternatively, the top seal was tolerable but we might not have left enough margin between the side of the device and the sensors, so the water entered from the side, passing under the parylene layer. One solution we have tested with the last set of sensors was to put some glue on the sides in order to prevent the water from entering to the sides. Next time, we should also leave more place between the sensors on the wafers to that we have more room to cut them and so they should be more impermeable to water.



Figure 77: Image of a sensor after removing from water during flat calibration testing. The beads of water indicate that the parylene layer is not completely sealed.

The destruction of the heating element due to high current was an unexpected issue which we thought we had carefully guarded against with circuitry calculations. One reason this may have happened is because we are using a potentiometer to tune the value of the current. At low resistance values, this potentiometer shows instability and its resistance can drop even lower, causing a peak of the current and thus burning the heater. Therefore, we replaced the potentiometer by a fixed resistance value of 220Ω , in order to generate a 20mA current. To enable the heater to handle more current, we could have increased the thickness of the gold wires of the heater.

11.2 Suggestions for Future Improvements

Besides the problems already mentioned that must be addressed in future work, there are several other potential aspects which could be made better.

Calibration for flow rate was inhibited by the fact that flow was controlled in a somewhat unpredictable way; while the height of the tank relative to the sensor could be adjusted in discrete blocks and was thus reliable, there was no way of quantifying how widely the release valve of the tank was opened due to it being a handle that can be gradually turned. With more time, a simple 3D-printed accessory mounted near the valve handle could have solved this problem by creating discrete stopping points for the rotated handle, ensuring the same locations every time just like the height of the tank.

Another change which might have improved our device's sensitivity would be an alteration in the microcontroller system, specifically using a microcontroller or other substitute which has a wider range of readable voltages.

12 Conclusion

This project was a proof-of-concept of the development of a thin film sensor in a short period of time under a budget. Many details were responsible for the success of our project and altering just one small thing in the process flow or the circuitry had major effects on the final product.

Going through the many steps of the process flow for all iterations of our device taught us that the manufacturing of such sensors is not a one-size-fits-all process. Different metal mixtures required different settings for deposition; changes in the development solution necessitated varying development times; each process has its own quirks which had to be adjusted for. After three iterations with multiple wafers in each iteration, we were finally able to determine the optimal parameters for each step. We recognize that our final sensors used gold for the metal, which does not have as good of properties as platinum; since the platinum iteration failed due to unknown reasons, though, we had to compromise and go with the less ideal but still good gold resistances.

The read-out circuitry also served as a learning tool. Besides the original filters thought to be necessary, additional steps had to be taken to control noise, such as putting a grounding piece of metal in contact with the water. With so much rearrangement of the circuit happening throughout the project, several parts were accidentally blown out when they were given too much current, leading us to the lesson that there should always be spare parts on hand when possible. In fact, excessive current was one of our main problems in that our sensors kept getting destroyed by even 50 mA of current, despite the fact that they were designed to withstand much higher currents.

Although these challenges were bumps in the road, our team not only hurdled them but also succeeded in contributing unique ideas to the design along the way. One of the most innovative aspects of some of our sensors was their spiral shape. The spiral was discovered during our literature search, but was not very common despite it being more mechanically robust than classical serpentine patterns. We also built an intricate filtering circuit to minimize the noise coming from our sensor, enabling high precision readings. By taking advantage of several batteries, our final product was completely wireless and portable. Several other creative pursuits had to be abandoned for lack of time, such as using a parylene substrate or creating a more complete heat transfer model. Such ideas could be used for future innovation of this work.

The fact that we have yet to have a fully functioning device is not a deterrent to how successful this project still was. We still hope to obtain full functionality in the coming week, and our device is nearly working.

While this work is certainly a complete project in that we created a system for sensing temperature and flow, it could be expanded even further, especially in light of the growing need for flexible sensors in the biomedical market. Such a sensor could be coated with biocompatible materials and connected to miniaturized electronics, for example, to be used as an implantable device to monitor aortic blood flow in a patient with a heart condition. It could also be used to keep track of conditions in microfluidic chambers used for experiments with cells or microscopic organisms. The applications of thin, flexible temperature and flow sensors is nearly endless. This project demonstrated that those needs can be satisfied with a reasonable amount of time, money, and standard materials and equipment, which means it is likely not long until such sensors hit the market and revolutionize sensing techniques.

References

- [1] A.K. Henning, Microfluidic MEMS for semiconductor processing. *IEEE Transducer* 98 1998, B21, 329-337.
- [2] J.T.W Kuo, L. Yu and E. Meng, Micromachined Thermal Flow Sensors—A Review, Department of Biomedical Engineering, University of Southern California, 2012.
- [3] B. Khan, S. Ahmed and V. Kakkar, A comparative analysis of thermal flow sensing in biomedical applications, *International Journal of Biomedical Engineering and Science (IJBES)*, Vol. 3, No. 3, July 2016.
- [4] S. Rajasekaran, H. Qu and K. Zakalik, Thermal measurement of cerebrospinal fluid flow rate in hydrocephalus shunt. *IEEE Sensors*. 2015.
- [5] R.Kersjes, F. Liebscher, E. Spiegel, Y. Manoli and W. Mokwa, An invasive catheter flow sensor with on-chip CMOS readout electronics for the on-line determination of blood flow. *Sens. Actuat. A*. 1996, 54, 563-567.
- [6] A. Alt, Flow measurement in smart inhalers for connected drug delivery. *Sensiron*, 2018.
- [7] J.V. Kuijk, J.C.C.V. Kuijk, T.S.J. Lammerink, H.E. de Bree, M.C. Elwenspoek and J.H.J. Fluitman, Multi-parameter detection in fluid flows. *Sens. Actuat. A* 1995, 47, 369–372.
- [8] M. Ashauer, H. Glosch, F. Hedrich, N. Hey, H. Sandmaier and W.Lang, Thermal flow sensor for liquids and gases based on combination of two principles, *Sens. Actuators, A*, 1999, 73
- [9] F. Durst, A. Al-Salaymeh and J. Jovanovic, Theoretical and experimental investigation of a wide range thermal velocity sensor, *Meas. Sci. Technol.*, 2001
- [10] M.J. Waldron, Design, simulation, and fabrication of a flow sensor for an implantable micropump, Theses Rochester Institute of Technology, 2009.
- [11] H. Berthet, J. Jundt, J. Durivault, B. Mercier and D. Angelescu, Time-of-flight thermal flowrate sensor for lab-on-chip applications. *Lab Chip* 2011, 11, 215–223.
- [12] L.Y. Yeo and J.R. Friend, Surface Acoustic Wave Microfluidics. *Annual Review of Fluid Mechanics*, January 2014, Vol. 46:379-406.
- [13] E.F.C. Meng, MEMS Technology and Devices for a Micro fluid Dosing System (Doctoral dissertation) California Institute of Technology, 2003. P. 125
- [14] M. Vraanes, S. Lee, Thermal Mass Flow Sensors for Gas and Liquid Applications. *IJBES*, July 2016. p. 2
- [15] M.Dijkstra, M.J.de Boer, J.W. Berenschot, T.S.J. Lammerink, R.J. Wiegerink and M.Elwenspoek, Miniaturized thermal flow sensor with planar-integrated sensor structures on semicircular surface channels. Elsevier, 2008. p. 553
- [16] A.N.A. Prouza, High Precision Flow Independent Thermal Conductivity Detector for Gas Sensing with Readout Circuit, at the Delft University of Technology, to be defended publicly on Day 25th September, 2015 at 10:30 AM, p. 7-9, p. 32
- [17] Temperature measurement, Cottrell Education, p. 11, p. 13-16, p. 20
- [18] R. Buchner, K. Froehner, C. Sosna, W. Benecke, and W. Lang, Toward flexible thermoelectric flow sensors: A new technological approach, *J. Microelectromechanical Syst.* 2008, 17, p. 1114–1119
- [19] R. Jacob Baker, CMOS circuit design, layout and simulation, IEEE press, chap. 23, p. 757-765
- [20] M. Malits, I. Brouk and Y. Nemirovsky, Study of CMOS-SOI Integrated Temperature Sensing Circuits for On-Chip Temperature Monitoring, *Sensors* 2018, 18, 1629; doi: 10.3390/s18051629
- [21] Temperature sensors – Types, working and operation, ElProCus
- [22] M. Elwenspoek, Thermal flow micro sensor. Semiconductor conference, 1999.
- [23] G. Chowdhury and A. Hassibi, An On-Chip Temperature Sensor With a Self-Discharging Diode in 32-nm SOI CMOS, *IEEE Transactions on circuits and systems II: Express Briefs*, vol. 59, NO. 9, September 2012

- [24] RTD temperature sensors: How are they designed?, SensorTips, WTHW Media LLC, 2009
- [25] RTD measurement and theory, OMEGA Engineering
- [26] Measuring Temperature with RTDs – A tutorial, National Instruments Corporation, November 1996
- [27] A Basic Guide to RTD Measurementi, Texas Instruments, June 2018, p. 4
- [28] V. Balakrishnan, H.P. Phan, T. Dinh, D.V. Dao, N.T. Nguyen. Thermal flow sensors for harsh environments. School of Engineering, Griffith University. 4 September 2017.
- [29] C. Li, P. Wu, J.A. Hartings, Z. Wu, C. Cheyuo, P.W., D. LeDoux, L.A. Shutter, B.R. Ramaswamy, C.H. Ahn, R.K. Narayan, Micromachined lab-on-a-tube sensors for simultaneous brain temperature and cerebral blood flow measurements, Biomed Microdevices (2012) p. 14, p. 759–768
- [30] S. Ferdous, S. Sarkar, F. Marty, P. Poulichet, W. César et al. Sensitivity optimization of micro-machined thermo-resistive flow-rate sensors on silicon substrates. Journal of Micromechanics and Microengineering, IOP Publishing, 2018
- [31] T. Berlicki, E. Murawski, S. Osadnik, E. Prociów, Thermoresistive thin film flow sensor. Act. Passive Electron. Comp. 1989, 13, p. 161–173.
- [32] K.G. Kreider, F. DiMeo, Platinium/palladium thin film thermocouples for temperature measurements on silicon wafer, Sens. Actuators A: Phys. 69 (1998), p. 46-52
- [33] F. Mailly, A. Giani, R. Bonnot, P. Temple-Boyer, F. Pascal-Delannoy, A. Foucaran and A. Boyer, Anemometer with hot platinum thin film, sens. Actuators A: Phys. 94 (2001), p. 32-38
- [34] J.T.W. Kuo, L.Y. Chang, P.Y. Li, T. Hoang, E. Meng, A microfluidic platform with integrated flow sensing for focal chemical simulation of cells and tissue, sens. Actuators B: Chemical, p. 267-276
- [35] B.C. Kaanta,H. Chen, G. Lambertus, W.H. Steinecker, O. Zhdaneev, X. Zhang, High sensitivity micro-thermal conductivity detector for gas chromatography. In Proceedings of the IEEE 22nd International Conference on Micro Electro Mechanical Systems, Sorrento, Italy, 2529 January, 2009
- [36] I.O. Martins, Parylene C as substrate, dielectric and encapsulation for flexible electronics applications, Licenciada em Ciências de Engenharia de Micro e Nanotecnologias, september 2017
- [37] E. Meng, P.Y. Li, Y.C. Tai, A biocompatible Parylene thermal flow sensing array. Sens. Actuat. A 2008, 144, 18–28.
- [38] C. Li, P.M. Wu, J.A. Hartings, Z. Wu, C.H. Ahn, R.K. Narayan, Cerebral blood flow sensor with in situ temperature and thermal conductivity compensation. In Proceedigns of the 25th International Conference on Micro Electro Mechanical Systems, Paris, France, 29 January–2 February 2012; pp. 1021–1024.
- [39] H.Yu, L. Ai, M. Rouhanizadeh, D. Patel, E.S. Kim, T.K. Hsiai, Flexible polymer sensors for in vivo intravascular shear stress analysis. J. Microelectromechanical Syst. 2008, 17, 1178–1186.
- [40] M.K. Ghosh, K.L. Mittal, Polyimides: fundamentals and applications. New York: Marcel Dekker (1996). 126–130 pp.
- [41] W.Y. Chang, T.H. Fang, Y.C. Lin, Physical characteristics of polyimide films for flexible sensors. Appl Phys. A 92: 693–701 (2008).
- [42] R. Ahrens, K. Schlotte-Holubek, A micro flow sensor from a polymer for gases and liquids. J. Micromech. Microeng. 2009, doi: 10.1088/0960-1317/19/7/074006.
- [43] P. Fürjes, G. Légrádi, C. Dücső, A. Aszódi, I. Bárszny, Thermal characterisation of a direction dependent flow sensor Sens. Actuators Phys. (2004) 115 417–23
- [44] E. Obermeier, P. Kopystynski, R. NieBl, Characteristics of polysilicon layers and their application in sensors. In IEEE Solid-State Sensors Workshop; IEEE Press: New York, NY, USA, 1986.

- [45] H.M. Chuang, K.B. Thei, S.F. Tsai, W.C. Liu, Temperature-dependent characteristics of polysilicon and diffused resistors. *IEEE Trans. Electron. Devices* 2003, 50, 1413–1415
- [46] C. Li P.-M. Wu, J. Han, C. H. Ahn, A flexible polymer tube lab-chip integrated with microsensors for smart microcatheter, Springer Science + Business Media, LLC 2008
- [47] R. Buchner, C. Sosna, M. Maiwald, W. Benecke, W. Lang, A high-temperature thermopile fabrication process for thermal flow sensors. *Sens. Actuat. A* 2006, 130–131, 262–266.
- [48] M. Melani, L. Bertini, M. De Marinis, P. Lange, F. D’Ascoli, L. Fanucci, Hot wire anemometric MEMS sensor for water flow monitoring. Design, Automation, and Test in Europe: 2008 conference. 2008.
- [49] Properties of material and simulation softwar, <https://www.simulationmateriaux.com>
- [50] Mr.I. Khamnusansin, Lab IV :Opamp Signal-Conditioning Circuit for 3-Wire RTD Bridge
- [51] Ju-Young Kim, Julia R. Greer, Tensile and compressive behavior of gold and molybdenum single crystals at the nano-scale. *ScienceDirect*. 2008.
- [52] A.I. Olivia, J.M. Lugo,R.A. Gurubel-Gonzalez, R.J. Senteno, J.E. Corona, F.Avilés, Temperature coefficient of resistance and thermal expansion coefficient of 10nm-thick gold films. *Thin Solid Films* 623 (2017) 84-89.
- [53] C. Li, P.M. Wu, J.A. Hartings, Z. Wu, C.H. Ann, D. Ledoux, L.A.Shutter and R.A.Narayan, Smart catheter flow sensor for real-time continuous regional cerebral blood flow monitoring. *Appl. Phys. Lett.* 99, 233705 (2011).
- [54] J. Böhm, P. Gruber, R. Spolenak, A. Stierle, A. Wanner, E. Arzt, Tensile testing of ultrathin polycrystalline films: A synchrotron-based technique, *Review of Scientific Instruments*, 2004.
- [55] NTC Thermistor. Resistorguide.com. EETech Media, LLC. Accessed 06 June 2019.
- [56] P. Waters. Stress analysis and mechanical characterization of thin films for microelectronics and MEMS applications. University of South Florida, PhD Dissertation. 22 April 2008.
- [57] J. Y. Faou. Mechanics of functional thin films: instabilities and adhesion. *Mechanics of Materials*. University of Pierre and Marie Curie. 2013.
- [58] E. Macia-Barber, Thermoelectric materials, Advances and Applications, Research Gate may 2015.
- [59] G. Boero, P. Renaud. Capteurs, EPFL course. Capteurs Thermique lecture slides. Spring 2018.

13 Appendix

13.1 Budget and Team Management

Talk about the budget and who did what, for both the project and the report "This should be described in one page. It should include how you worked as a team and how your project budget was managed. This is also where you can say who wrote which section of the report."

With such a diverse interdisciplinary group, each member of the team brought their own strengths to the table. In the very beginning of the project, we broke the entire project down into groups of tasks which each person would be responsible for, and more or less maintained this task division through the entire semester. Speaking on a large scale, Damien and Stan worked together on the design and manufacturing of the sensor itself while Pierre and Brooke teamed up to create the system for reading, processing, and displaying the data.

On a more detailed level, each teammate had an expertise that they contributed. Damien's mechanical engineering background came in handy for running stress-strain simulations and thermal calculations, which were used to optimize the layout of our sensor. Stan used his microengineering knowledge to delve into a material analysis, determining the most effective combination of materials for our device. Pierre, as an electrical engineer, designed an intricate filtering circuit which properly excited our sensor and produced clean data. Brooke took advantage of her microcontroller and programming knowledge to assemble the system which wirelessly transmits the data and displays its results in a graphical user interface in LabVIEW. Of course, each of these specialties overlaps with the others, and thus there was much cross-collaboration. Ultimately, it was truly a team effort.

In regards to writing the report, each team member wrote about the part that they had worked on. The State of the Art section was shared equally among the team. Results were mostly written by Pierre, who did much of the calibration and testing. Stan and Damien had a lot to write about the simulations and clean room work for manufacturing the sensor, so Brooke took on the introduction, conclusion, and general refining of the report.

The 2000 CHF budget was approximately attributed to various project aspects in the beginning and adjusted as the semester went on. In the end, the entire project was a comfortable amount under the allotted budget (Table 13, Figure 78).

Category	Expense	Cost (CHF)
Clean room	Device iterations except parylene coating	550
	Parylene coating	175
Connection	Small PCBs	150
	Wire bonding	150
Read-out circuit	Big PCB routing	180
	Big PCB fabrication	105
	Electrical components of big PCB	275
	Big PCB soldering	140
	Microcontroller, batteries	30
Calibration	External sensors	100
Total		1855

Table 13: Budget breakdown. The total budget available was 2000 CHF.

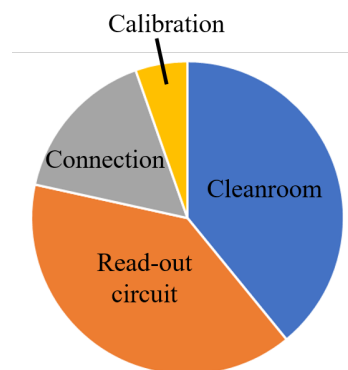
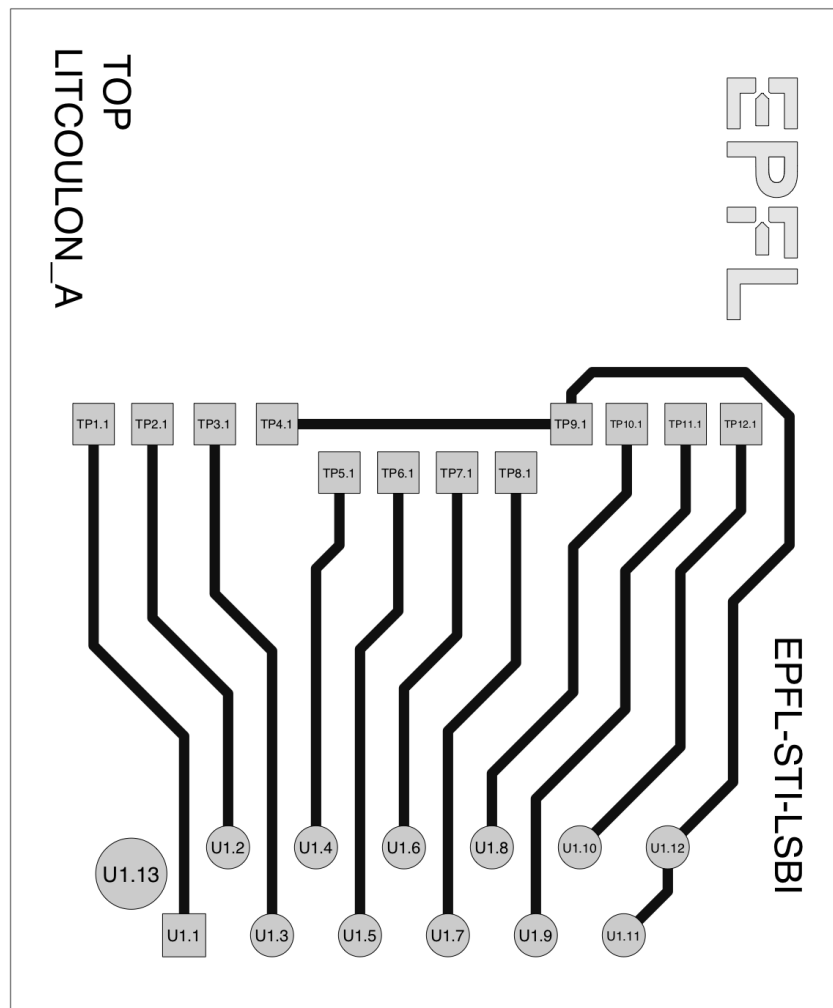


Figure 78: Pie chart breakdown of the budget categories.

13.2 Small PCB Layout



EPFL ACI-CAO pb Project = litcoulon_a - litcoulon_gloss.brd - Etch_Top 12.4.2019 16:29 Scale = 8.00 2.50 mm = ————— Page 5

Figure 79: Small PCB design

13.3 LabVIEW Block Diagrams

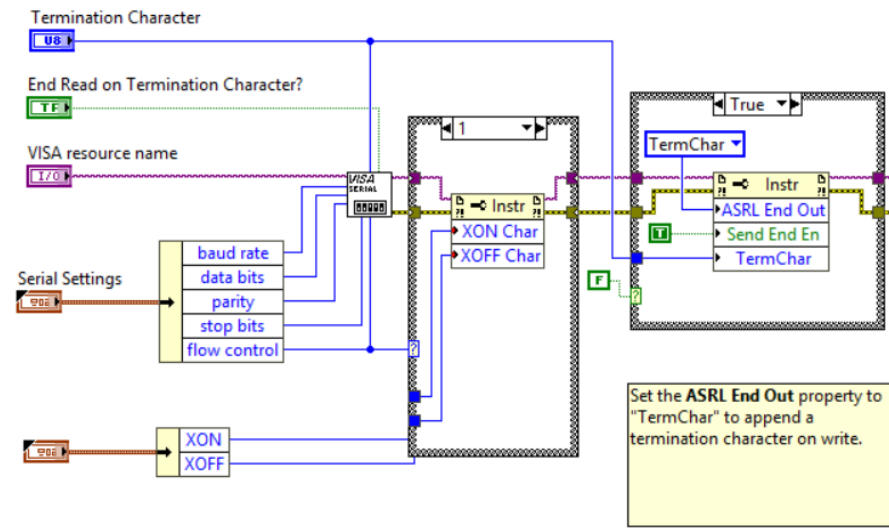


Figure 80: Block diagram section of the LabVIEW interface which handles the reading of the Bluetooth data. This uses the National Instruments visa driver, which is involved in serial input. On the graphical interface, some of these settings must be adjusted to match those of the microcontroller.

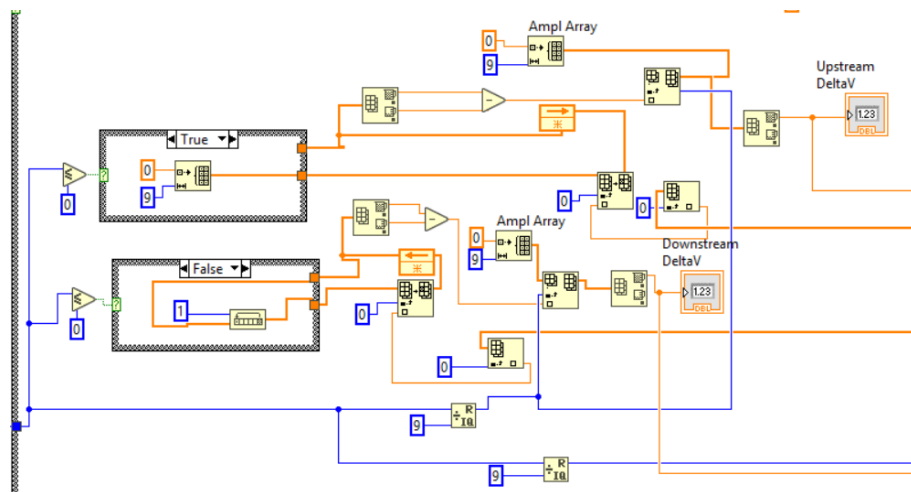


Figure 81: Block diagram section of the LabVIEW interface which processes the real-time data to produce an amplitude of each voltage wave. The case structures handle the very first iteration, upon which the 9-element array that will later hold each voltage reading is created. For every iteration other than the first, the case structure is false, shifting the array elements by 1 to get rid of the oldest data point and make room for the new data point. To calculate the amplitude, the program finds the difference between the largest and the smallest values in the array at any given time.

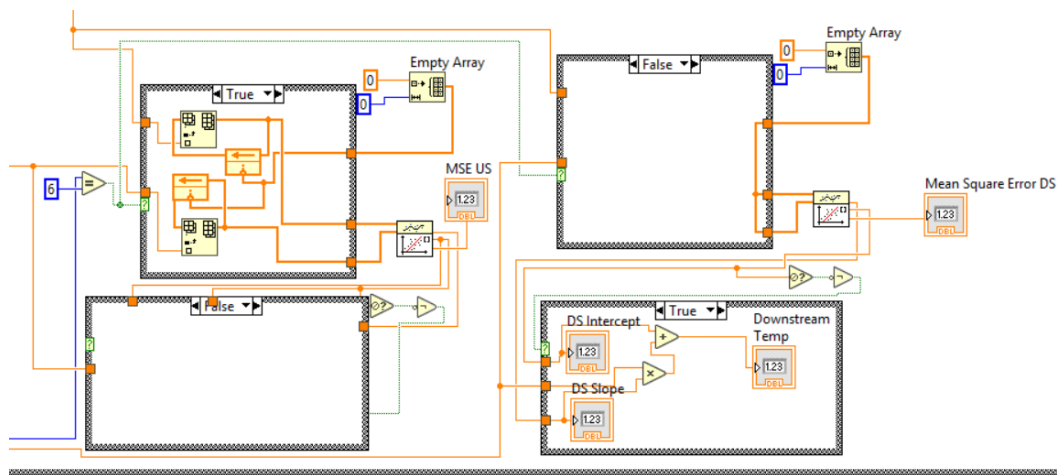


Figure 82: Block diagram section of the LabVIEW interface which performs calibration of the two device's temperature sensors. Both of the top case structures are identical and both of the bottom case structures are identical, so the true and false options of each are shown for completeness. The top case structures are true once every time a square wave of data is completed, and false at all other times, to ensure only one amplitude per wave is collected. These feed an array of true temperature and an array of voltage amplitudes to a linear fitting module. The bottom case structures control for the fact that there is only one slope and intercept per wave, and every other time the slopes and intercepts are not a number. When the slope and intercept are numbers, they are used to calculate the temperatures based on the voltage amplitudes.

13.4 Testing Setup

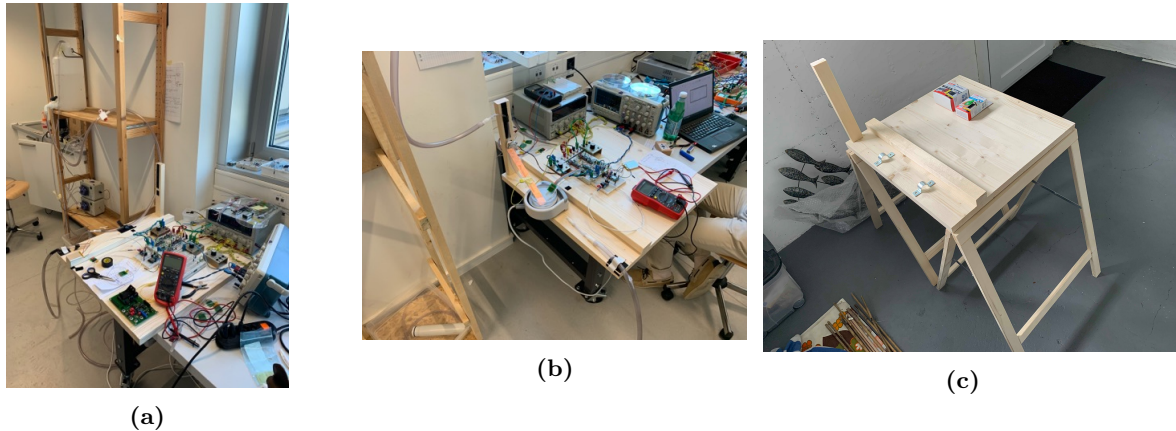


Figure 83: Testing Setup (a)all setup (b)Read-out circuit (c) wood stand

13.5 Electronic Setup and Oscilloscope Readings

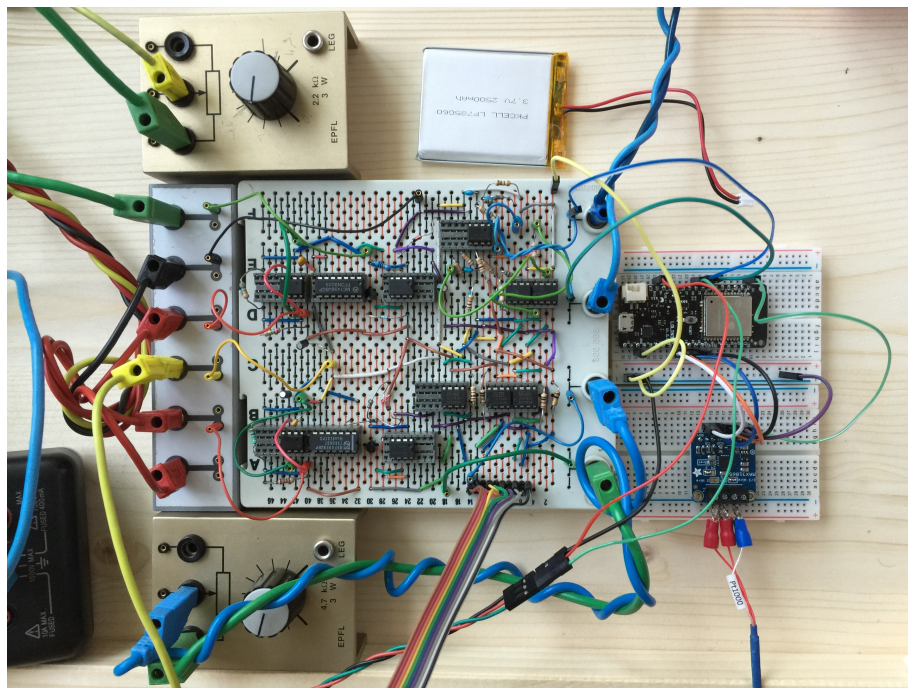


Figure 84: Picture of the Hirschmann board on which the circuits blocks - presented into the conditioning circuit section - are mounted; along with the microcontroller and the reference temperature sensor

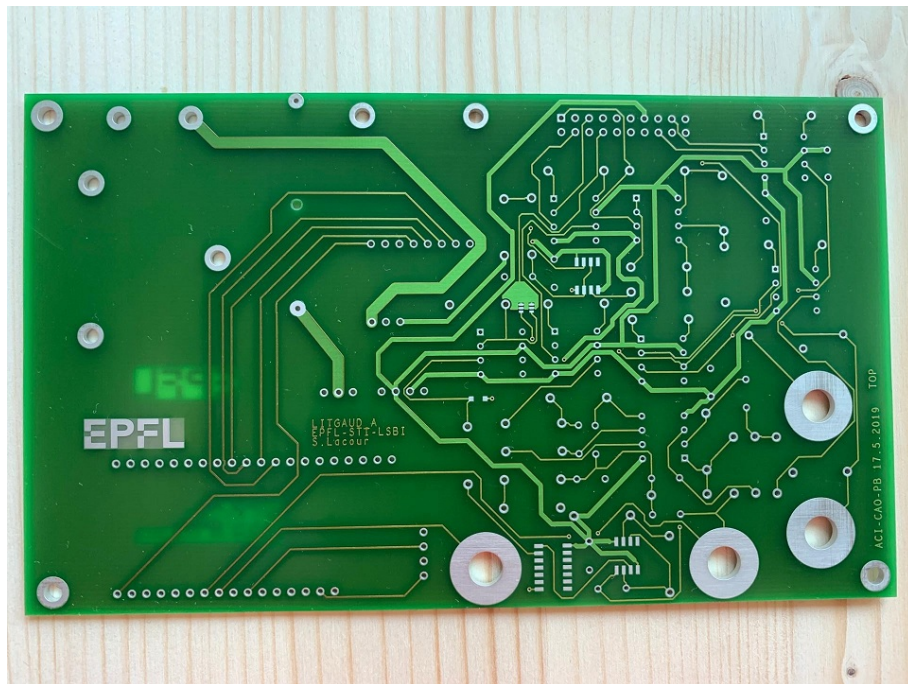


Figure 85: Outline of the PCB before the components are added. The size of the PCB is 195 by 12mm

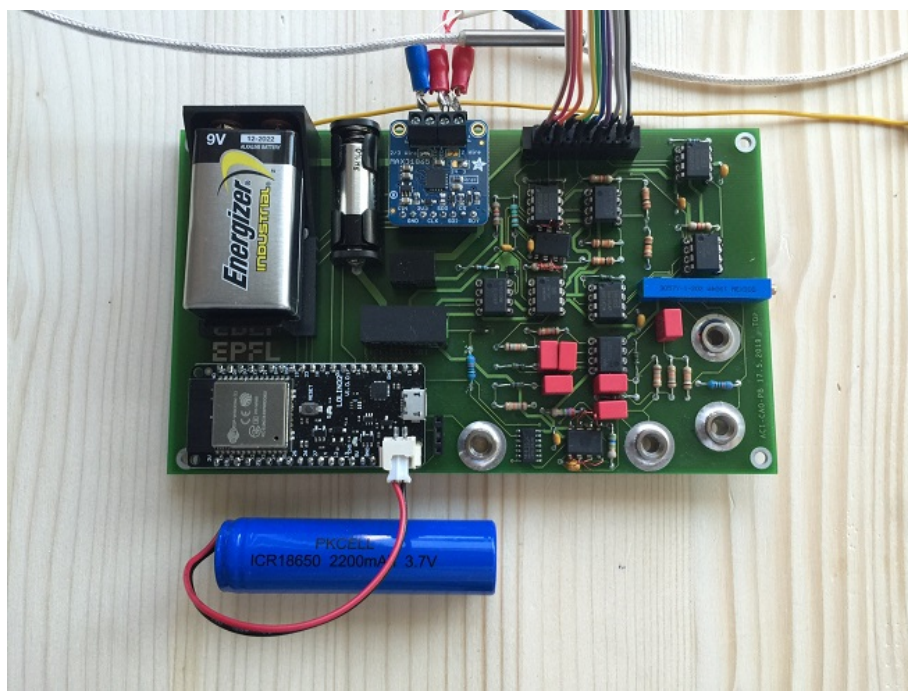


Figure 86: Final Result of the PCB with all the components added to it

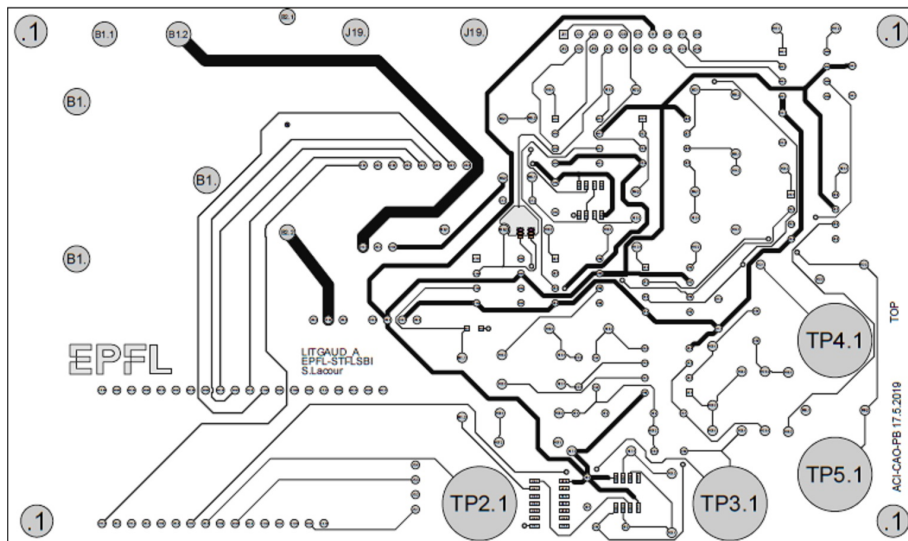


Figure 87: Schematic of the PCB connections between the different components

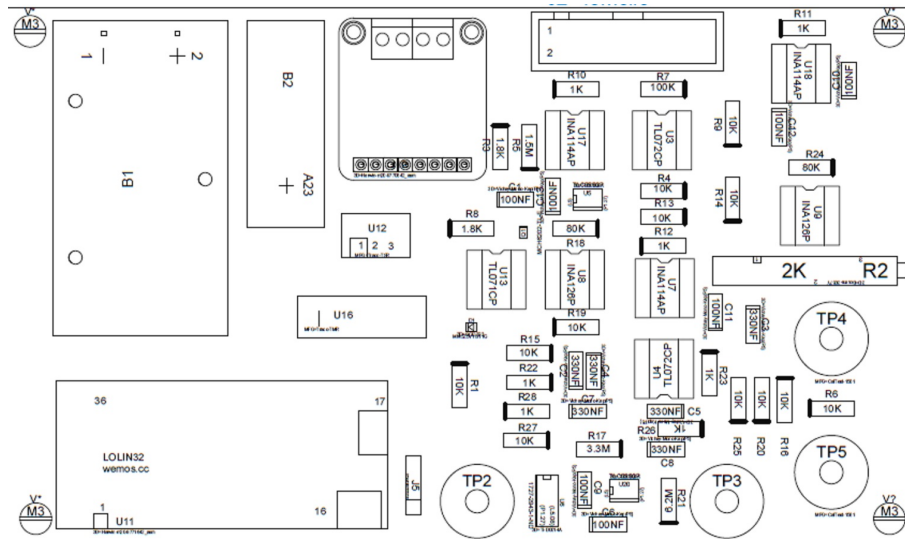


Figure 88: Schematic of the placement of the different components of the PCB before fabrication

13.6 Detailed Formulas For Upstream and Downstream Sensors

Upstream Sensor:

$$\begin{aligned}
 \Delta V_{Upstream} &= G_f G_2 (V_{Upstream} - V_{Reference}) \\
 \Delta V_{Upstream} &= G_f G_2 (I_0 G_1 (R_{0Upstream} - R_{Reference}) + G_1 \alpha_{gold} I_0 R_{0Upstream} (T_{abs} - T_0)) \\
 \Delta V_{Upstream} &= Intercept + Slope \times T_{abs} \\
 Slope &= G_f G_2 G_1 \times \alpha_{gold} I_0 R_{0Upstream} \\
 Intercept &= G_f G_2 G_1 \times (I_0 (R_{0Upstream} - R_{Reference}) - \alpha_{gold} I_0 R_{0Upstream} T_0)
 \end{aligned} \tag{20}$$

Downstream Sensor:

$$\begin{aligned}
 \Delta V_{Downstream} &= G_f G_2 (V_{Downstream} - V_{Reference}) \\
 \Delta V_{Downstream} &= G_f G_2 (I_0 G_1 (R_{0Downstream} - R_{Reference}) + G_1 \alpha_{gold} I_0 R_{0Downstream} (T_{abs} - T_0)) \\
 \Delta V_{Downstream} &= Intercept + Slope \times T_{abs} \\
 Slope &= G_f G_2 G_1 \times \alpha_{gold} I_0 R_{0Downstream} \\
 Intercept &= G_f G_2 G_1 \times (I_0 (R_{0Downstream} - R_{Reference}) - \alpha_{gold} I_0 R_{0Downstream} T_0)
 \end{aligned} \tag{21}$$

Ideally, we would like the difference $R_{0sensor} - R_{Reference}$ to be zero. However, doing this leads to instability of the electronic circuits. Moreover, the potentiometer we are having is not very precise.

13.7 Toricelli's Principle

```
%Toricelli's principle
clc
clear all
close all

Flow = [10:5:100]; %cm^3/s
Tube_diameter = [2, 5, 10]*1e-1; %cm
Surface = pi * (Tube_diameter/2).^2; %cm^2
g = 9.81; %m/s^2

%Compute the height difference between the output of the tank and the top
%of the water column
H = zeros(length(Flow),length(Surface));
for i=1:length(Surface)
    H(:,i) = Flow.^2 ./ (2*g*1e2*Surface(i).^2); %cm
end

figure()
D2 = semilogy(Flow, H(:,1),'b+-');
hold on
D5 = semilogy(Flow, H(:,2),'r+-');
D10 = semilogy(Flow, H(:,3),'k+-');
hold off
grid on
legend([D2,D5,D10],{'2mm tube','5mm tube','10mm tube'})
xlabel('Flow rate [mL/s]')
ylabel('Height [cm]')
title('Variation of the height of the column of water with respect to the required flow')
```

Figure 89: Matlab code to obtain the theoretical heights of the tank required for a given flow and a given tube diameter. The output plot of the code is shown on Figure 57

13.8 Matlab Code for the Resistance

```

%% Variable
% N : Number of element test : 10-20
% L' : Straight segment test : 3-5 [mm]
% t : Thickness test : 100 [nm]
% x : width test : 30-35 [micron]
% ro : Conductivity test : 22*10^(-9) [Ohm/m] Gold

%% Function Serpentine
% Resistance = ro*(N*(2*(L+pi*x))-pi*x)/(x*t); ;
% Surface = (L+3*x)*(4*N-1); ;
%%%%%%%%%%%%%%%
%% Plot fonction
% L=5 [mm] x=30 [um]
ResistanceL1x1 = ro*(N*(2*(L1+pi*x1))-pi*x1)/(x1*t); ;
|
% L=3 [mm] x=35 [um]
ResistanceL3x2 = ro*(N*(2*(L3+pi*x2))-pi*x2)/(x2*t); ;
|
% L=5 [mm] x=35 [um]
ResistanceL1x2 = ro*(N*(2*(L1+pi*x2))-pi*x2)/(x2*t); ;

```

Figure 90: Matlab code to obtain the theoretical resistance of the serpentine

13.9 Acknowledgements

The authors would like to say a big thank you to everyone who helped us toward our goal. The biggest nod of appreciation goes to our team mentor, Dr. Yves Leterrier, who faithfully monitored our progress each week. Thank you also to: Cedric Meinen, our electronics consultant; Jean-Baptiste Leran, the LabVIEW expert; Giancarlo Corradini, who performed our wire bonding at the CMi; Peter Bruhlmeier and Jean-Marie Barblan, the ACI coordinator who assisted us with the PCBs; Adil Koukab, for his assistance with our read-out circuit; Florian Bourgeois, who led our cleanroom training; Cyrille Hibert and George Andre Racine, who served as consultants on our process flow; Santiago Andany, for his assistance with soldering; and the EPFL association Robopoly, for their expertise on microcontrollers. Finally, thank you to Dr. Stephanie Lacour for arranging the Lab in Tube project, enabling each of us to learn so much by having access to many resources and a neat project to pursue.